

AD-A233 600

AFATL-TR-90-84

A Dynamic Failure Model for Ductile Materials

**A. M. Rajendran
D. J. Grove, et al**

**UNIVERSITY OF DAYTON RESEARCH INSTITUTE
300 COLLEGE PARK
DAYTON, OHIO 45469-0120**

FEBRUARY 1991

FINAL REPORT FOR PERIOD OCTOBER 1988 - AUGUST 1990

APPROVED FOR PUBLIC RELEASE; DISTRIBUTION UNLIMITED

AIR FORCE ARMAMENT LABORATORY
Air Force Systems Command ■ United States Air Force ■ Eglin Air Force Base, Florida

NOTICE

When Government drawings, specifications, or other data are used for any purpose other than in connection with a definitely Government-related procurement, the United States Government incurs no responsibility or any obligation whatsoever. The fact that the Government may have formulated or in any way supplied the said drawings, specifications, or other data, is not to be regarded by implication, or otherwise as in any manner construed, as licensing the holder, or any other person or corporation; or as conveying any rights or permission to manufacture, use, sell any patented invention that may in any way be related thereto.

This report has been reviewed and is approved for publication.

FOR THE COMMANDER

Martin F. Zimmer

MARTIN F. ZIMMER
Technical Director

Even though this report may contain special release rights held by the controlling office, please do not request copies from the Air Force Armament Laboratory. If you qualify as a recipient, release approval will be obtained from the originating activity by DTIC. Address your request for additional copies to:

Defense Technical Information Center
Cameron Station
Alexandria, Virginia 22304-6145

If your address has changed, if you wish to be removed from our mailing list, or if your organization no longer employs the addressee, please notify AFATL/ MNW, Eglin AFB FL 32542-5434, to help us maintain a current mailing list.

Do not return copies of this report unless contractual obligations or notice on a specific document requires that it be returned.

REPORT DOCUMENTATION PAGE			Form Approved OMB No. 0704-0188	
<small>Public reporting burden for this collection of information is estimated to average 1 hour per response, including the time for reviewing instructions, searching existing data sources, gathering and maintaining the data needed, and completing and reviewing the collection of information. Send comments regarding this burden estimate or any other aspect of this collection of information, including suggestions for reducing this burden, to Washington Headquarters Services, Directorate for Information Operations and Reports, 1215 Jefferson Davis Highway, Suite 1204, Arlington, VA 22202-4302, and to the Office of Management and Budget, Paperwork Reduction Project (0704-0188), Washington, DC 20503.</small>				
1. AGENCY USE ONLY (Leave blank)	2. REPORT DATE September 1990	3. REPORT TYPE AND DATES COVERED Final Oct. 88-Aug. 90		
4. TITLE AND SUBTITLE A Dynamic Failure Model for Ductile Materials		5. FUNDING NUMBERS PE: 626062F JON: 25020701 F33615-86-C-5064		
6. AUTHOR(S) A. M. Rajendran, D.J. Grove, M. A. Dietenberger, W. H. Cook				
7. PERFORMING ORGANIZATION NAME(S) AND ADDRESS(ES) Univ. of Dayton Research Inst. Munitions Division 300 College Park Eglin AFB FL Dayton, OH 45469-0120 32452-5434		8. PERFORMING ORGANIZATION REPORT NUMBER UDR-TR-90-109		
9. SPONSORING / MONITORING AGENCY NAME(S) AND ADDRESS(ES) Warheads Branch Munitions Division Air Force Armament Laboratory Eglin AFB FL 32542-5434		10. SPONSORING / MONITORING AGENCY REPORT NUMBER AFATL-TR-90-84		
11. SUPPLEMENTARY NOTES This report was a joint effort between the University of Dayton Research Institute and the Air Force Armament Laboratory. Therefore, the report is in contractor format.				
12a. DISTRIBUTION / AVAILABILITY STATEMENT Approved for public release; distribution is unlimited.		12b. DISTRIBUTION CODE		
13. ABSTRACT (Maximum 200 words) This report presents a recently developed continuum mechanics based dynamic failure model for ductile metals. Ductile failure often initiates due to void nucleation and growth. The void generation degrades the strength and stiffness of the initially void-free material. Realistic modeling of this failure process requires an accurate description of the strain rate and temperature dependent plastic flow in the intact material surrounding the microvoids. This is all the more important when the evolution law for ductile void growth is based on the plastic deformation in the intact material. An elastic perfectly plastic idealization of the intact material may lead to erroneous or sometimes limited applicability of the failure model. The present failure model incorporates a state variable based viscoplastic theory into the model formulation. The void nucleation is modeled as a statistical process. A Gaussian function based on mean stress and/or strain threshold has been used in the failure model formulation. Model constants were determined for OFHC copper, Armco Iron, MAR-200, MAR-250, AF1410, C1008, and HY100 steels and tantalum. As a final exercise the ductile failure processes in different geometrical configurations were described by the RDG model.				
14. SUBJECT TERMS Ductile Failure Hydrocode Model Fracture		15. NUMBER OF PAGES 94		
		16. PRICE CODE		
17. SECURITY CLASSIFICATION OF REPORT UNCLASSIFIED	18. SECURITY CLASSIFICATION OF THIS PAGE UNCLASSIFIED	19. SECURITY CLASSIFICATION OF ABSTRACT UNCLASSIFIED	20. LIMITATION OF ABSTRACT SAR	

PREFACE

This report describes a joint contractual and in-house effort conducted by personnel of the University of Dayton Research Institute and of the Warheads Branch, Munitions Division, Air Force Armament Laboratory under project 25020701 (Numerical Hydrodynamics).

The work reported herein was performed during the period 1 October 1988 to 30 August 1990. Work performed at the University of Dayton Research Institute was supported by Air Force contract number F33615-86-C-5064 monitored by Dr. Theodore Nicholas of the Air Force Wright Research and Development Center, Wright-Patterson Air Force Base OH. Work conducted by the Air Force Armament Laboratory at Eglin Air Force Base was supported by project 25020701 (Numerical Hydrodynamics).

The authors gratefully acknowledge the support of Drs. N. S. Brar and S. J. Bless who provided the impact experimental data.

Administrative	
1	<input checked="checked" type="checkbox"/>
2	<input type="checkbox"/>
3	<input type="checkbox"/>
4	<input type="checkbox"/>
5	<input type="checkbox"/>
6	<input type="checkbox"/>
7	<input type="checkbox"/>
8	<input type="checkbox"/>
9	<input type="checkbox"/>
10	<input type="checkbox"/>
11	<input type="checkbox"/>
12	<input type="checkbox"/>
13	<input type="checkbox"/>
14	<input type="checkbox"/>
15	<input type="checkbox"/>
16	<input type="checkbox"/>
17	<input type="checkbox"/>
18	<input type="checkbox"/>
19	<input type="checkbox"/>
20	<input type="checkbox"/>
21	<input type="checkbox"/>
22	<input type="checkbox"/>
23	<input type="checkbox"/>
24	<input type="checkbox"/>
25	<input type="checkbox"/>
26	<input type="checkbox"/>
27	<input type="checkbox"/>
28	<input type="checkbox"/>
29	<input type="checkbox"/>
30	<input type="checkbox"/>
31	<input type="checkbox"/>
32	<input type="checkbox"/>
33	<input type="checkbox"/>
34	<input type="checkbox"/>
35	<input type="checkbox"/>
36	<input type="checkbox"/>
37	<input type="checkbox"/>
38	<input type="checkbox"/>
39	<input type="checkbox"/>
40	<input type="checkbox"/>
41	<input type="checkbox"/>
42	<input type="checkbox"/>
43	<input type="checkbox"/>
44	<input type="checkbox"/>
45	<input type="checkbox"/>
46	<input type="checkbox"/>
47	<input type="checkbox"/>
48	<input type="checkbox"/>
49	<input type="checkbox"/>
50	<input type="checkbox"/>
51	<input type="checkbox"/>
52	<input type="checkbox"/>
53	<input type="checkbox"/>
54	<input type="checkbox"/>
55	<input type="checkbox"/>
56	<input type="checkbox"/>
57	<input type="checkbox"/>
58	<input type="checkbox"/>
59	<input type="checkbox"/>
60	<input type="checkbox"/>
61	<input type="checkbox"/>
62	<input type="checkbox"/>
63	<input type="checkbox"/>
64	<input type="checkbox"/>
65	<input type="checkbox"/>
66	<input type="checkbox"/>
67	<input type="checkbox"/>
68	<input type="checkbox"/>
69	<input type="checkbox"/>
70	<input type="checkbox"/>
71	<input type="checkbox"/>
72	<input type="checkbox"/>
73	<input type="checkbox"/>
74	<input type="checkbox"/>
75	<input type="checkbox"/>
76	<input type="checkbox"/>
77	<input type="checkbox"/>
78	<input type="checkbox"/>
79	<input type="checkbox"/>
80	<input type="checkbox"/>
81	<input type="checkbox"/>
82	<input type="checkbox"/>
83	<input type="checkbox"/>
84	<input type="checkbox"/>
85	<input type="checkbox"/>
86	<input type="checkbox"/>
87	<input type="checkbox"/>
88	<input type="checkbox"/>
89	<input type="checkbox"/>
90	<input type="checkbox"/>
91	<input type="checkbox"/>
92	<input type="checkbox"/>
93	<input type="checkbox"/>
94	<input type="checkbox"/>
95	<input type="checkbox"/>
96	<input type="checkbox"/>
97	<input type="checkbox"/>
98	<input type="checkbox"/>
99	<input type="checkbox"/>
100	<input type="checkbox"/>
101	<input type="checkbox"/>
102	<input type="checkbox"/>
103	<input type="checkbox"/>
104	<input type="checkbox"/>
105	<input type="checkbox"/>
106	<input type="checkbox"/>
107	<input type="checkbox"/>
108	<input type="checkbox"/>
109	<input type="checkbox"/>
110	<input type="checkbox"/>
111	<input type="checkbox"/>
112	<input type="checkbox"/>
113	<input type="checkbox"/>
114	<input type="checkbox"/>
115	<input type="checkbox"/>
116	<input type="checkbox"/>
117	<input type="checkbox"/>
118	<input type="checkbox"/>
119	<input type="checkbox"/>
120	<input type="checkbox"/>
121	<input type="checkbox"/>
122	<input type="checkbox"/>
123	<input type="checkbox"/>
124	<input type="checkbox"/>
125	<input type="checkbox"/>
126	<input type="checkbox"/>
127	<input type="checkbox"/>
128	<input type="checkbox"/>
129	<input type="checkbox"/>
130	<input type="checkbox"/>
131	<input type="checkbox"/>
132	<input type="checkbox"/>
133	<input type="checkbox"/>
134	<input type="checkbox"/>
135	<input type="checkbox"/>
136	<input type="checkbox"/>
137	<input type="checkbox"/>
138	<input type="checkbox"/>
139	<input type="checkbox"/>
140	<input type="checkbox"/>
141	<input type="checkbox"/>
142	<input type="checkbox"/>
143	<input type="checkbox"/>
144	<input type="checkbox"/>
145	<input type="checkbox"/>
146	<input type="checkbox"/>
147	<input type="checkbox"/>
148	<input type="checkbox"/>
149	<input type="checkbox"/>
150	<input type="checkbox"/>
151	<input type="checkbox"/>
152	<input type="checkbox"/>
153	<input type="checkbox"/>
154	<input type="checkbox"/>
155	<input type="checkbox"/>
156	<input type="checkbox"/>
157	<input type="checkbox"/>
158	<input type="checkbox"/>
159	<input type="checkbox"/>
160	<input type="checkbox"/>
161	<input type="checkbox"/>
162	<input type="checkbox"/>
163	<input type="checkbox"/>
164	<input type="checkbox"/>
165	<input type="checkbox"/>
166	<input type="checkbox"/>
167	<input type="checkbox"/>
168	<input type="checkbox"/>
169	<input type="checkbox"/>
170	<input type="checkbox"/>
171	<input type="checkbox"/>
172	<input type="checkbox"/>
173	<input type="checkbox"/>
174	<input type="checkbox"/>
175	<input type="checkbox"/>
176	<input type="checkbox"/>
177	<input type="checkbox"/>
178	<input type="checkbox"/>
179	<input type="checkbox"/>
180	<input type="checkbox"/>
181	<input type="checkbox"/>
182	<input type="checkbox"/>
183	<input type="checkbox"/>
184	<input type="checkbox"/>
185	<input type="checkbox"/>
186	<input type="checkbox"/>
187	<input type="checkbox"/>
188	<input type="checkbox"/>
189	<input type="checkbox"/>
190	<input type="checkbox"/>
191	<input type="checkbox"/>
192	<input type="checkbox"/>
193	<input type="checkbox"/>
194	<input type="checkbox"/>
195	<input type="checkbox"/>
196	<input type="checkbox"/>
197	<input type="checkbox"/>
198	<input type="checkbox"/>
199	<input type="checkbox"/>
200	<input type="checkbox"/>
201	<input type="checkbox"/>
202	<input type="checkbox"/>
203	<input type="checkbox"/>
204	<input type="checkbox"/>
205	<input type="checkbox"/>
206	<input type="checkbox"/>
207	<input type="checkbox"/>
208	<input type="checkbox"/>
209	<input type="checkbox"/>
210	<input type="checkbox"/>
211	<input type="checkbox"/>
212	<input type="checkbox"/>
213	<input type="checkbox"/>
214	<input type="checkbox"/>
215	<input type="checkbox"/>
216	<input type="checkbox"/>
217	<input type="checkbox"/>
218	<input type="checkbox"/>
219	<input type="checkbox"/>
220	<input type="checkbox"/>
221	<input type="checkbox"/>
222	<input type="checkbox"/>
223	<input type="checkbox"/>
224	<input type="checkbox"/>
225	<input type="checkbox"/>
226	<input type="checkbox"/>
227	<input type="checkbox"/>
228	<input type="checkbox"/>
229	<input type="checkbox"/>
230	<input type="checkbox"/>
231	<input type="checkbox"/>
232	<input type="checkbox"/>
233	<input type="checkbox"/>
234	<input type="checkbox"/>
235	<input type="checkbox"/>
236	<input type="checkbox"/>
237	<input type="checkbox"/>
238	<input type="checkbox"/>
239	<input type="checkbox"/>
240	<input type="checkbox"/>
241	<input type="checkbox"/>
242	<input type="checkbox"/>
243	<input type="checkbox"/>
244	<input type="checkbox"/>
245	<input type="checkbox"/>
246	<input type="checkbox"/>
247	<input type="checkbox"/>
248	<input type="checkbox"/>
249	<input type="checkbox"/>
250	<input type="checkbox"/>
251	<input type="checkbox"/>
252	<input type="checkbox"/>
253	<input type="checkbox"/>
254	<input type="checkbox"/>
255	<input type="checkbox"/>
256	<input type="checkbox"/>
257	<input type="checkbox"/>
258	<input type="checkbox"/>
259	<input type="checkbox"/>
260	<input type="checkbox"/>
261	<input type="checkbox"/>
262	<input type="checkbox"/>
263	<input type="checkbox"/>
264	<input type="checkbox"/>
265	<input type="checkbox"/>
266	<input type="checkbox"/>
267	<input type="checkbox"/>
268	<input type="checkbox"/>
269	<input type="checkbox"/>
270	<input type="checkbox"/>
271	<input type="checkbox"/>
272	<input type="checkbox"/>
273	<input type="checkbox"/>
274	<input type="checkbox"/>
275	<input type="checkbox"/>
276	<input type="checkbox"/>
277	<input type="checkbox"/>
278	<input type="checkbox"/>
279	<input type="checkbox"/>
280	<input type="checkbox"/>
281	<input type="checkbox"/>
282	<input type="checkbox"/>
283	<input type="checkbox"/>
284	<input type="checkbox"/>
285	<input type="checkbox"/>
286	<input type="checkbox"/>
287	<input type="checkbox"/>
288	<input type="checkbox"/>
289	<input type="checkbox"/>
290	<input type="checkbox"/>
291	<input type="checkbox"/>
292	<input type="checkbox"/>
293	<input type="checkbox"/>
294	<input type="checkbox"/>
295	<input type="checkbox"/>
296	<input type="checkbox"/>
297	<input type="checkbox"/>
298	<input type="checkbox"/>
299	<input type="checkbox"/>
300	<input type="checkbox"/>
301	<input type="checkbox"/>
302	<input type="checkbox"/>
303	<input type="checkbox"/>
304	<input type="checkbox"/>
305	<input type="checkbox"/>
306	<input type="checkbox"/>
307	<input type="checkbox"/>
308	<input type="checkbox"/>
309	<input type="checkbox"/>
310	<input type="checkbox"/>
311	<input type="checkbox"/>
312	<input type="checkbox"/>
313	<input type="checkbox"/>
314	<input type="checkbox"/>
315	<input type="checkbox"/>
316	<input type="checkbox"/>
317	<input type="checkbox"/>
318	<input type="checkbox"/>
319	<input type="checkbox"/>
320	<input type="checkbox"/>
321	<input type="checkbox"/>
322	<input type="checkbox"/>
323	<input type="checkbox"/>
324	<input type="checkbox"/>
325	<input type="checkbox"/>
326	<input type="checkbox"/>
327	<input type="checkbox"/>
328	<input type="checkbox"/>
329	<input type="checkbox"/>
330	<input type="checkbox"/>
331	<input type="checkbox"/>
332	<input type="checkbox"/>
333	<input type="checkbox"/>
334	<input type="checkbox"/>
335	<input type="checkbox"/>
336	<input type="checkbox"/>
337	<input type="checkbox"/>
338	<input type="checkbox"/>
339	<input type="checkbox"/>
340	<input type="checkbox"/>
341	<input type="checkbox"/>
342	<input type="checkbox"/>
343	<input type="checkbox"/>
344	<input type="checkbox"/>
345	<input type="checkbox"/>
346	<input type="checkbox"/>
347	<input type="checkbox"/>
348	<input type="checkbox"/>
349	<input type="checkbox"/>
350	<input type="checkbox"/>
351	<input type="checkbox"/>
352	<input type="checkbox"/>
353	<input type="checkbox"/>
354	<input type="checkbox"/>
355	<input type="checkbox"/>
356	<input type="checkbox"/>
357	<input type="checkbox"/>
358	<input type="checkbox"/>
359	<input type="checkbox"/>
360	<input type="checkbox"/>
361	<input type="checkbox"/>
362	<input type="checkbox"/>
363	<input type="checkbox"/>
364	<input type="checkbox"/>
365	<input type="checkbox"/>
366	<input type="checkbox"/>
367	<input type="checkbox"/>
368	<input type="checkbox"/>
369	<input type="checkbox"/>
370	<input type="checkbox"/>
371	<input type="checkbox"/>
372	<input type="checkbox"/>
373	<input type="checkbox"/>
374	<input type="checkbox"/>
375	<input type="checkbox"/>
376	<input type="checkbox"/>
377	<input type="checkbox"/>
378	<input type="checkbox"/>
379	<input type="checkbox"/>
380	<input type="checkbox"/>
381	<input type="checkbox"/>
382	<input type="checkbox"/>
383	<input type="checkbox"/>
384	<input type="checkbox"/>
385	<input type="checkbox"/>
386	<input type="checkbox"/>
387	<input type="checkbox"/>
388	<input type="checkbox"/>
389	<input type="checkbox"/>
390	<input type="checkbox"/>
391	<input type="checkbox"/>
392	<input type="checkbox"/>
393	<input type="checkbox"/>
394	<input type="checkbox"/>
395	<input type="checkbox"/>
396	<input type="checkbox"/>
397	<input type="checkbox"/>
398	<input type="checkbox"/>
399	<input type="checkbox"/>
400	<input type="checkbox"/>
401	<input type="checkbox"/>
402	<input type="checkbox"/>
403	<input type="checkbox"/>
404	<input type="checkbox"/>
405	<input type="checkbox"/>
406	<input type="checkbox"/>
407	<input type="checkbox"/>
408	<input type="checkbox"/>
409	<input type="checkbox"/>
410	<input type="checkbox"/>
411	<input type="checkbox"/>
412	<input type="checkbox"/>
413	<input type="checkbox"/>
414	<input type="checkbox"/>
415	<input type="checkbox"/>
416	<input type="checkbox"/>
417	<input type="checkbox"/>
418	<input type="checkbox"/>
419	<input type="checkbox"/>
420	<input type="checkbox"/>
421	<input type="checkbox"/>
422	<input type="checkbox"/>
423	<input type="checkbox"/>
424	<input type="checkbox"/>
425	<input type="checkbox"/>
426	<input type="checkbox"/>
427	<input type="checkbox"/>
428	<input type="checkbox"/>
429	<input type="checkbox"/>
430	<input type="checkbox"/>
431	<input type="checkbox"/>
432	<input type="checkbox"/>
433	<input type="checkbox"/>
434	<input type="checkbox"/>
435	<input type="checkbox"/>
436	<input type="checkbox"/>
437	<input type="checkbox"/>
438	<input type="checkbox"/>
439	<input type="checkbox"/>
440	<input type="checkbox"/>
441	<input type="checkbox"/>
442	<input type="checkbox"/>
443	<input type="checkbox"/>
444	<input type="checkbox"/>
445	<input type="checkbox"/>
446	<input type="checkbox"/>
447	<input type="checkbox"/>
448	<input type="checkbox"/>
449	<input type="checkbox"/>
450	<input type="checkbox"/>
451	<input type="checkbox"/>
452	<input type="checkbox"/>
453	<input type="checkbox"/>
454	<input type="checkbox"/>
455	<input type="checkbox"/>
456	<input type="checkbox"/>
457	<input type="checkbox"/>
458	<input type="checkbox"/>
459	<input type="checkbox"/>
460	<input type="checkbox"/>
461	<input type="checkbox"/>
462	<input type="checkbox"/>
463	<input type="checkbox"/>
464	<input type="checkbox"/>
465	<input type="checkbox"/>
466	<input type="checkbox"/>
467	<input type="checkbox"/>
468	<input type="checkbox"/>
469	<input type="checkbox"/>
470	<input type="checkbox"/>
471	<input type="checkbox"/>
472	<input type="checkbox"/>
473	<input type="checkbox"/>
474	<input type="checkbox"/>
475	<input type="checkbox"/>
476	<input type="checkbox"/>
477	<input type="checkbox"/>
478	<input type="checkbox"/>
479	<input type="checkbox"/>
480	<input type="checkbox"/>
481	<input type="checkbox"/>
482	<input type="checkbox"/>
483	<input type="checkbox"/>
484	<input type="checkbox"/>
485	<input type="checkbox"/>
486	<input type="checkbox"/>
487	<input type="checkbox"/>
488	<input type="checkbox"/>
489	<input type="checkbox"/>
490	<input type="checkbox"/>
491	<input type="checkbox"/>
492	<input type="checkbox"/>
493	<input type="checkbox"/>
494	<input type="checkbox"/>
495	<input type="checkbox"/>
496	<input type="checkbox"/>
497	<input type="checkbox"/>
498	<input type="checkbox"/>
499	<input type="checkbox"/>
500	<input type="checkbox"/>
501	<input type="checkbox"/>
502	<input type="checkbox"/>
503	<input type="checkbox"/>
504	<input type="checkbox"/>
505	<input type="checkbox"/>
506	<input type="checkbox"/>
507	<input type="checkbox"/>
508	<input type="checkbox"/>
509	<input type="checkbox"/>
510	<input type="checkbox"/>
511	<input type="checkbox"/>
512	<input type="checkbox"/>
513	<input type="checkbox"/>
514	<input type="checkbox"/>
515	<input type="checkbox"/>
516	<input type="checkbox"/>
517	<input type="checkbox"/>
518	<input type="checkbox"/>
519	<input type="checkbox"/>
520	<input type="checkbox"/>
521	<input type="checkbox"/>
522	<input type="checkbox"/>
523	<input type="checkbox"/>
524	<input type="checkbox"/>
525	<input type="checkbox"/>
526	<input type="checkbox"/>
527	<input type="checkbox"/>
528	<input type="checkbox"/>
529	<input type="checkbox"/>
530	<input type="checkbox"/>
531	<input type="checkbox"/>
532	<input type="checkbox"/>
533	<input type="checkbox"/>
534	<input type="checkbox"/>
535	<input type="checkbox"/>
536	<input type="checkbox"/>
537	<input type="checkbox"/>
538	<input type="checkbox"/>
539	<input type="checkbox"/>
540	<input type="checkbox"/>
541	<input type="checkbox"/>
542	<input type="checkbox"/>
543	<input type="checkbox"/>
544	<input type="checkbox"/>
545	<input type="checkbox"/>
546	<input type="checkbox"/>
547	<input type="checkbox"/>
548	<input type="checkbox"/>
549	<input type="checkbox"/>
550	<input type="checkbox"/>
551	<input type="checkbox"/>
552	<input type="checkbox"/>
553	<input type="checkbox"/>
554	<input type="checkbox"/>
555	<input type="checkbox"/>
556	<input type="checkbox"/>
557	<input type="checkbox"/>
558	<input type="checkbox"/>
559	<input type="checkbox"/>
560	<input type="checkbox"/>
561	<input type="checkbox"/>
562	<input type="checkbox"/>
563	<input type="checkbox"/>
564	<input type="checkbox"/>
565	<input type="checkbox"/>
566	<input type="checkbox"/>
567	<input type="checkbox"/>
568	<input type="checkbox"/>
569	<input type="checkbox"/>
570	<input type="checkbox"/>
571	<input type="checkbox"/>
572	<input type="checkbox"/>
573	<input type="checkbox"/>
574	<input type="checkbox"/>
575	

TABLE OF CONTENTS

<u>SECTION</u>	<u>PAGE</u>
1. INTRODUCTION	1
2. BACKGROUND	3
3. FAILURE MODEL FORMULATION.	6
3.1 Bodner-Partom Model.	6
3.2 Johnson-Cook Model	9
3.3 Nucleation and Growth Voids.	9
3.4 Pressure Dependent Plastic Flow of the Aggregate	12
3.5 Degradation of Shear and Bulk Moduli	14
3.6 Equation of State for the Aggregate.	15
4. FAILURE ANALYSES USING THE RDG MODEL	16
4.1 Plate Impact Simulations	16
4.1.1 Physical Features.	17
4.1.2 Stability of the Solution.	22
4.1.3 Sensitivity Study.	24
4.2 Model Parameters	26
5. MODELING OF VOID COLLAPSE UNDER MULTIPLE SHOCKING.	37
5.1 Double Flyer Plate Impact Experiment.	40
6. RDG MODEL APPLICATIONS	47
6.1 Tensile Necking.	47
6.2 Application of RDG Model to Rod Penetration Problem.	73
6.3 Spall in a Solid Cone Target	85
7. SUMMARY AND CONCLUSIONS.	89
8. REFERENCES	92
 <u>APPENDICES</u>	 <u>PAGE</u>
A NUMERICAL SOLUTION OF THE GOVERNING EQUATIONS IN SECTION 3	96
B THE DIAGONALLY IMPLICIT RUNGE DUTTA (DIRK) SCHEME WITH TIME STEP CONTROL.	99

LIST OF ILLUSTRATIONS

<u>Figure</u>		<u>Page</u>
1.	Simulated Velocity History for a Target without and with Spall Failure.	18
2.	Simulated Free Surface Velocity Histories at Different Velocities.	19
3.	Simulated Stress History at the Spall Plane. Stress Relaxation under Tension is Shown for Three Impact Velocities.	20
4.	Model Simulated Void Distribution in the Impacted Target Plate for $t = 3, 4$, and 6 Microseconds	21
5.	The Loading Path at the Spall Plane in a Simulation	23
6.	Demonstration of Grid (or mesh) Independency of the Solution for Three Different Grids at Two Velocities	25
7.	Comparison Between Model Simulation and the Experimental Data of the Free Surface Velocity History.	29
8.	(a) Comparison Between Model and the Measured Stress History (HY100 steel). (b) Numerical Simulation of the Stress History at the Spall Plane (HY100 steel).	32
9.	Comparisons Between RDG Model Generated and Experimental Stress Gauge for Different Metals	34
10.	Comparisons Between RDG Model Generated and Experimental Stress Gauge Signals for Different Metals	35
11.	Comparisons of Spall Modeling for HY100 Steel Using BP and JC Models. Spall Process is Described by the RDG Model. . .	36
12.	Comparisons Between the Spall Signals Generated Using JC and BP Models for Different Values of RDG Model Constants. . . .	38
13.	Comparison Between Model Prediction and the Measure Stress History (OFHC Copper).	39
14.	Experiment Configuration for Double Flyer Impact Experiment.	41
15.	Stress History Comparison for Original RDG Model	42
16.	Stress History Comparison for Modified RDG Model, with a Critical Void Volume Fraction of 5% for Complete Collapse. .	43
17.	Comparison of Simulated Stress Histories from Double Flyer Impact Configuration, With and Without Void Growth	45

18.	x-t Diagram for the Souble Flyer Impact Experiment, Assuming No Void Growth	46
19.	Shallow-notched Tensile Specimen Geometry.	48
20.	Finite Element Mesh for Shallow-notched SHB Specimen. The Velocity Loading History is Shown in the Inset	49
21.	Stress Triaxiality (P/Y) at (a) t=40, (b) t=50, and (c) t=60 Microseconds	51
22.	Damage (Void Volume Fraction) Contour at (a) t=0, (b) t=20, (c) t=50, and (d) t=60 Microseconds.	52
	Concluded.	53
23.	Time Histories of Effective Plastic Strain and Void Volume Fraction for Elements #82 (Uniform Section) and #382 (local section)	54
24.	Time History Plots for the Stress Components and Void Volume Fraction	56
25.	Stress-strain Response for #82 and #382 Among with the Variation of f with Respect to Effective Plastic Strain. . .	57
26.	Time History Plot of Mean Stress for Elements #82, 182, 282 and 382	58
27.	Measure of Triaxiality with Respect to Time for the Uniform (#82) and Local (#382) Sections.	59
28.	Loading Paths with Respect to Pressure Dependent Yield Surfaces in Elements #82, 182, 282, and 382.	60
29.	Radial Distribution of Void Volume Fraction at These Different Positions Along the Specimen Length.	63
30.	Normalized Effective Stress Distribution Along the Radius for Different z Positions and Time Intervals	64
31.	Comparisons of Failure Strain for Tensile Necking With and Without Voids. The Solid Line Without Symbols is an Average Measure of Strain Based on the Pull Velocity	66
32.	Comparison of σ_{eff} versus ϵ_{eff}^P for Tensile Necking With and Without Voids.	67
33.	Radial Distributions of ϵ_{eff}^P for Cases With and Without Voids, Plotted for Elements in Uniform (#182) and Local (#382) Sections.	68
34.	Measure of Triaxiality ($P \sigma_{eff}$) along the Radius for Cases With and Without Voids	70

35.	Pressure Contour Plot for Void-Growth Influenced Necking Process. The Shaded Region is Under Tensile Loading, and the Rest of the Region Experiences Compressive Loading	71
36.	Initial (dotted) and Final (full) Shapes of the Shallow Notch Tensile Specimens.	72
37.	Finite Element Mesh for the Rod Penetration Problem.	74
38.	Measure of Triaxiality, Ratio of Pressure (mean stress) and Strength (effective stress), Void Volume Fraction with Respect to Time.	75
39.	Effect of Void Volume Fraction, f (porosity) on the Aggregate Strength. The Matrix Strength (Y_m) is Independent of f	77
40.	The Loading Path (solid line) with Respect to the Pressure Dependent Yield Surfaces	79
41.	Distributions of Aggregate Strength (Y_a) Along the Target Radius at Two Different Times.	80
42.	Damage Contours at Various Stages in the Rod Penetration	82
43.	Comparisons of Yield Strength (Y) With and Without Voids. Y_m is the Matrix Strength of Void ^a Containing Material. . . .	83
44.	Deformed Configurations at 20 μ sec, With and Without Void Growth	84
45.	(a) Schematic Two Dimensional Sketch of a Flyer Plate Impact on the Base of a Right Solid Cone (b) Recovered and Sectioned Solid Cone Revealing the Complex Spall Zones	86
46.	The Finite Element Mesh of the Cone Impact Geometry at (a) $t=0$ and (b) $t=60$ microseconds.	87
47.	The Damage (Void Volume Fraction) Contour at (a) $t=5$ and (b) $t=60$ microseconds.	88

<u>Table</u>		<u>Page</u>
1.	Bodner-Partom Model Constants.	8
2.	Strength Model Constants for Johnson-Cook Model.	10
3.	Plate Impact Experiments	27
4.	RDG Model Constants.	27

1. INTRODUCTION

High velocity impact loading generates high pressures, very high strain rates, and high temperatures. Most structural alloys exhibit strain rate dependent material behavior under high strain rates ($>1000/\text{sec}$). The constitutive description of structural alloys under impact loading must therefore incorporate the effects of pressure, strain rate, temperature, and loading history on strength and plastic deformation. Material strength increases with increasing strain rates. Depending on the various levels and conditions of these variables, the failure mechanisms can change widely. For instance, at rapid plastic deformations, the thermal softening of materials enhances the formation of localized adiabatic shear bands. High tensile pressures are often generated due to wave interactions. These pressures can cause void nucleation and growth. The use of advanced, continuum mechanics based, three dimensional, thermoviscoplastic constitutive and failure models incorporating these physical features is essential for accurate computer code calculations of practical impact engineering problems.

Ductile material failure is often accompanied by nucleation and growth of microvoids. Most initially intact structural alloys develop microvoids/microcracks during plastic deformation under both quasi-static and dynamic loading conditions. The nucleation process is often controlled either by the stress (tensile pressure) or by the strain state experienced by the material. For instance, in the biaxial stretching of a thin sheet, the process is controlled by plastic deformation. However, in a plane plate impact (uniaxial strain) condition, the void nucleation is controlled by the high tensile stresses generated due to shock wave interactions. The nucleation threshold strain under a uniaxial stress state is always orders of magnitude higher than under uniaxial strain. In general, the high triaxial stress state enhances the ductile void growth process. The modeling of the ductile failure process requires careful consideration of the influence and sensitivity of stress/strain states as well as strain rates on the nucleation and growth processes of microvoids.

The main objective of this report is to describe the recently developed dynamic failure model [1] and its applications in detail. However, prior to describing this model, the authors provided a comprehensive background on

dynamic failure models for ductile metals in Section 2. The essential equations of the model are given in Section 3. A few application problems are described in Section 4. For example, spallation in a target due to a long rod penetration, necking in a dynamically stretched tensile specimen, a spallation in a solid cone impacted by a flyer plate on its base are simulated using the failure model. In the summary section, the salient features of the new failure model are discussed and recommendations for additional experiments and computer simulations. The numerical solution scheme of the governing equations is discussed in Appendix A and B.

2. BACKGROUND

Numerous journal articles, technical reports, and conference proceedings on dynamic failure models exist. Investigators with widely varying backgrounds, such as applied mechanicians, metallurgists, and shock physicists, have contributed to the understanding of dynamic ductile failure. Based on the metallurgical evidence, Argon et al. [2] suggested that one of the most often observed void nucleation processes is the debonding of the matrix material from the second phase particles. Several other metallurgical investigations support this evidence [3-5]. McClintock [6] proposed theories describing growth of cylindrical voids and their subsequent coalescence. Rice and Tracey [7] considered the growth kinetics of a single spherical void in an infinite matrix material and described mathematically the dependence of void growth on triaxiality of the stress state. Gurson [8] derived a pressure dependent yield condition for porous metals. Using this condition, he proposed a void growth law similar to Rice and Tracey's. Hancock and MacKenzie [9] provided the experimental evidence to support this dependency on the stress state and used this model to predict failure initiation in notched tensile specimens under quasi-static loading conditions. However, the mean stress (pressure) level in their study is relatively low when compared with the level in a plate impact test configuration. Also, the strain rate effects become important under impact loading conditions.

In a plate impact test, tension arising from the interactions of reflected shock waves from the stress free planes parallel to the plane of impact induces fracture in the target. Void nucleation and growth occur under very high triaxial stress leading to the generation of a stress free plane inside the target through coalescence of the voids. This type of failure is often referred to as spallation. A simple criterion in which stress or pressure is assumed to reach a critical value is usually employed to model spallation in computer code calculations. This type of time independent failure model may work well when the spall is well above the threshold conditions. Tuler and Butcher [10] proposed a time dependent spall criterion in which the integrated value of a stress dependent damage parameter is assumed to reach a critical value. The criterion assumes that spall occurs if the material is subjected to a stress greater than some threshold level for a sufficient characteristic time. In this model, the damage parameter does not

degrade either the stiffness or the strength. This model has three parameters which have to be determined from the spall experiments. Rajendran and Bless [11] determined the Tuler-Butcher model constants for several metals.

Cochran and Banner [12] proposed a relatively advanced model to describe the spallation. This model incorporates the effects of void nucleation and growth on the strength calculation in a simplistic manner. The stress is allowed to relax due to damage evolution. The main shortcoming of this model is that it is limited to only rectilinear motions (one dimensional strain). Steinberg et al. [13] successfully applied this model in conjunction with viscoplastic constitutive models to describe the spall phenomenon in several metals. The dynamic failure process in metals was extensively modeled using a microstatistical approach by Curran et al. [14-16]. This relatively complex, but conceptually advanced, computational model pioneered the statistical nature of the nucleation process and the pressure driven void growth process. They also phenomenologically modeled the coalescence process. This model contained a number of parameters determined from the direct measurements of voids in the target of a carefully conducted recovery experiment. Therefore, the determination of the failure model parameters is unfortunately complex and time consuming. The constitutive equation of the matrix material is relatively simple and the strength degradation is handled in an ad hoc manner, rather than through a continuum mechanics based three dimensional approach. However, the effects of damage on stiffness and strength are incorporated in a manner which leads to numerically efficient solutions.

Recently Curran, Seaman, and Shockey [16] described their model in detail and provided an in-depth investigation of the dynamic failure process in both ductile and brittle metals. Davison et al. [17] presented a theory of spall damage based on a unified and thermodynamically consistent treatment of elastic-viscoplastic deformation. A continuum mechanics approach was employed with a three dimensional theory. They considered a detailed dislocation based thermoviscoplastic constitutive model for the matrix material behavior. This complete treatment of material flow and failure process led to numerous model constants which are not easily obtainable.

Johnson and Addessio [18] described their approach to model tensile plasticity and ductile fracture. They proposed a model valid for general tensile loading conditions. Therefore, this model focused on describing plastic

flow and fracture in notched and smooth bars as well as spallation under uniaxial strain conditions. For a simplistic approach, the nucleation of voids is assumed to occur instantaneously, and a small initial void content is assigned to the void volume fraction. The plastic flow was described by the associative flow rule derived from Gurson's yield surface [8]. The growth law reduces to an equation derived by Carroll and Holt [19] for tensile threshold pressure. The matrix material behavior is described through a rate independent perfectly plastic model. The plastic flow in the porous aggregate is also rate independent. Numerical results from three different (one dimensional strain, two dimensional stress, and one dimensional stress) calculations were presented to demonstrate the model capabilities.

Rajendran [20], and Rajendran, Dietersberger, and Grove [1] presented a three dimensional, continuum mechanics based dynamic failure model (RDG Model) to describe spallation in two dimensional stress (long rod impact on a thick plate) and one dimensional strain (plane plate impact). The RDG model considered a viscoplastic constitutive description for the matrix and the porous aggregate materials. The stress and strain based void nucleation process was modeled through a Gaussian distribution, as initially proposed by Chu and Needleman [21] to describe strain rate independent nucleation process in thin sheet stretching. The RDG model proposed a new pressure dependent yield function for describing plastic flow in the porous aggregate. There are four phases in the model. In the first phase, the intact material is described by the Bodner-Partom viscoplastic model [22]. The void nucleation is introduced in the second phase. The void-contained aggregate is described in the third phase using an associated plastic flow rule derived from a pressure dependent yield function. The last phase of modeling is the coalescence of voids leading to complete failure. In the RDG model, separate modeling of the coalescence process is not needed. The void growth law is such that the growth rate is rapidly increased as the damage approaches its critical value.

3. FAILURE MODEL FORMULATION

Three of the main features in a dynamic ductile failure model are the following: one, the initial intact (void-free) material requires a constitutive description which will include strain rate and temperature effects; two, a mathematical description of the void nucleation and growth process; and three, pressure dependent plastic flow equations for the porous (void-containing) aggregate. There could be several other features in the failure modeling. For instance, depending on the level of voids, the stiffness of the aggregate may significantly be reduced; therefore, models to degrade the stiffness will be required for the realistic description of the material behavior. The final process of voids coalescence may also be important. Another aspect of the failure model is the equation of state for the porous aggregate.

A brief description of the Bodner-Partom (BP) model for the intact (matrix) material is given in this section. As an alternative to BP model, the model proposed by Johnson and Cook (JC) [23] is also described. The model constants for BP and JC are provided for several metals. The model constant evaluation scheme for these two models have been described elsewhere, reference [24] for the BP model and reference [25] for JC model.

3.1 Bodner-Partom Model

The fully densified, void-free matrix material can be modeled through the state variable based viscoplastic constitutive equations of Bodner and Partom (B-P model) [22]. The B-P model in terms of equivalent plastic strain rate, $\dot{\epsilon}_m^p$, and effective stress, σ_m , is given by,

$$\dot{\epsilon}_m^p = \frac{2}{\sqrt{3}} D_0 \exp\left\{-\left(\frac{n+1}{2n}\right) \left(\frac{Z}{\sigma_m}\right)^{2n}\right\} \quad (1)$$

where Z is a state variable. D_0 is the limiting value of the plastic strain rate. The value of D_0 is usually set to 10^8 /sec for metals. n is a parameter that is mainly related to strain rate sensitivity. The state variable Z describes the overall resistance of the material to plastic flow, and it

depends on the loading history. The evolution equation for the loading history parameter Z is

$$\dot{Z} = m(Z_1 - Z) \dot{W}_p \quad (2)$$

where \dot{W}_p is the plastic work rate. Z_1 is the maximum value that Z can attain, and m is a parameter that embodies the strain hardening behavior of the material. For highly strain hardening materials like copper, m is described by,

$$m = m_0 + m_1 e^{-\alpha W_p} \quad (3)$$

where m_0 , m_1 and α are additional model parameters. For less strain hardening materials, m_1 and α are assumed to be zero. For example, the modeling of OFHC copper required the additional two constants.

The high temperature effect on the strength (thermal softening) is incorporated simplistically through the strain rate sensitivity constant, n . Experimental evidence suggests that at elevated temperatures metals exhibit increased rate dependency. The temperature dependent n is described by,

$$n = A + B / T_K^0 \quad (4)$$

where the temperature is expressed in degrees Kelvin. A and B are additional BP model constants. Previously, Rajendran et al. [24] presented a systematic scheme for evaluating the model constants. They determined the B-P model parameters from split Hopkinson bar experimental data and the steady state value of σ_{HEL} . The BP model constants for several metals have been determined and tabulated in Table 1. Z_0 is the initial value of Z . The D_0 is assumed to be the same for all metals, and a value of 10^8 /sec has been arbitrarily assigned. In his review report, Bodner [26] suggested a value of 10^7 /sec based on dislocation motion measurements for high velocity impact loading conditions. A lower value for the strain rate sensitivity parameter n indicates that the material is extremely strain rate sensitive. The C1008 steel is an example. The value of 4 for 6061-T6 aluminum indicates that the material is the least strain rate dependent. When the difference between Z_0 and Z_1 is small, the material is relatively less strain hardening. For OFHC copper the difference is significantly high which means high strain hardening behavior.

TABLE 1
BODNER-PARTOM MODEL CONSTANTS

Material	Z_0 (GPa)	Z_1 (GPa)	n	m_0 GPa ⁻¹	m_1 GPa ⁻¹	α GPa ⁻¹	A	B
C1008 Steel	5.5	7.0	0.4	15	0	0	0.245	46
HY100 Steel	2.4	3.6	1.2	10	0	0	NA	NA
1020 Steel	0.64	0.93	4.0	30	0	0	NA	NA
MAR-200 Steel	2.2	2.4	4.0	5	0	0	NA	NA
Armco Iron	2.65	4.2	0.58	56	0	0	NA	NA
OFHC Copper	0.8	6.6	0.4	11	150	1500	NA	NA
6061-T6 Aluminum	0.45	0.55	4.0	120	0	0	-2.86	2343
7039-T64 Aluminum	0.56	0.76	4.0	28	0	0	NA	NA
Pure Tantalum	1.3	3.1	0.74	20	0	0	NA	NA
W-2 Tungsten	8.75	10.0	0.58	150	0	0	0.166	134
Nickel 200	0.32	0.82	4.0	40	0	0	NA	NA
MAR-250 Steel	2.5	2.7	5.0	20	0	0	NA	NA
AF1410 Steel	2.4	2.75	5.0	15	0	0	NA	NA

NA -- The high temperature constants are "Not Available"

3.2 Johnson-Cook Model

The Johnson-Cook constitutive model was used as a basis of comparison for this study. This model is basically an empirical model which incorporates strain rate and temperature dependency on strength. The plastic strain rates are not bounded and therefore are not restricted below any limiting value. Also, no loading history effects are built into the model. However, this five-parameter empirical model has been demonstrated to provide realistic solutions to hydrocode predictions of a very broad class of applications to extremely dynamic events such as impact, penetration, and explosive acceleration of metals. The success of the model is due to its ability to incorporate the overall effects of temperature and strain rate as observed from the dynamic and quasi-static experimental data. The Johnson-Cook model has the following form:

$$Y = [A + B \bar{\epsilon}^n] [1 + C \ln \hat{\epsilon}^*] [1 - T^{*M}] \quad (5)$$

$$T^* = \frac{T - T_{\text{room}}}{T_{\text{melt}} - T_{\text{room}}} \quad (6)$$

where Y is the flow strength, $\bar{\epsilon}$ is effective plastic strain, $\hat{\epsilon}^*$ is non-dimensional strain rate (normalized by 1/sec). The five material constants are the following: A is the yield strength, B is the work hardening coefficient, n is the work hardening exponent, C is strain rate coefficient, and M is the thermal softening exponent. In Table 2, the values of these constants are tabulated for various metals.

The model constants A , B , and n are determined from quasi-static stress-strain data either from tensile or compressive tests. The strain rate dependent constant C can be determined from the slope of the stress versus strain rate plot. The temperature constant M is estimated from the stress versus temperature plot. In hydrocode analysis, strain rate, and the von-Mises yield radius can be calculated from the JC equation for a given strain and temperature.

3.3 Nucleation and Growth of Voids

Until voids nucleate, the aggregate behavior can be described by the P model. The plastic flow in the void-free aggregate is incompressible, i.e

TABLE 2

STRENGTH MODEL CONSTANTS FOR JOHNSON-COOK MODEL

MATERIAL	A MPa	B MPa	C	n	M	REMARKS
OFHC Copper	89.63	291.64	0.025	0.31	1.09	800°F, Anneal/60 min.
Cartridge Brass	111.69	504.69	0.009	0.42	1.68	1000°F, Anneal/60 min.
Nickel 200	163.40	648.10	0.006	0.33	1.44	1300°F, Anneal/30 min.
Armco Iron	175.12	3799.90	0.06	0.32	0.55	1700°F, Anneal/60 min.
Carpenter Electric Iron	289.58	338.53	0.055	0.40	0.55	1000°F, Anneal/60 min.
1006 Steel	350.25	275.00	0.022	0.36	1.00	
2024-T351 Aluminum	264.75	426.09	0.015	0.34	1.00	
7039 Aluminum	336.46	342.66	0.01	0.41	1.00	
4340 Steel	792.19	509.51	0.014	0.26	1.03	
S-7 Tool Steel	1538.89	476.42	0.012	0.18	1.00	
Tungsten	1505.79	176.50	0.016	0.12	1.00	7% Ni, 3% Fe
Depleted Uranium	1079.01	1119.69	0.007	0.25	1.00	0.75 Ti
Tantalum	140.00	300.00	*	0.30	0.70	[ref. Lips et al. (1987)]

*not provided

the sum of the principal or orthogonal plastic strains is equal to zero. However, the nucleation of voids will introduce dilatation and the plastic yield behavior will depend not only on the second invariant, J_2 , but also on the mean stress or pressure. The constitutive model for the aggregate must include these effects. For this purpose, a yield-criterion-based plastic flow rule in which the pressure dependence enters explicitly into the calculations was considered.

The most widely used void nucleation model was the one that was initially used by Chu and Needleman [21] in their analysis of localized necking in biaxially stretched sheets. The model was based on a mechanism in which voids are nucleated due to debonding of inclusions from the matrix. The debonding can occur because of a stress or a strain criterion or both. The corresponding model for void nucleation rate is given by,

$$\dot{f}_n = F_\sigma (\dot{Y}_m + \dot{P}) + F_\epsilon \dot{D}_m^P \quad (7)$$

where

$$F_\sigma = \frac{f_1}{s_1 \sqrt{2\pi}} e^{-\frac{1}{2} \left(\frac{Y_m + P - \sigma_N}{s_1} \right)^2} \quad (8)$$

and

$$F_\epsilon = \frac{f_2}{s_2 \sqrt{2\pi}} e^{-\frac{1}{2} \left(\frac{D_m^P - e_N}{s_2} \right)^2} \quad (9)$$

If the nucleation is due to only the matrix debonding from inclusions, then the total void volume nucleated must be consistent with the volume fraction of second phase particles. Therefore, the values determined for the parameters f_1 and f_2 must meet this requirement. σ_N and e_N are the mean equivalent stress and strain, respectively, around which the nucleation stress and strain are distributed in a Gaussian manner. s_1 and s_2 are the standard deviations of the distributions. These two parameters will control the ranges of stress or strain over which most of the voids can be nucleated.

The growth law can be directly related to the dilatation due to growth of voids in the aggregate. By definition, the void growth rate is given by,

$$\dot{f}_g = \rho * \dot{\epsilon}_{ii}^p \quad (10)$$

where repeated index means summation, and $\dot{\epsilon}_{ii}^p$ are plastic strain rates in the three principal directions and $f = 1 - \rho$, where ρ is the relative density. ρ is the ratio of current density to the reference density.

3.4 Pressure Dependent Plastic Flow of the Aggregate

A pressure dependent yield-criterion-based approach has been considered in the constitutive model formulation. For randomly distributed voids or microcracks contained in the aggregate, the yield behavior will be influenced by not only the second invariant of the deviatoric stress (J_2) but also by the pressure or mean stress (I_1). The following form of the yield function has been considered:

$$A(\rho) J_2 + B(\rho) I_1^2 = \delta(\rho) Y_m^2 \quad (11)$$

where A, B, and δ are functions of relative density, ρ . Y_m is the effective stress in the matrix material. (Note: the subscript 'm' means matrix material and not a tensorial index.) Based on a critical total deformation energy, Doraivelu et al. [27] derived the following expressions for A and B:

$$A(\rho) = 2 + \rho^2 \quad (12)$$

and

$$B(\rho) = \frac{1 - \rho^2}{3} \quad (13)$$

In general, the δ function is material dependent while the functions A and B are independent of the matrix material behavior. The conditions on the coefficient of the matrix effective stress in the yield function are $\delta(\rho) = 1$ at $\rho = 1$ and $\delta(\rho) = 0$ at $\rho = \rho_{cr}$. Rajendran et al. [1] proceeded initially with the form

$$\delta(\rho) = \frac{g(\rho) - g(\rho_{cr})}{g(1) - g(\rho_{cr})} \quad (14)$$

which satisfies the conditions on the δ function. Rajendran et al. also proposed a new function for $g(\rho)$ with the form

$$g(\rho) = \left[\kappa - \frac{N}{|N|} (1 - \rho) \right]^N \quad (15)$$

where κ and N are model constants. A negative value of N makes Equation (14) a hyperbolic power function. Numerical simulations of a plate impact test configuration were performed to evaluate the effects of the δ function on the space signal. In these simulations, the initial slope of $\delta(\rho)$ at $\rho=1$ greatly influenced the slope of the spall signal. By taking advantage of this aspect, a parameter, β ($-\delta'(1)$) was introduced. With β , N , and ρ_{cr} as model constants, the corresponding value of κ can be solved by a simple iterative scheme. An idealistic value of one can be assumed for ρ_{cr} . Therefore, N and β become the only model parameters for void growth description.

As a first step in deriving the plastic strain rates, the yield condition for the aggregate can be rewritten as:

$$\Phi = (2+\rho^2) J_2 + \frac{1-\rho^2}{3} I_1^2 - \delta(\rho) Y_m^2 = 0 \quad (16)$$

The viscoplastic strain rates in the aggregate can be calculated using the flow rule derived as:

$$\dot{\epsilon}_{ij}^p = \dot{\lambda} \frac{\partial \Phi}{\partial \sigma_{ij}} \quad (17)$$

The proportionality factor, $\dot{\lambda}$, can be obtained using the flow rule in conjunction with the following relationship:

$$(1-f) Y_m \dot{D}_m^p = \sigma_{ij} \dot{\epsilon}_{ij}^p \quad (18)$$

where f is the void volume fraction and related to relative density ρ through $f = 1-\rho$. Note that 'm' is a subscript and not a tensorial index. The above expression was derived from the definition that the total plastic work in the aggregate is entirely due to the plastic work done by the matrix. By combining Equations (17) and (18), $\dot{\lambda}$ can be expressed by,

$$\dot{\lambda} = \frac{(1-f) Y_m \dot{D}_m^P}{\frac{\partial \Phi}{\partial \sigma_{ij}} \sigma_{ij}} \quad (19)$$

The plastic strain rates in the aggregate can be rewritten as:

$$\dot{\epsilon}_{ij}^P = \frac{(1-f) Y_m \dot{D}_m^P}{\frac{\partial \Phi}{\partial \sigma_{rl}} \sigma_{rl}} \frac{\partial \Phi}{\partial \sigma_{ij}} \quad (20)$$

In the constitutive model formulation, the total strain rate is decomposed into elastic and plastic strain rates. The elastic strain rates, $\dot{\epsilon}_{ij}^e$, are related to the stress through Hooke's law as:

$$\dot{\epsilon}_{ij}^e = D_{ik} \dot{\sigma}_{kj} \quad (21)$$

where D_{ik} is the inverse of elastic modulus matrix, E_{ik} .

Using the consistency condition which holds during the plastic flow, an expression can be obtained for \dot{Y}_m as:

$$\dot{Y}_m = \frac{-\left(\frac{\partial \Phi}{\partial \sigma_{ij}} \dot{\sigma}_{ij} + \frac{\partial \Phi}{\partial f} \dot{f}\right)}{\frac{\partial \Phi}{\partial Y_m}} \quad (22)$$

An expression for $\dot{\sigma}_{ij}$ can be obtained from Equation (21) by replacing the elastic strain rate as the difference between total and plastic strain rates.

$$\dot{\sigma}_{ij} = E_{il} (\dot{\epsilon}_{lj} - \dot{\epsilon}_{lj}^P) \quad (23)$$

3.5 Degradation of Shear and Bulk Moduli

The shear and bulk moduli are degraded using Mackenzie's [28] formula. Mackenzie derived an approximate analytical expression for the reduction of elastic stiffness based on the elastic-plastic flow around a spherical void in an infinite, incompressible matrix material. The RDG model [1] employed the corresponding expression for the degraded moduli \hat{K} and \hat{G} as,

$$\frac{\hat{K}}{K} = \frac{(1 - f)}{(1 + \frac{3Kf}{4G})}, \quad (24)$$

$$\frac{\hat{G}}{G} = (1 - f) \left(1 - \frac{(6K + 12G)f}{(9K + 8G)}\right), \quad (25)$$

where K and G are the bulk and shear moduli of the intact material. Since the void volume fraction is also changing with time, the stress rate equation (23) needs to be modified to add a term proportional to the void growth rate. Appendices A and B outline the solution scheme to solve the governing equations.

3.6 Equation of State for the Aggregate

The equation of state for the solid (intact) material has been routinely determined from the experimentally obtained Hugoniot data for several metals, such as steel, aluminum, copper, etc. However, once the initially intact solid develops voids upon tensile loading, the equation of state (EOS) of the original solid material is no longer valid during the subsequent compressive loading. For this purpose, the EOS parameters have to be modified.

The simple approach used in the RDG model is an extension of Mackenzie's procedure. The EOS for the intact solid is described by the Mie-Gruneisen equation as

$$P_s = (\beta_1 \mu + \beta_2 \mu^2 + \beta_3 \mu^3)(1 - \Gamma \mu/2) + \Gamma(I - I_0), \quad (26)$$

where β_1 , β_2 , β_3 , and Γ are EOS constants. μ is the volumetric compressible strain of the intact solid, $(V_s/V - 1)$, and I is the specific internal energy of the solid material. To account for the voids, the Mackenzie's formulation is implemented as follows. A volumetric elastic strain of the aggregate is first defined as,

$$\mu_{ag} = \left[(1 + \mu)/(1 - f) - 1 \right], \quad (27)$$

to replace μ in the right side of Equation (26). Then the right side expression of Equation (26) is multiplied by the Mackenzie correction term, \hat{K}/K , to

obtain the aggregate pressure, P . Thus a voided material undergoing compression will load along a degraded bulk modulus at the aggregate compressible strain. At high enough stress levels, the void will collapse ($f=0$), and thus the modified EOS will reduce to Equation (26).

The various governing equations can be rearranged and numerically integrated. The RDG model along with BP or JC model was implemented into the EPIC2 finite element code [29]. Special purpose subroutines have been developed successfully. The corresponding numerical scheme is given in Appendix A.

4. FAILURE ANALYSES USING THE RDG MODEL

The strength model (BP or JC) constants are determined using the stress - strain data from split Hopkinson bar (SHB) tests. These data may comprise data from quasi-static tensile, SHB tensile, compressive, and torsional tests. Rajendran et al. [24] described a combined experimental and numerical scheme for evaluating BP model constants. They also included the HEL (Hugoniot Elastic Limit) data in the scheme. Johnson and Holmquist [30] provided a methodology to obtain JC model constants. The BP and JC model constants for various metals are given in Tables 1 and 2.

The determination of the failure model constants requires plate impact test data in terms of either velocity history or stress history at the back of the target. Rajendran and Bless [11,31] reported the test and diagnostic techniques as well as data for several metals. Rajendran et al. [32] determined the failure model constants using the velocity history obtained from a plate impact test on OFHC copper.

Numerical exercises were conducted using the new subroutines. The exercises were based on a plate impact test simulation.

4.1 Plate Impact Simulations

Detailed discussions on planar plate impact test technique can be found in References 33 and 34. Determination of the failure model parameters is aided through the simulation of plate impact tests. Simulations are carried out using the STEALTH one-dimensional finite difference code [35]. The effect of each model parameter on the spall behavior is evaluated from the simulation results. A methodology to determine the parameters is outlined. The model also has been successfully used to describe spallation in OFHC copper.

4.1.1 Physical Features

Impact of a 2 mm thick copper flyer against a 9 mm thick OFHC copper target is modeled using the STEALTH code. The constitutive and failure models described in Section 3 were used to characterize the high strain rate behavior of copper. Our first objective was to demonstrate the experimentally observed important physical features of the free surface velocity profile. In Figure 1, results from two different simulations are shown. In the first simulation

important physical features of the free surface velocity profile. In Figure 1, results from two different simulations are shown. In the first simulation the model parameters were chosen so that the target spalls. A typical spall signal, as is usually observed in an experiment, can be seen in Figure 1. In the second simulation the spall is suppressed by choosing a zero value for the nucleation parameter, f_1 . The complete unloading of the velocity history, as indicated by the dotted line, clearly demonstrates the absence of spall in the target.

In Figure 2, the velocity histories obtained from simulations at different impact velocities are shown. The most important physical features in the velocity profiles are the velocity level, ΔV_s , and the time duration or period, τ_s , of the wave transit between the spall plane and the free surface. The ΔV_s corresponds to a stress level around which rapid microvoid or microcrack nucleation occurs (note that $\sigma_N = 1/2 \rho C \Delta V_s$). If the impact velocity is greater than ΔV_s , as in the cases of plots A, B, C, and D in Figure 2, then spallation will occur, as indicated by the spall signal. However, at an impact velocity of 50 m/s, spall nucleation has not occurred. The tensile stresses in the target at this impact velocity are lower than the mean nucleation threshold stress σ_N (≈ 16 kbars). In the nucleation model, nucleation is assumed to occur at $\sigma_N \pm 3s$, where s is the standard deviation. Figure 3 shows that at velocity $V = 100$ m/s, the tensile peak stress was around 13 kbars, compared to a peak stress of 18 kbars in compression. This is due to void softening of material which reduced the stress levels.

The void volume fraction distribution levels in the target at three different times are shown in Figure 4. The distribution clearly shows that the maximum void volume fraction is at the spall plane which is around 2 mm (flyer plate thickness) from the free surface (at $x = 7$ mm). Presence of voids at and around the spall plane has been supported by metallographical studies conducted on different materials [14-16].

In Figure 5, the loading path at the spall plane of the target is shown. The void volume levels are shown by dotted lines. Initially, the strength is independent of pressure as can be seen between points A-B. Damage nucleation has not yet initiated, and therefore f remains zero. At B, the nucleation occurs. As the tensile pressure increases, the void volume also increases between the loading points B-C. Strength rapidly decreases between

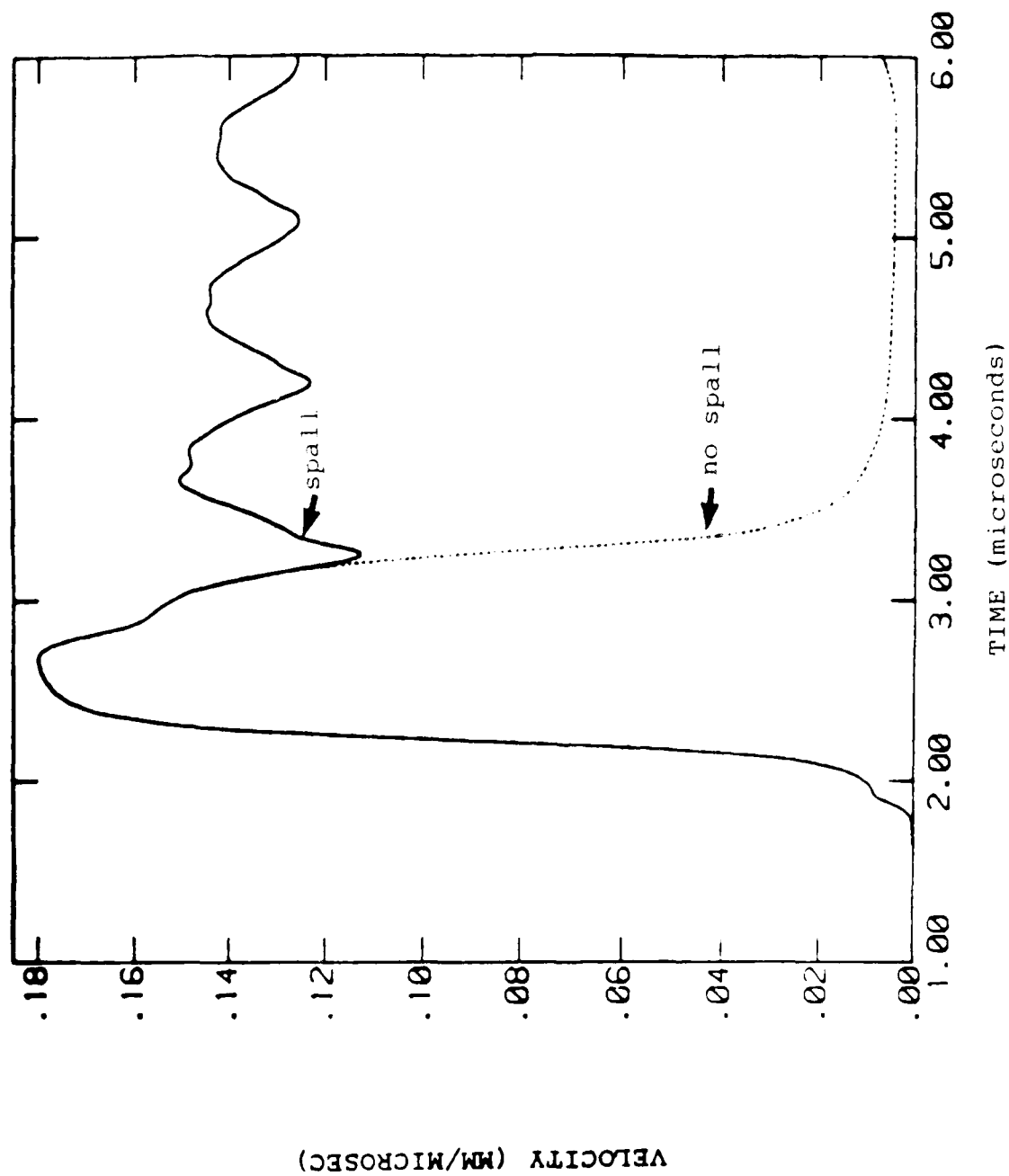


Figure 1. Simulated Velocity History for a Target without and with Spall Failure

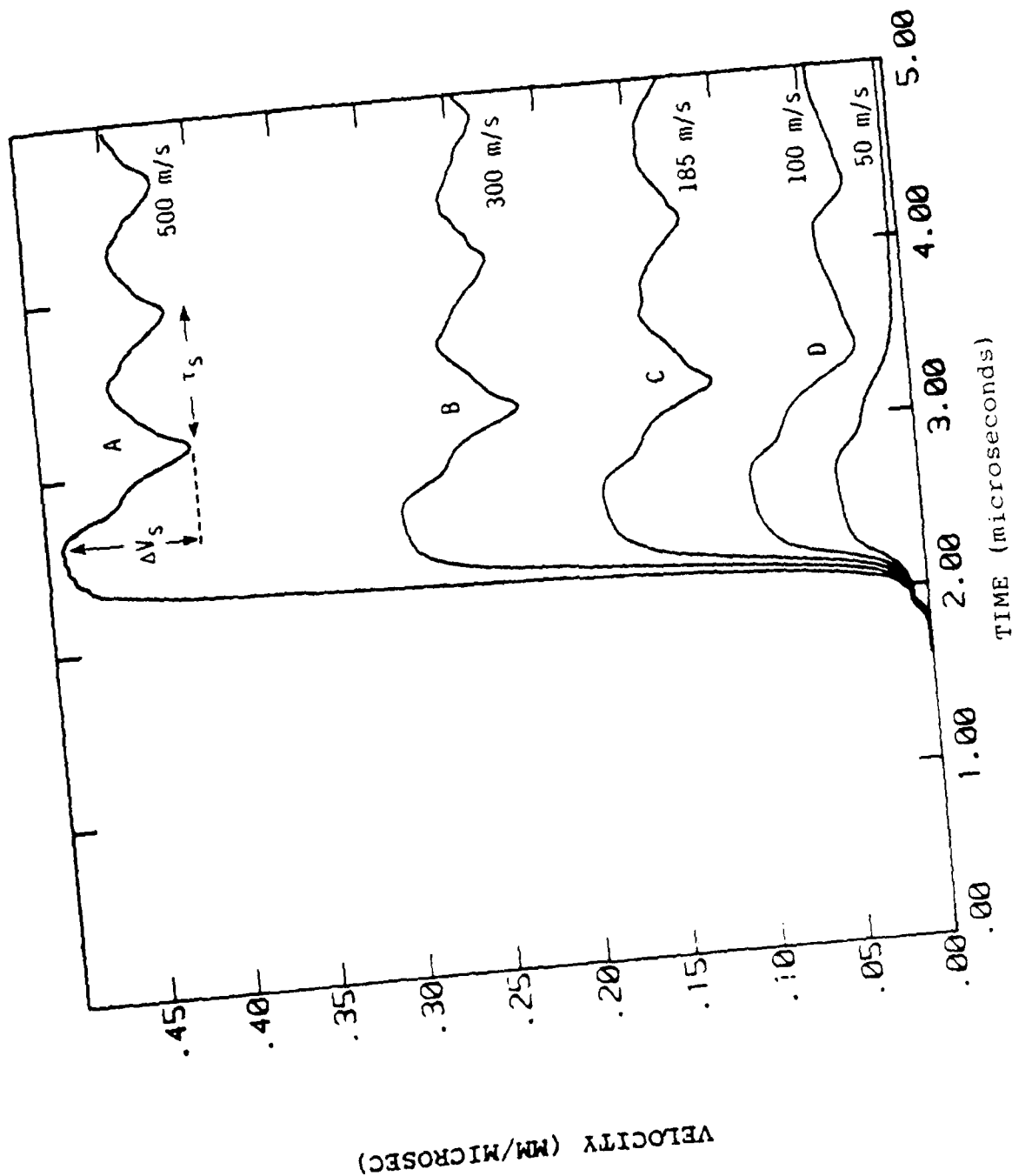


Figure 2. Simulated Free Surface Velocity Histories at Different Velocities.
(Note: as velocity decreases, no spall occurred.)

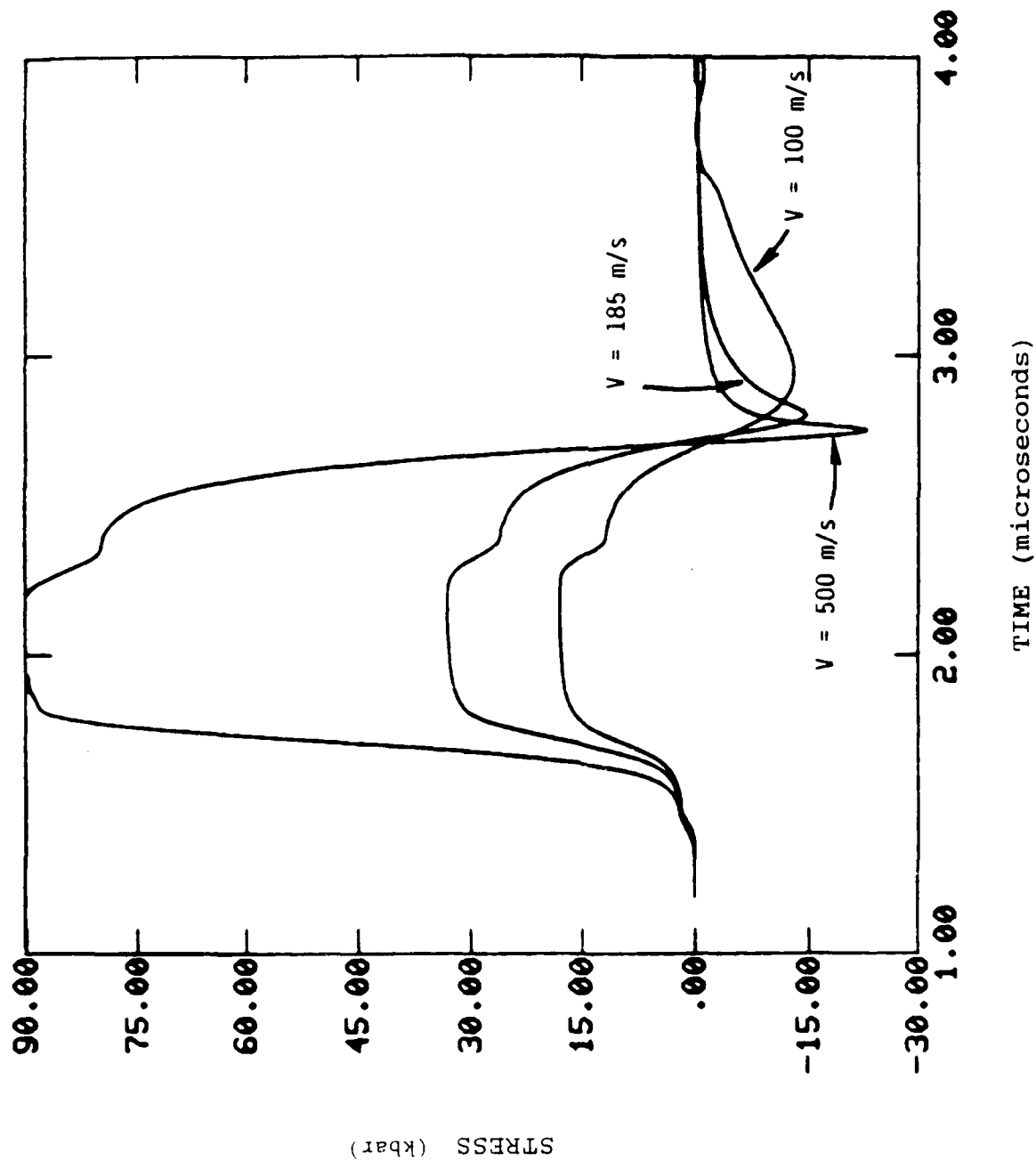


Figure 3. Simulated Stress History at the Spall Plane. Stress Relaxation under Tension is Shown for Three Impact Velocities - 100, 185, and 500 m/s. (Note: stress is -Ve in tension and +Ve in compression.)

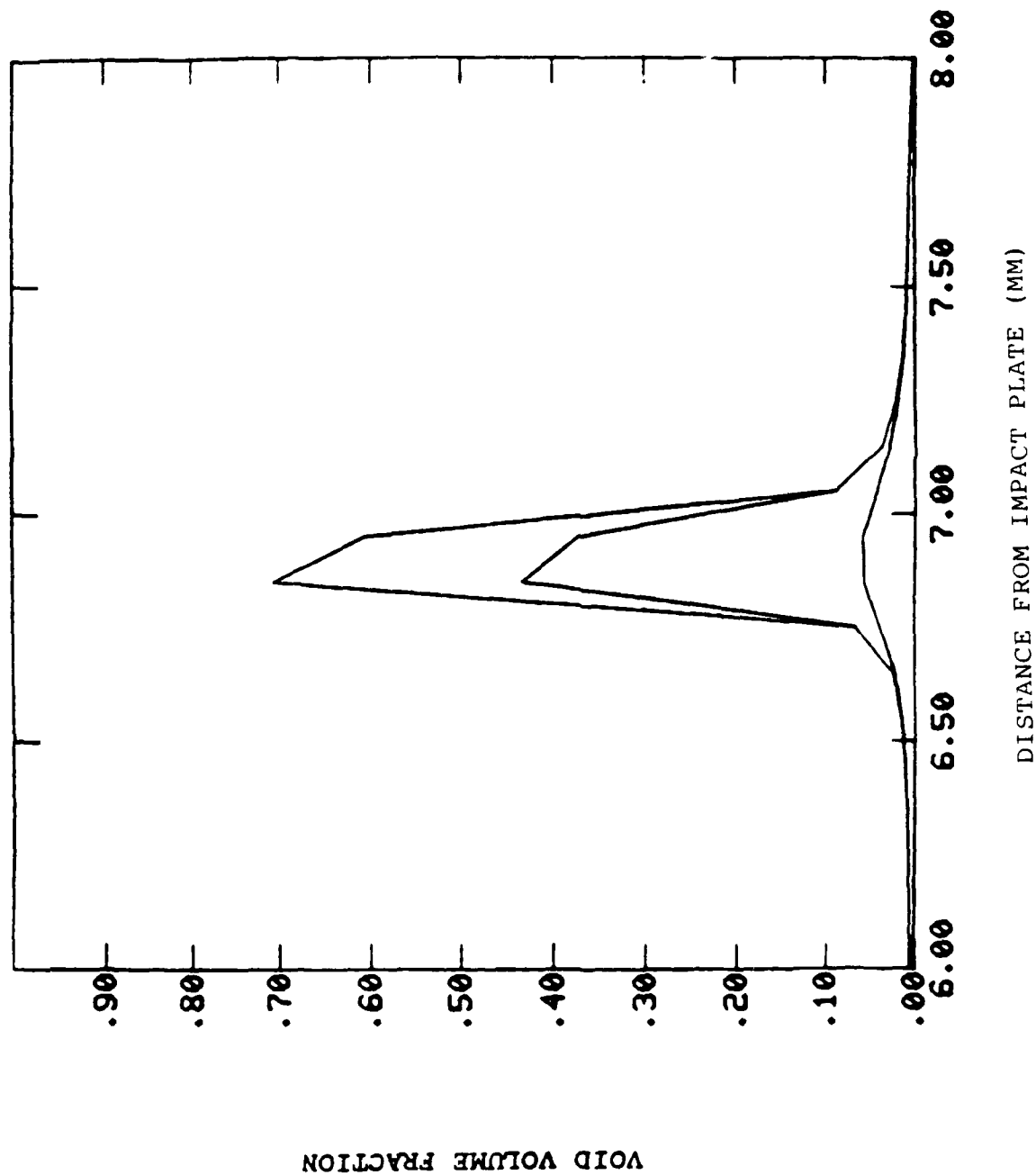


Figure 4. Model Simulated Void Distribution in the Impacted Target Plate for $t = 3, 4, \text{ and } 6 \text{ Microseconds.}$

points C-D. At one percent void (around D), the void contained aggregate can no longer sustain tensile pressure, so the pressure rapidly decreases as the void volume reaches 10 percent. Failure (coalescence of voids) occurs between points E-F. Both pressure and strength approach zero as the material completely fails.

4.1.2 Stability of the Solution

The integration of the ordinary differential equations for the constitutive model by a Diagonally Implicit Runge-Kutta (DIRK) scheme is known to be stable and at least second order accurate. But if the time intervals of the DIRK scheme are much smaller than the time step determined by the Courant criterion in the STEALTH wave propagation code [35], then the stability and accuracy of the solution becomes uncertain. Depending on the DIRK time step size, the STEALTH stable time step for a particular zone (or element), as determined from the Courant condition, may be reduced by an integer factor ranging from 2 to 10. This factor is initialized to one, indicating no reduction in the stable time step. Then the factor is either increased by one, if the last DIRK time step is less than one tenth of the STEALTH time step, or decreased by one, if the last DIRK time step is greater than two tenths of the STEALTH time step. This method allows a gradual, but not necessarily permanent, reduction in the STEALTH stable time step down to one tenth of the stable time step computed from the Courant condition. Since there is no mathematical criterion of stability for the entire solution, a few numerical exercises were devised to check for solution stability and accuracy. These exercises involved several plate impact simulations. One effective numerical test was to determine if the total momentum and the total energy remained constant during a plate impact simulation. The solution was accepted only if this condition was met. The second exercise was to determine if the entire solution remained essentially the same if the grid size was varied. The results are shown in Figure 6 for two impact velocities (200 m/s and 500 m/s) with three different grid sizes. It is possible to ensure stability and accuracy by forcing the STEALTH time interval to be the same as the DIRK scheme time interval, but this is costly in terms of programming effort and excessive computer time. In any case, numerical exercises to vary the numerical integration and stability parameters should be conducted to optimize the

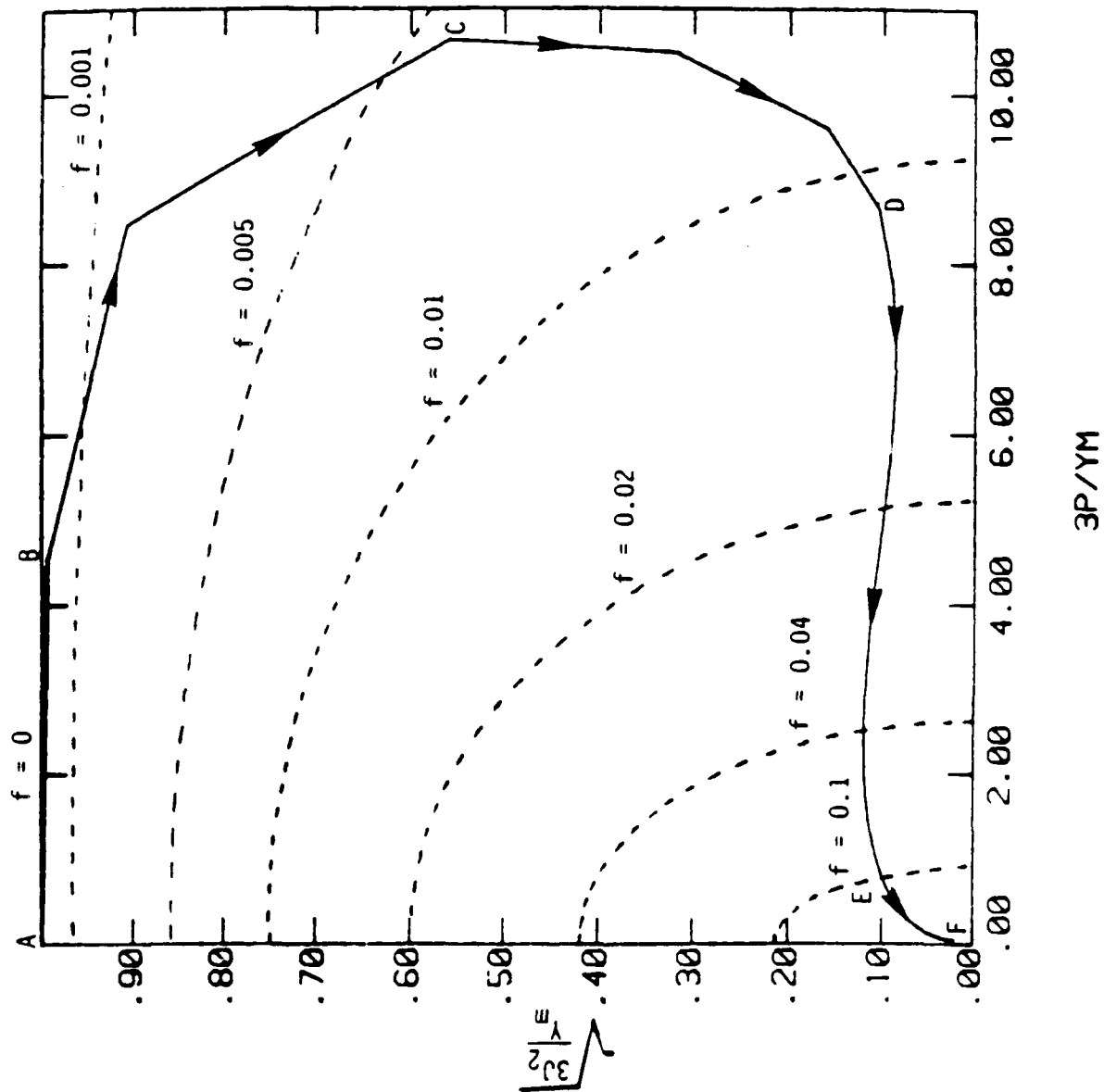


Figure 5. The Loading Path ($\sqrt{3J_2}/Y_m$ vs. $3P/Y_m$) at the Spall Plane in a Simulation.

stability, accuracy, and computer time of the solution. The results so far indicate that the solution is stable and reasonably accurate.

4.1.3 Sensitivity Study

It is important to evaluate the effects of various model parameters (σ_N , f_1 , s , β , N , f_{cr}) on the numerically simulated failure process. For this purpose, a sensitivity study was considered. The sensitivity of the dynamic failure model parameters on the solution (in the free surface velocity versus time plot) can be checked by varying the values systematically. The variation in the values of the three void nucleation parameters, (σ_N , f_1 and s) were examined first, and then the three void growth parameters (β , N , and f_{cr}) were examined.

An increase in the value of σ_N caused the spall signal to occur later while the solutions during the rebound tend to merge together. Likewise, a decrease in the value of f_1 caused the spall signal to occur later while the solutions during the rebound tend to merge together. It appears the void nucleation parameters σ_N and f_1 have a strong influence on the initial spall signal, but become a negligible influence on the void growth which affects the rebound. The standard deviation s can be defined as a fraction of σ_N . The sensitivity study used three different fractions, 0.125, 0.25, and 0.5. Recall from Equations (7) and (8) that the model for void nucleation due to stress follows a Gaussian distribution with mean σ_N , which allows nucleation to occur for a stress range of $\sigma_N \pm 3s$. Since void nucleation in metals can only occur during tension, a practical upper limit for the fraction is one third. This prevents a negative lower bound for the nucleation stress range. Varying the stress standard deviation, s , had only a minor effect on the spall signal or the rebound.

The rebound peak of the spall signal increased for increasing values of the void growth parameters β and $|N|$. The initial slope of the spall signal was less influenced by N than β . Further sensitivity studies showed that the void growth parameter β seems to affect the slope significantly. Taking advantage of the negligible influence of N on the slope, the parameter β can be estimated by matching the spall signal slopes between the simulation and experiment. Varying f_{cr} from 0.6 to 1.0 had a very minimal impact on the spall

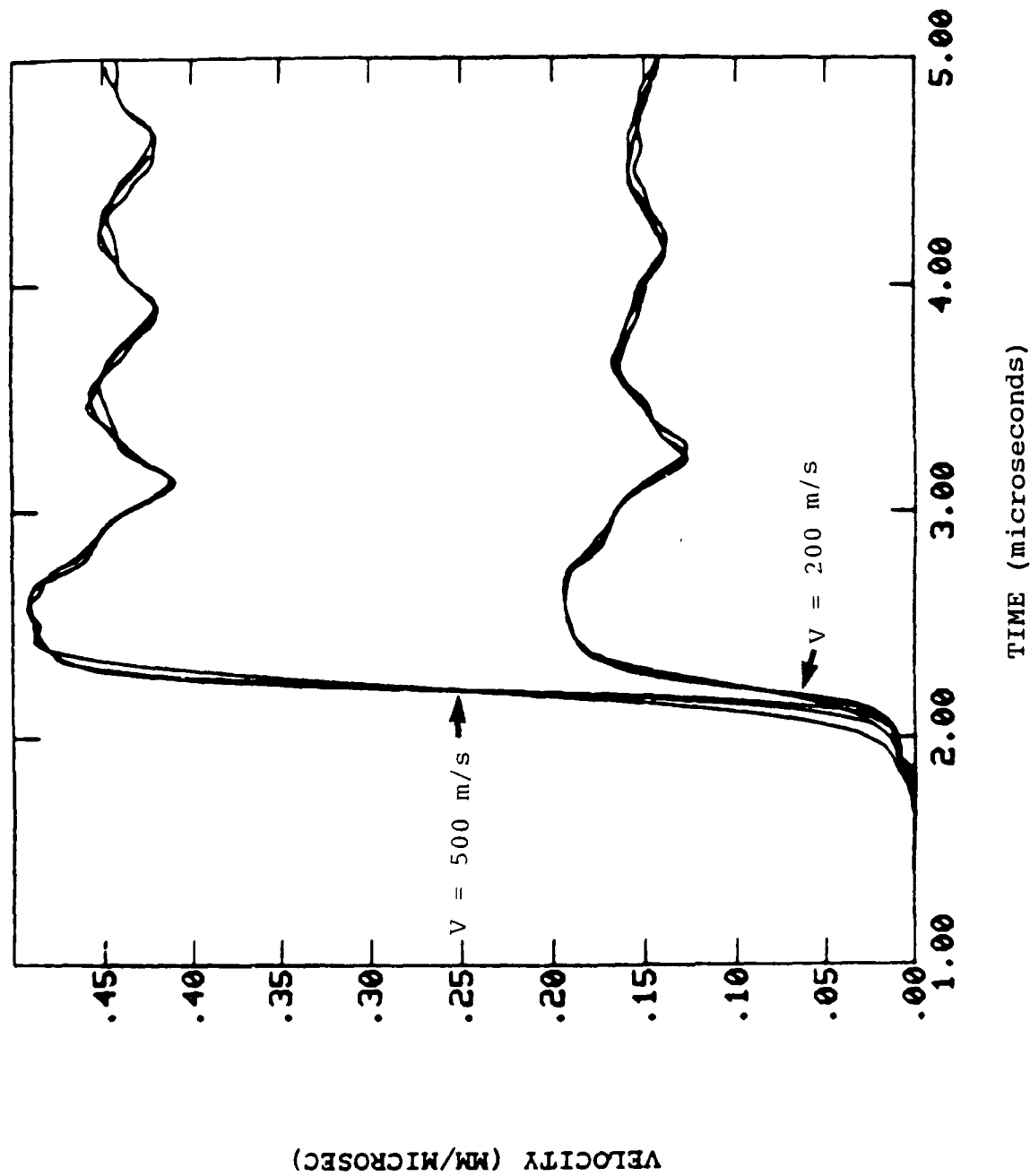


Figure 6. Demonstration of Grid (or mesh) Independency of the Solution for Three Different Grids at Two Velocities.

In summary, the sensitivity study indicates that the failure model parameters can be systematically determined by matching the simulation results with the spall signal. Preliminary estimate for σ_N can be obtained from the relationship, $\sigma_N = 1/2 \rho C \Delta V_s$, where ρ is the mass density and C is the wave speed. The value for ΔV_s is available from the velocity history. The value for s can be arbitrarily chosen to be one-fourth of σ_N . A theoretical value of 1 can be assigned for f_{cr} . The only remaining parameters that need to be determined from the spall signal are f_1 , β , and N . f_1 can be determined by matching the spall arrival time; β is chosen based on matching the slope of the spall signal; finally, N is selected based on matching the rebound peak of the spall signal. Rajendran et al. [32] employed this scheme and determined the model parameters for OFHC copper. The following section describes this effort.

4.2 Model Parameters

For establishing a standard procedure to calibrate the failure model constants, two plate impact experiments (#538 and #1299) were considered. The first experiment was on an OFHC copper target plate and the velocity history was obtained using VISAR (velocity interferometry). The second experiment considered an HY100 steel target, and in this experiment the diagnostic was the manganin gage measured stress history. The test configuration details are given in Table 3. These two experiments were simulated using the EPIC code. The special purpose subroutines describing the RDG model were used to model the spall process in both OFHC copper and HY100 steel. Using the suggested procedure, the model constants for these two as well as several other metals were determined. The corresponding constants are given in Table 4.

The BP model was employed for the intact material description. The corresponding parameters were given earlier in Table 1. The plate impact experiment on annealed OFHC copper reported by Rajendran et al. [32] was employed in the failure model parameter evaluation. A 2 mm copper flyer was impacted against a 9 mm copper target at an impact velocity of 185 m/s. The free surface velocity history of the target was determined by VISAR measurements. This velocity history was used in the model parameter calibrations.

Based on the sensitivity study discussed in the preceding section, the failure model parameters are estimated. Out of the six parameters (σ_N , s ,

TABLE 3
PLATE IMPACT EXPERIMENTS

Shot Number	Flyer Plate		Target Plate		Impact Velocity (m/sec)
	Material	Thickness (mm)	Material	Thickness (mm)	
7-1299	Copper	3	HY100 Steel	6	489
7-1300	Copper	3	C1008 Steel	6	462
7-1298	Copper	3	Armco Iron	6	470
7-1268	1020 Steel	3.9	1020 Steel	7.8	572
7-1288	Copper	2	Copper	4.1	512
7-1302	Copper	2	Tantalum	6	735
7-1455	MAR-200 Steel	3	MAR-200 Steel	6	508
7-1454	MAR-250 Steel	3	MAR-250 Steel	6	575
7-1523	AF1410 Steel	4.5	AF1410 Steel	9.0	678

TABLE 4
RDG MODEL CONSTANTS

Material	Nucleation			Yield Function	
	f_1	σ_N	$s=(\sigma_N/4)$	β	N
OFHC Copper	0.01	1.6	0.4	65	-2.4
HY100 Steel	0.035	3.6	0.9	30	-1.0
C1008 Steel	0.02	1.2	0.3	100	-2.0
MAR 200-Steel	0.01	4.8	1.2	40	-5.0
Armco Iron	0.05	2.0	0.5	70	-0.5
Tantalum	0.003	4.8	1.2	10	-3.0
1020 Steel	0.01	2.4	0.6	1	-0.5
MAR-250 Steel	0.01	3.2	0.8	50	-3.0
AF1410 Steel	0.01	5.6	1.4	20	-4.0

Based on the sensitivity study discussed in the preceding section, the failure model parameters are estimated. Out of the six parameters (σ_N , s , f_{cr} , f_1 , β , and N), determination of the first three is fairly straightforward. The calculated value for σ_N was 16 kbar, as determined from the measured value of ΔV_s . In order to minimize the number of model parameters, by taking advantage of the fact that s and f_{cr} are less sensitive to the failure processes, arbitrary values were assigned for $s = 0.25 \sigma_N$ and $f_{cr} = 1$. Also, the spall signal did not show significant differences for $s = 2, 4$, and 8 . Similarly, for $f_{cr} \geq 0.5$, the results showed similar trends; therefore, a theoretical value of 1 was chosen for f_{cr} .

The remaining parameters β , N , and f_1 were determined by adjusting them until the simulated free surface velocity matched well with the experimental data. Following the guidelines discussed in the preceding section, f_1 was adjusted to approximately match the spall signal arrival time. Then β was modified until the average initial slope of the spall signal matched the experimental data. Finally, the value of N was chosen so that the peak velocity of the spall signal rebound matched with the data. The corresponding failure model parameters for OFHC copper are given below.

σ_N (kbar)	s (kbar)	f_1	β	N	f_{cr}
16	4	0.01	65	-2.4	1

The comparison between the model simulation and the experimental velocity history data for OFHC copper is shown in Figure 7. Since the HEL of OFHC copper is extremely low compared to the shock stress, the BP model predicted HEL (knee at A in Fig. 7) did not match well. However, for copper, the HEL value is not considered critical because plastic yielding occurs at (uniaxial) stress below 1 kbar. Fine tuning of the BP model parameters will certainly improve the matching, but this will not significantly influence the failure model constants. The rounding of the simulated velocity profile around P and R in Figure 7 indicates either the value of artificial viscosity coefficient is excessive or the strain rate sensitivity ($n=0.4$) assumed for copper in the BP model is large. The matching beyond the point S is controlled by the RDG model constants. In general, the overall match between the simulation and the data seems to be very good. This demonstrates the ability

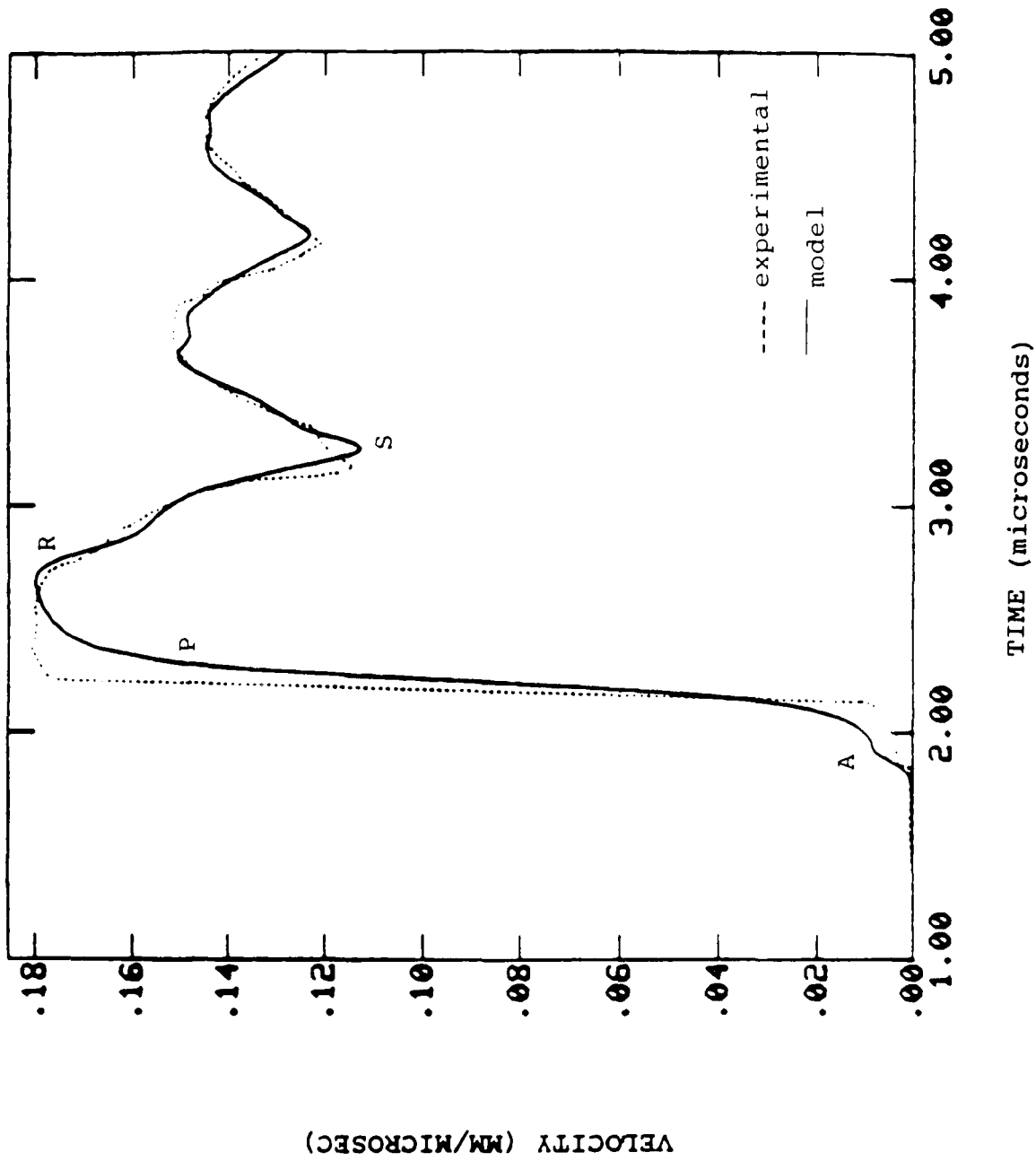


Figure 7. Comparison Between Model Simulation and the Experimental Data of the Free Surface Velocity History.

to calibrate the model constants using plate impact test data as well as the RDG model capability to accurately reproduce the spall signal.

To further verify the model constant calibration using a plate impact test data, spall in HY100 steel was considered. In this case, a manganin gage recorded stress history is the experimental data. Recall that the failure model constants for OFHC copper were obtained using the velocity history. The experimental data were obtained only for a time duration of 4 microseconds. In this experiment the release waves from the edges of the flyer plate arrived at the gage location around 4.2 microseconds. The model constants were obtained by matching the experimental stress signal until this time. The corresponding match is shown in Figure 8a. The modeling of the material behavior before any void nucleated in the target is excellent. This indicates that the BP model constants reproduced the HEL data well. Also, the strain rate sensitivity of HY100 steel seemed to be modeled correctly as one can interpret from the shape of the simulated signal around the stress peak. Rajendran et al. [24] modeled the SHB test accurately using the same BP model constants for HY100 steel. The ability to model both the SHB and plate impact tests makes the model constants relatively more general than by matching only one of these two test configurations. In Figure 8b, the computed stress history at the spall plane is shown. The compressive stress is shown as positive, and the tensile stress is shown as negative. The material experiences a compressive stress of around 10 GPa. When the material goes into tension, the stress peak only reaches 2.8 GPa. This reduction in stress under tension is due to void softening. The stress relaxes to zero as the material spalls. Modeling of this time dependent stress relaxation is the most important feature of the RDG model.

The failure model constants were accurately determined as can be seen from the excellent comparison between the model simulation and the experimental data in Figure 8. Since the BP model constants for the intact material and the RDG model constants for the void-containing aggregate have been accurately determined, the entire stress history could be reproduced accurately. Of course, this statement assumes that the equations of state for the flyer, target, and the PMMA are accurately modeled in the computer code simulation. The ability of the model to reproduce the entire spall signal clearly

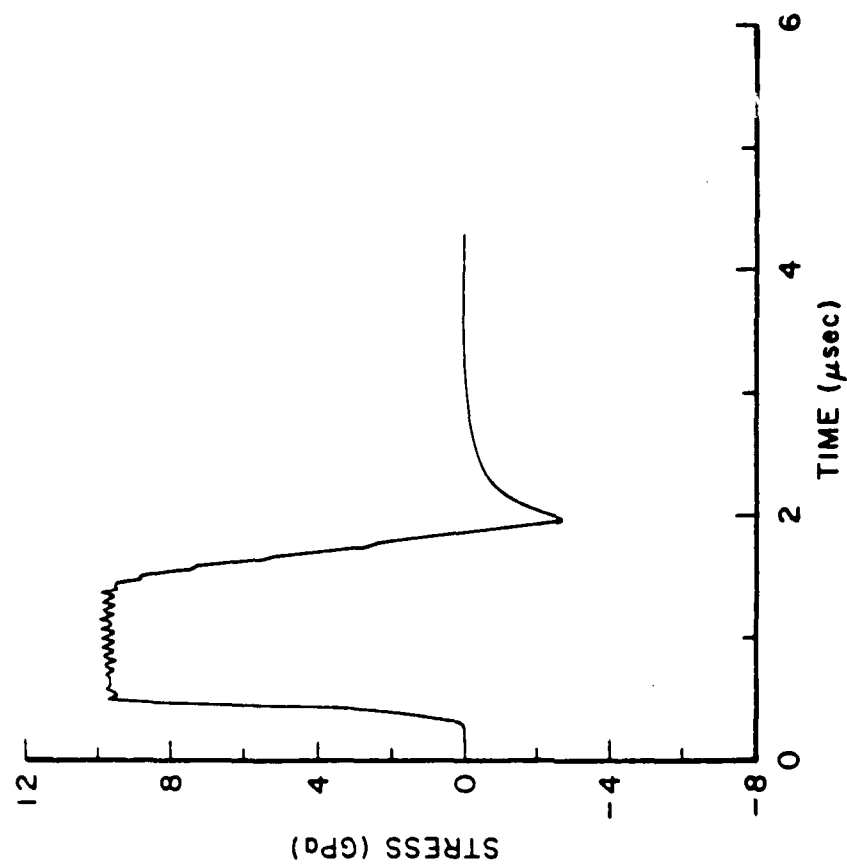
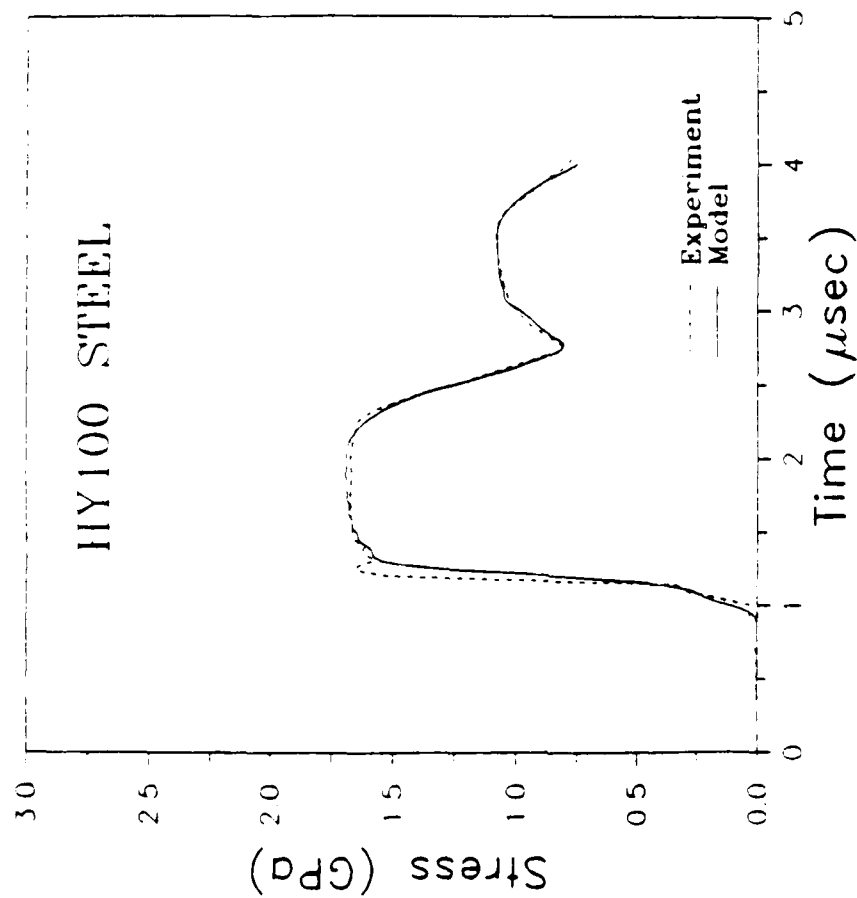


Figure 8. (a) Comparison between model and the measured stress history (HY100 steel). (b) Numerical simulation of the stress history at the spall plane (HY100 steel).

demonstrates that the nucleation and growth models follow the physical processes realistically.

RDG model constants were also determined for 1020, C1008, and MAR-200 steels, Armco Iron, and pure tantalum by matching the experimental data as shown in Figures 9 and 10. The ability of the RDG model in modeling the spall failure is truly outstanding. The RDG model generated spall signal for tantalum matched extremely well with the data up to 3.4 microseconds. The difference between the model and experiment could be due to the uncertainty in the experimental data. In this case (#7-1302), the plate impact configuration was such that the spall plane location was very close to the manganin gauge (about one millimeter).

In the simulations, behavior of the intact material can also be described by the JC model instead of the BP model. Using the JC and RDG models, the plate impact test #1299 on HY100 steel was simulated. The JC constants for the HY100 steel were obtained by Johnson and Holmquist [34] using torsional SHB test data. In the simulation, the authors initially used the RDG model constants for HY100 that were determined in conjunction with the BP model. In Figure 11 the stress histories obtained from 1) test data, 2) simulation using BP model and the RDG model, and 3) simulation using JC model and the RDG model are shown. The matching between 1 and 2 are excellent which is not too surprising because the RDG model constants were calibrated in conjunction with the BP model. When the same RDG model constants were employed in the simulation in conjunction with the JC model, the spall signals did not match exactly. This slight difference could be attributed to the material characterizations of HY100 steel using different experimental configurations and sources. In other words, the descriptions of HY100 steel by the BP model and the JC model are slightly different; therefore, this difference will introduce slight alterations in the RDG model constants. To determine the RDG model constants that correspond to the use of JC model for the intact material, plate impact simulations were made and the constants were determined. A slight adjustment to the f_1 to a value of 0.01 led to a better fit between the failure model and the test data. It can be seen from Figure 12 that the spall signal is matched extremely well by both BP and JC models with the use of appropriate RDG model constants.

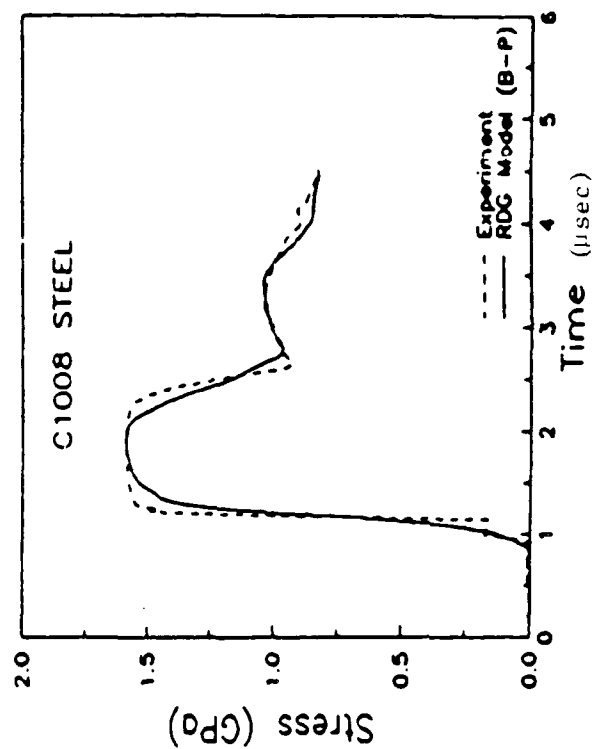
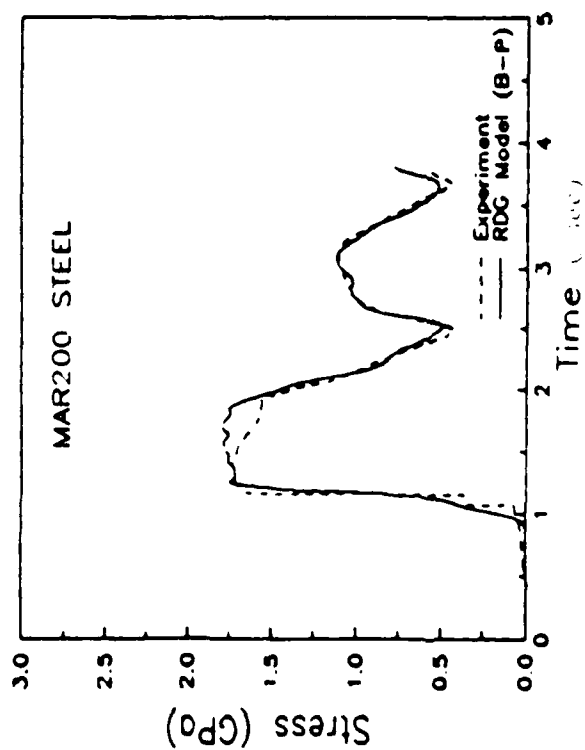
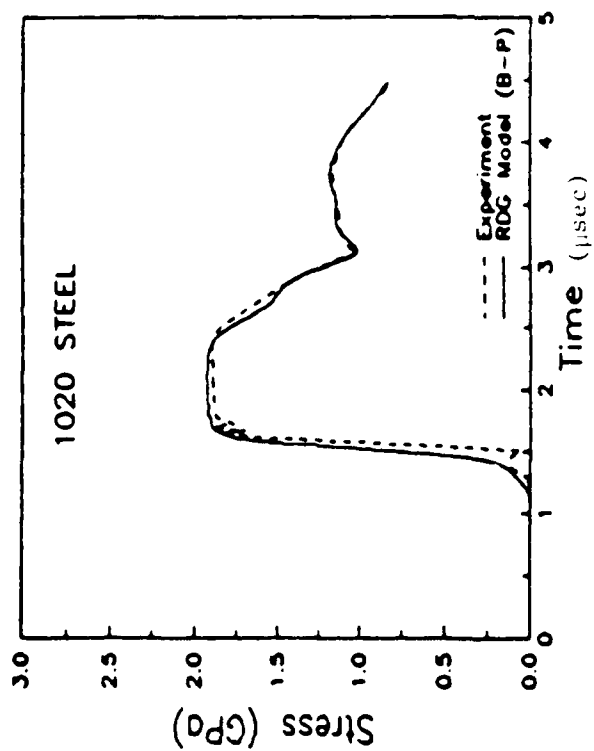


Figure 9. Comparisons between RDG model generated and experimental stress gauge for different metals.

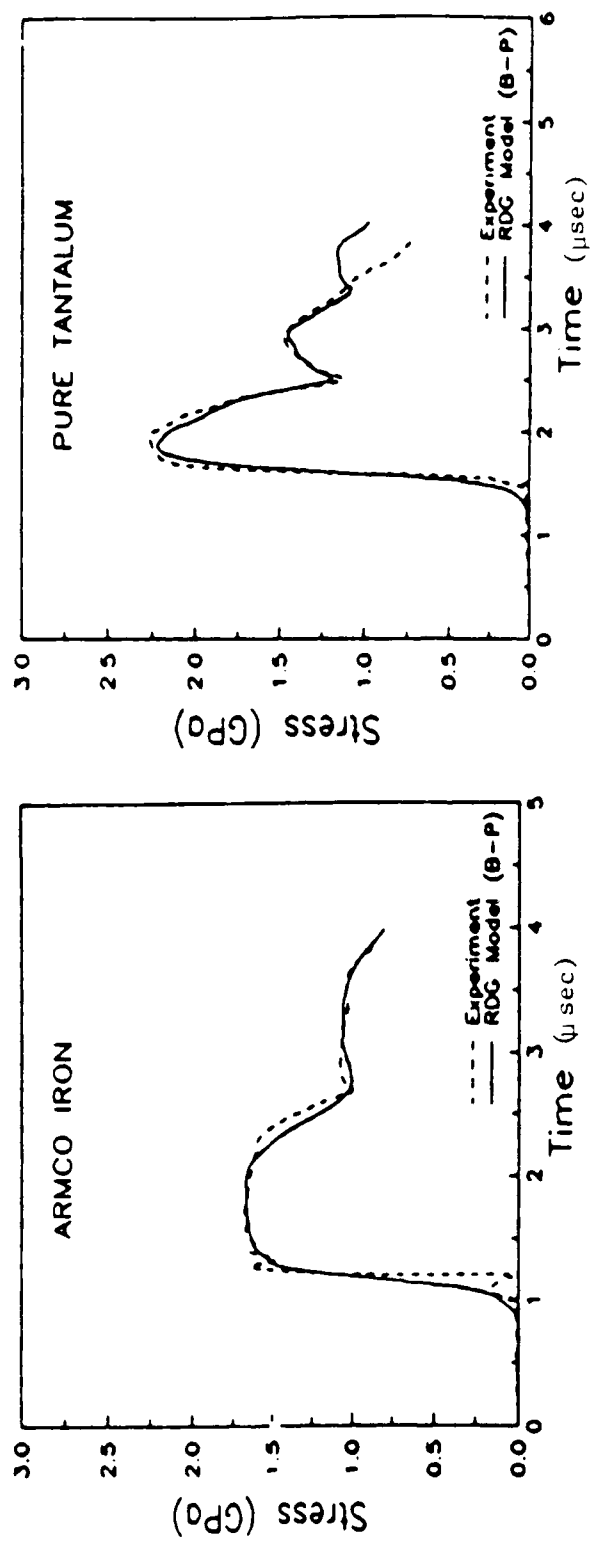


Figure 10. Comparisons between RDC model generated and experimental stress gauge signals for different metals.

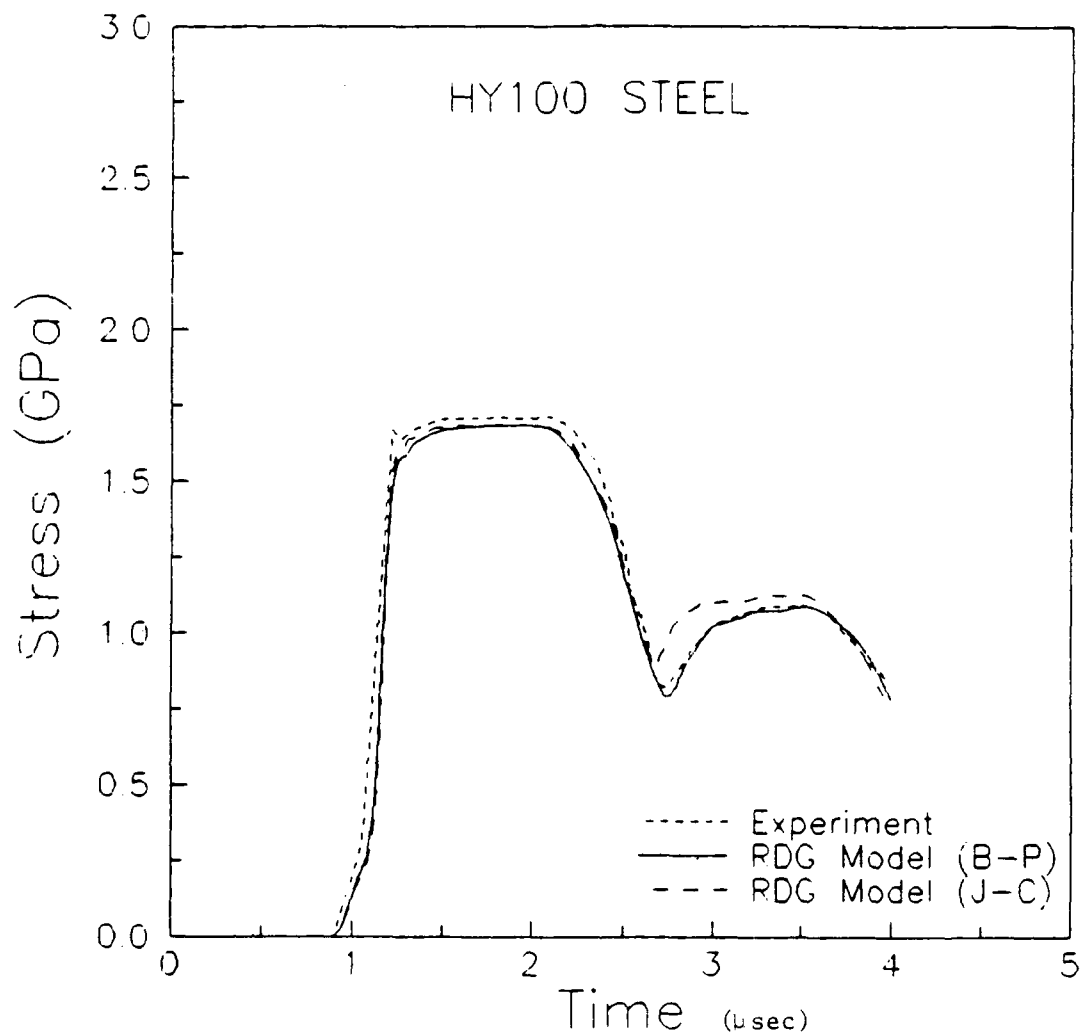


Figure 11. Comparisons of spall modeling for HY100 steel using BP and JC models. Spall process is described by the RDG model.

An important aspect of the modeling is the model's ability to reproduce an experiment which was not used for determining the model constants. Also the model's ability to reproduce a failure process in some other stress-strain configuration is important. To check this aspect, a new experiment (#1288) on OFHC copper was considered. In this experiment, the stress history at the interface of the target and the back plate was measured using a manganin gage. The flyer and target thicknesses and the impact velocity were all different than in experiment #538. The new experiment #1288 was simulated using the same model constants that were determined using experiment #538 to check the model's ability to predict the measured stress history. In Figure 13, a comparison between the model prediction and the data is shown. The model reproduced the measured spall signal extremely well as can be seen from this figure.

5. MODELING OF VOID COLLAPSE UNDER MULTIPLE SHOCKING

In real life application problems, such as projectile penetration into a target, explosively compacted metal operations, etc., the loading conditions often lead to multiple shocking in the material. Under these conditions, void growth as well as void collapse occur. The dynamic properties of the shocked material are modified due to loading history effects. To further evaluate the RDG model, a double flyer plate impact experiment was simulated with the EPIC-2 finite element code [29]. Previously calibrated RDG model parameters were used in the simulation. The computed stress history was compared with the experimentally measured stress history. A simple void collapse criterion, based on a critical void volume fraction, was employed to obtain a better fit to the experimental data.

5.1 Double Flyer Plate Impact Experiment

Yaziv [36] and Yaziv et al. [37] introduced a double flyer plate impact technique for examining the dynamic properties of shock damaged materials. This technique differs from a conventional plate impact experiment in that two flyer plates are used, separated by a small gap, as shown schematically in Figure 14.

The first flyer has a lower shock impedance than the second flyer. When the first flyer impacts the target plate, microvoid nucleation and growth occur in a localized area of maximum tensile stress in the target. The reshocking by the second flyer reverses the damage by closing the microvoids.

Grove et al. [38] simulated an experiment (#829) in which the first flyer was a 2 mm thick aluminum plate and the second flyer was a 3 mm thick copper plate. The spacing between the flyers was 0.25 mm, and the impact velocity was approximately 336 m/s. The target was a 4 mm thick OFHC copper plate with a PMMA backing. The stress history at the interface of the target and PMMA was measured with a manganin stress gauge.

The double flyer plate impact experiment was simulated using the EPIC-2 finite element code [29]. EPIC-2 material models were used to describe both flyers and the PMMA. The PMMA was modeled as a rate independent elastic-perfectly plastic material with a yield stress of 0.18 GPa. The RDG model was used to describe the plastic flow and dilatation in the OFHC copper target

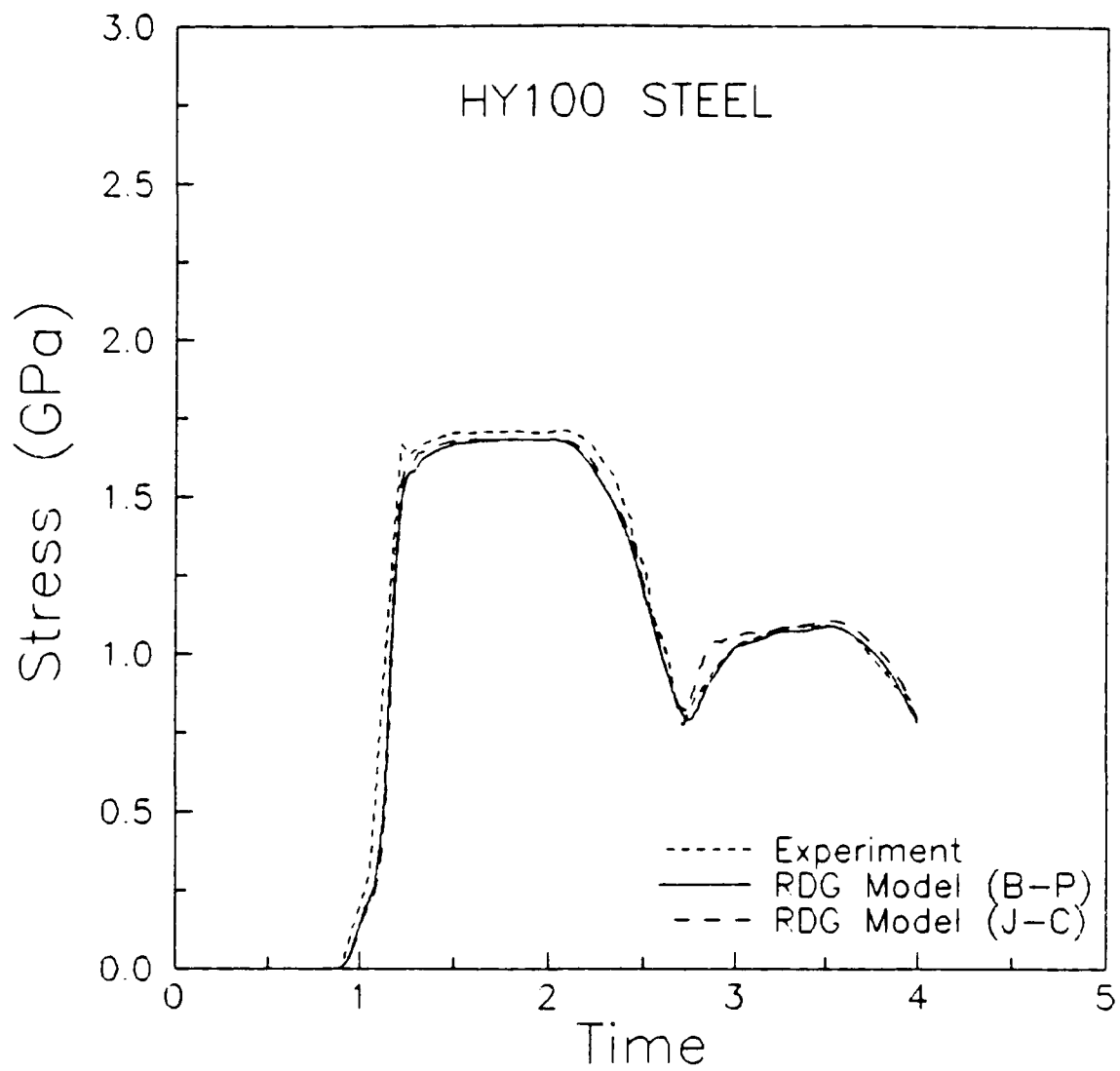


Figure 12. Comparisons between the spall signals generated using JC and BP models for different values of RDG model constants.

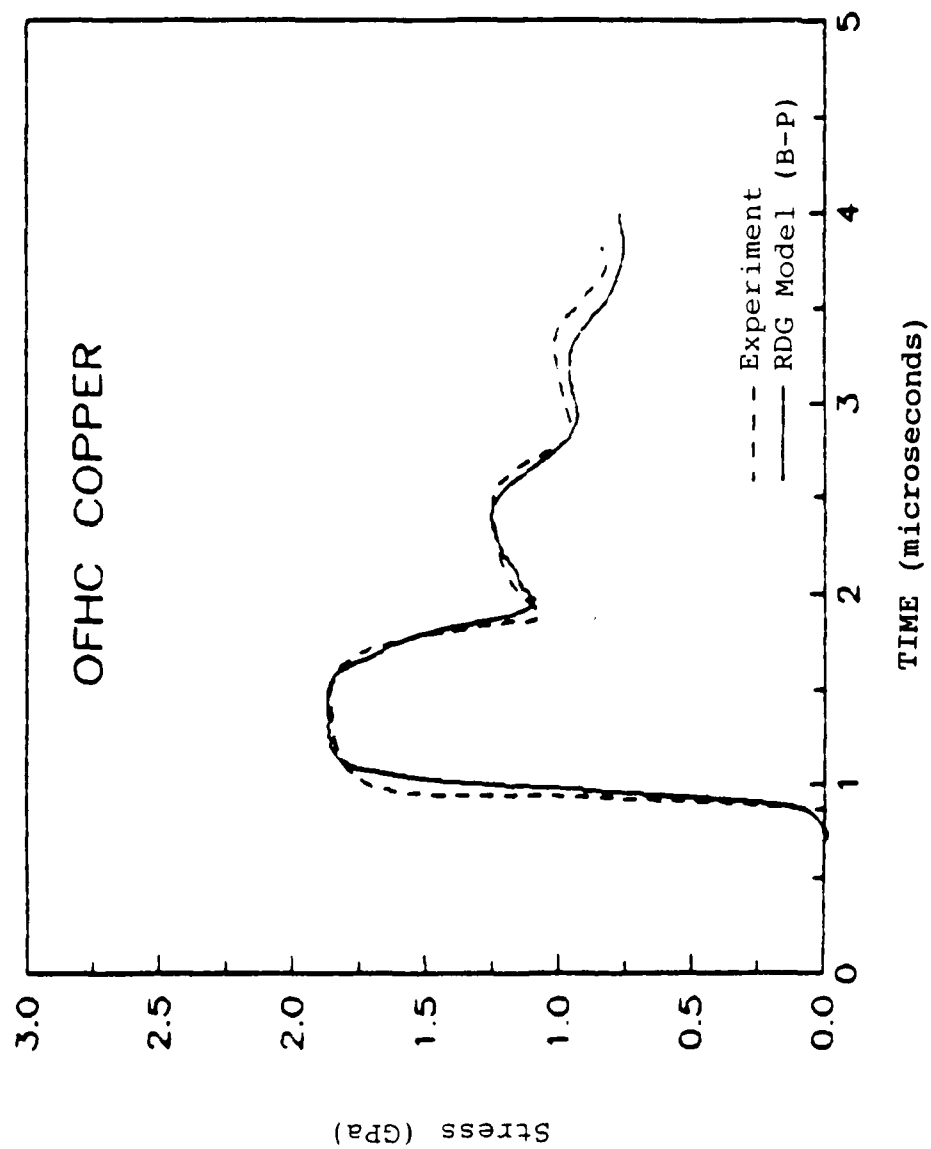


Figure 13. Comparison between model prediction and the measured stress history (OFHC copper).

plate. The previously determined RDG model parameters for OFHC copper had been used in this simulation.

In the first simulation of the double flyer plate experiment, the RDG model predicted the initial spall signal reasonably well but was unable to accurately reproduce the experimental recompaction signal, as indicated by Figure 15. The plastic wave slope of the simulated reshocking exhibited ramping with a long rise time indicating that the predicted pore collapse, described by the same equations as void growth, was unrealistically slow and required modification. Grove et al. [38] introduced a complete collapse of the microvoids in a particular element if that element's dilatation rate was negative and its void volume fraction was less than or equal to some critical value. Figure 16 shows the excellent fit to the experiment obtained when the critical void volume fraction for complete collapse was five percent.

The double flyer plate experiment without void growth was also simulated so that the microvoids effect on the reshock signal could be investigated. Figure 17 compares the two simulations, with and without void growth. It is interesting to note that the dip at point F occurs at the same time in both curves, indicating that this feature is directly related to the experimental configuration. Figure 18 shows an x-t (distance-time) diagram for the double flyer plate impact experiment, assuming no void growth. In this figure, the solid and dashed lines represent shock and release waves, respectively. The release and shock waves that arrive at points E and F are solely due to the impedance mismatch between the first flyer and the target. Because the first flyer has a lower impedance than the target, it separates from the target at about 0.75 microseconds. As Figure 18 indicates, the initial shock wave from the second flyer reflects off the free surface of the first flyer as a release wave because of the gap formed between the first flyer and the target. This release wave can be traced to point E. When the first flyer impacts the target again, another shock wave is produced, and this shock wave can be traced to point F in the x-t diagram.

In the absence of microvoid nucleation and growth, the shock wave from the second flyer would arrive at point C. When void growth occurs, however, this signal is delayed because of the reduced wave speed in the porous region of the target. Arrival of this signal at point C' (in Figure 17) signifies that the microvoids have completely collapsed. Since the release and shock

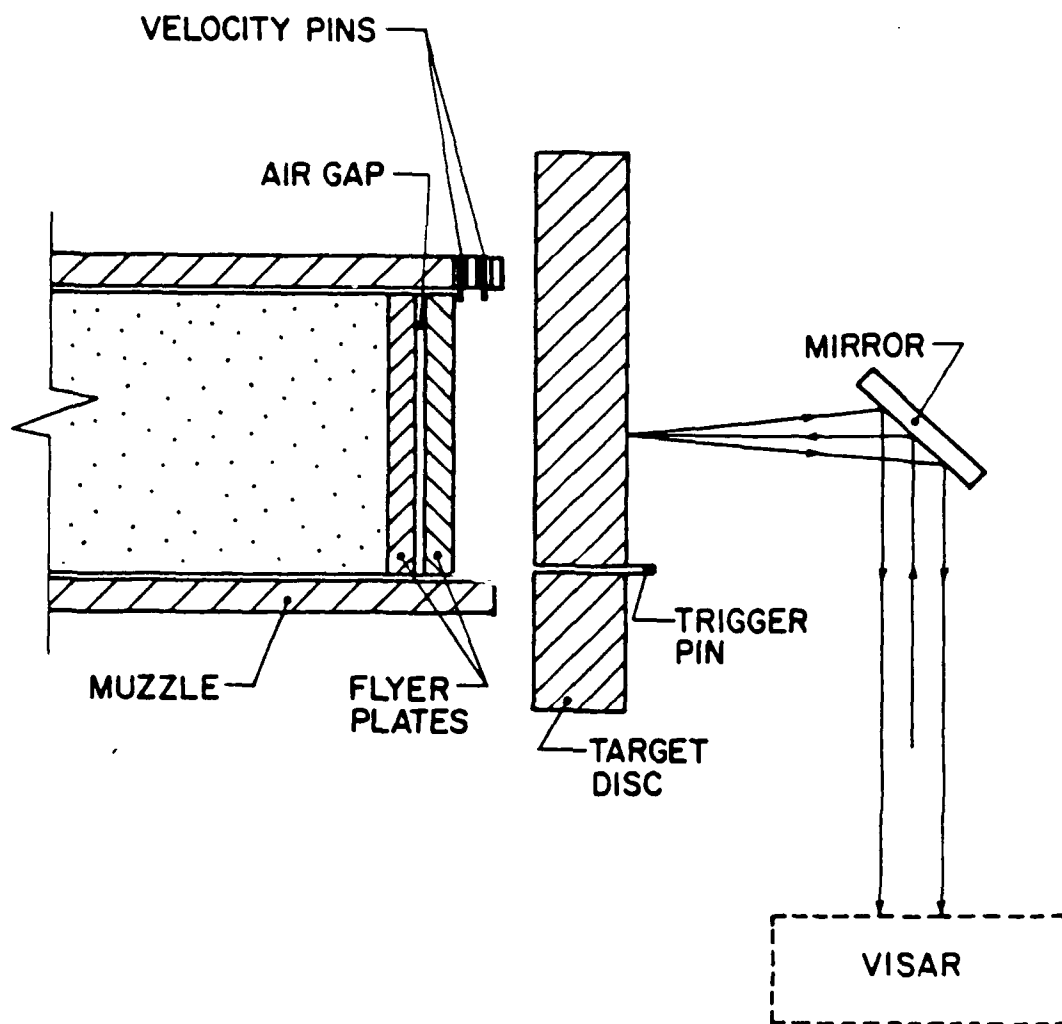


Figure 14. Experiment Configuration for Double Flyer Impact Experiment.

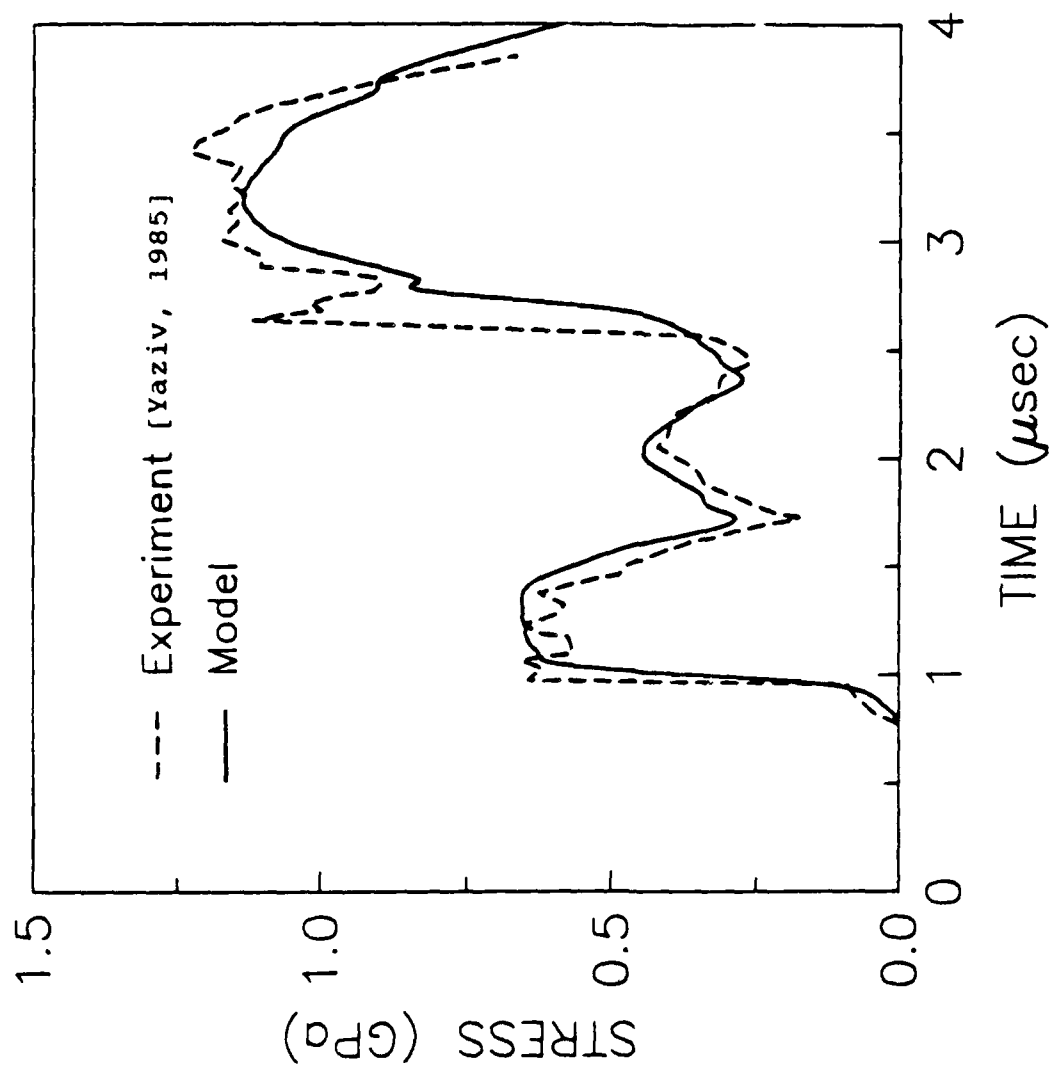


Figure 15. Stress history comparison for original RDG model.

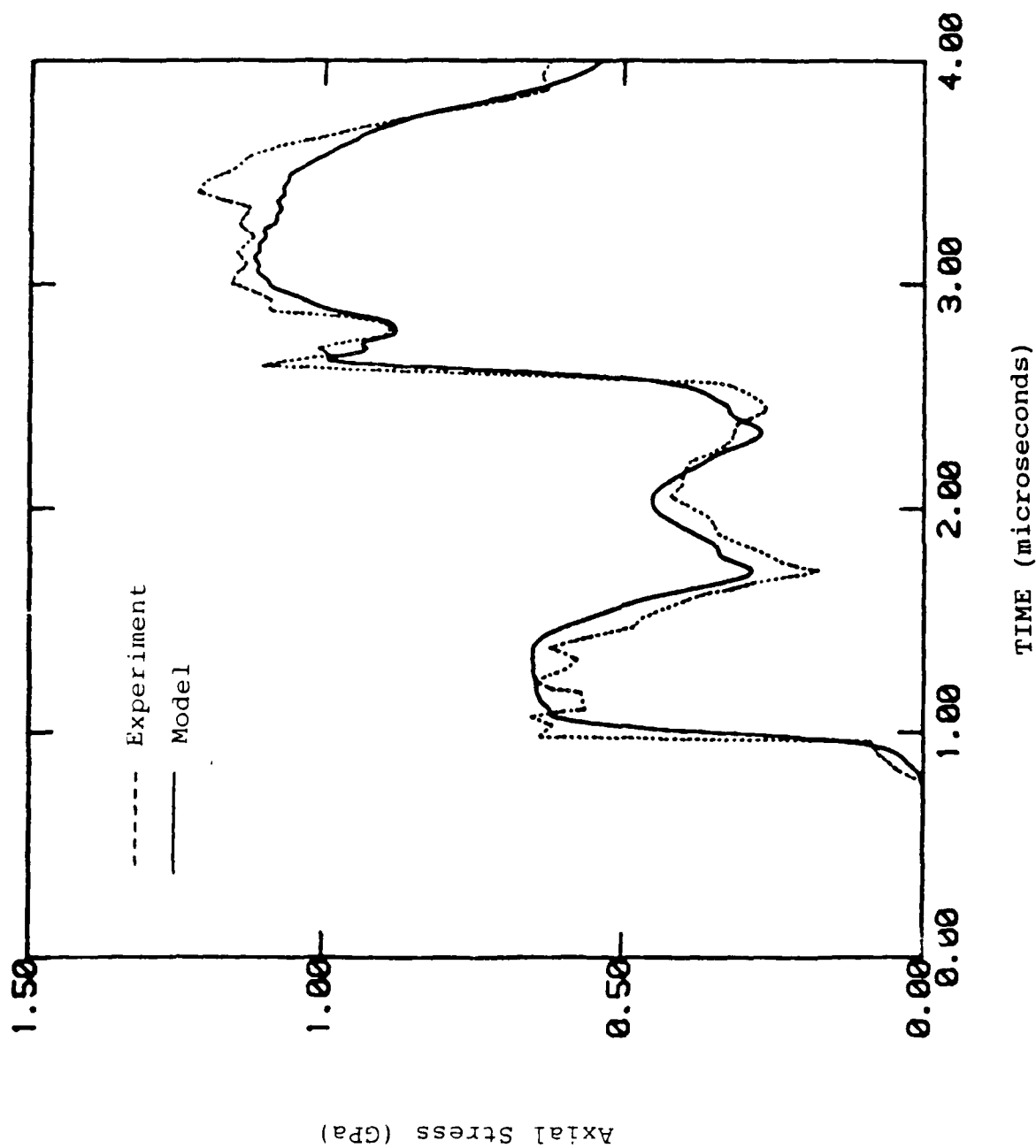


Figure 16. Stress history comparison for modified RDG model, with a critical void volume fraction of 5% for complete collapse.

waves at points E and F arrive after point C', it appears that they are unaffected by the void growth phenomenon.

In summary, a double flyer plate impact experiment was successfully simulated using the RDG model. Using previously calibrated constants, the RDG model was able to reproduce the initial spall signal, but the reshock signal did not compare as well with the experimental stress history. The RDG model was modified to include a simple void collapse criterion in which the microvoids were forced to completely collapse below a critical void volume fraction when the dilatation rate was negative. Microvoid collapse in OFHC copper was successfully modeled using precalibrated RDG model constants and a critical void volume fraction for complete collapse of 5 percent. Thus, the RDG model has been extended to describe microvoid collapse as well as a history dependent failure process.

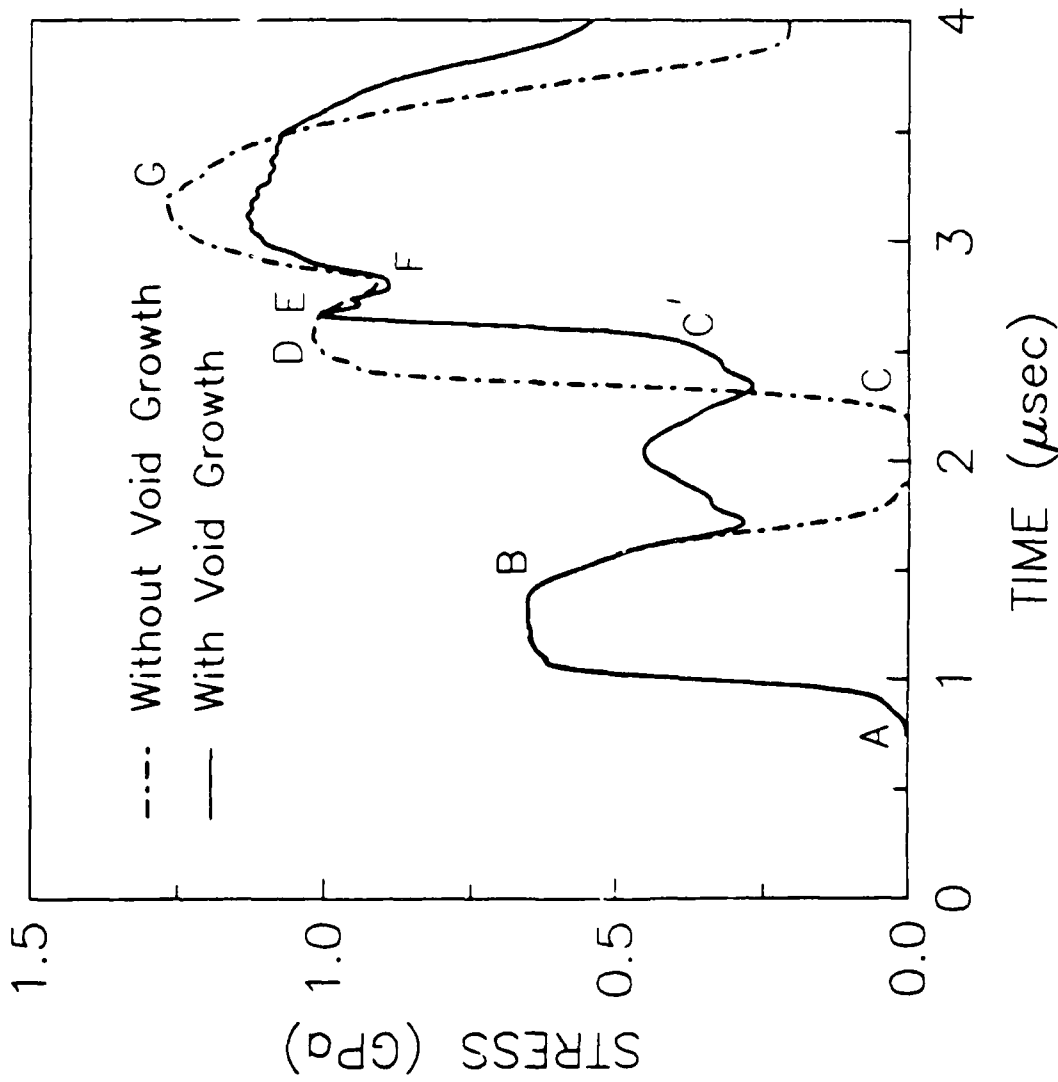


Figure 17. Comparison of simulated stress histories from double flyer impact configuration, with and without void growth.

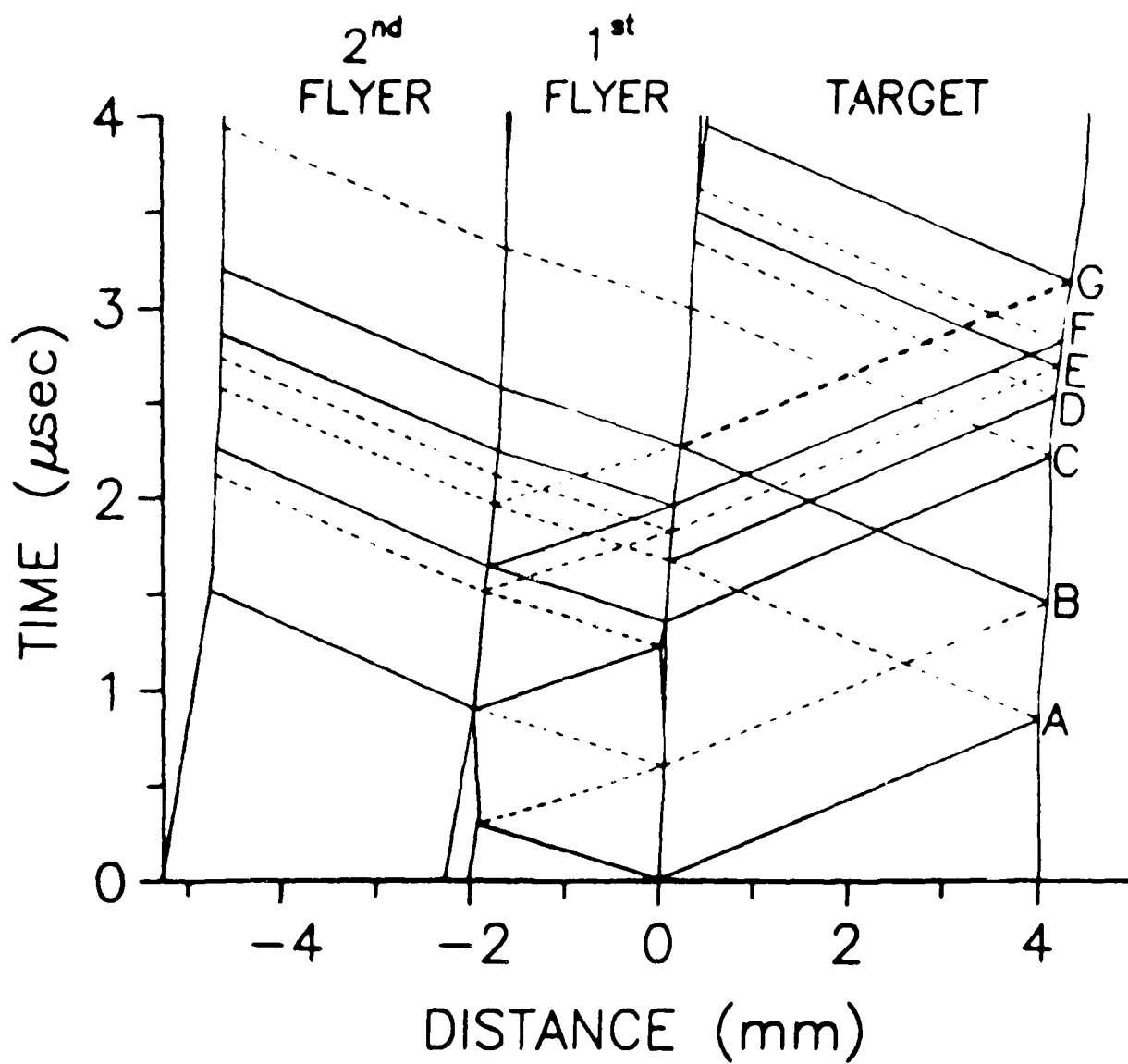


Figure 18. x-t diagram for the double flyer impact experiment, assuming no void growth. This corresponds to the dashed line in Figure 17.

6. RDG MODEL APPLICATIONS

The dynamic ductile failure also occurs in other types of configurations. Tensile necking in a split Hopkinson bar test and spallation in a target plate impacted by a long rod penetrator are a few examples. These two configurations are investigated in the following sections.

6.1 Tensile Necking

To further demonstrate the capability of RDG model, several two dimensional axi-symmetric configurations were considered. The first case considered the problem of dynamic tensile necking. The main objective of this two dimensional analysis was to examine the stress states, evolution of necking, void growth as influenced by the plastic deformation, and ductility. To initiate necking, a shallow-notched copper specimen was considered. This is shown schematically in Figure 19. The length and uniform diameter of the specimen are 0.35 and 0.125 inches respectively. The minimum diameter at the notch is 0.105 inches. The length represents the actual gauge length of a standard SHB tensile specimen.

The shallow notched specimen was modeled using the quadrilateral element option in the EPIC-2 code. Due to specimen symmetry, it is sufficient to model only one quarter of the specimen as shown in Figure 20. The Bodner-Partom (BP) model [22] was used to describe the high strain rate behavior of the copper specimen. The BP model constants for copper are given in Table 1. A typical experimentally measured SHB pull velocity was applied to the specimen in the simulation. The velocity was linearly increased from zero to 50.8 m/sec (2000 inches/sec) for 40 microseconds, and afterwards, it was kept constant.

The RDG model [1] was used to describe the necking evolution, and the corresponding constants are given in Table 4. A mean-effective plastic strain based Gaussian distribution as described by equation [9] was used for void nucleation. The corresponding RDG model constants are given in Table 4. Since the stress level under uniaxial stress state is considerably lower than the level under uniaxial strain condition (plate impact test), the void nucleation was assumed to occur entirely due to large plastic flow around the inclusions and oxide particles. In a uniaxial tensile test, the necking often

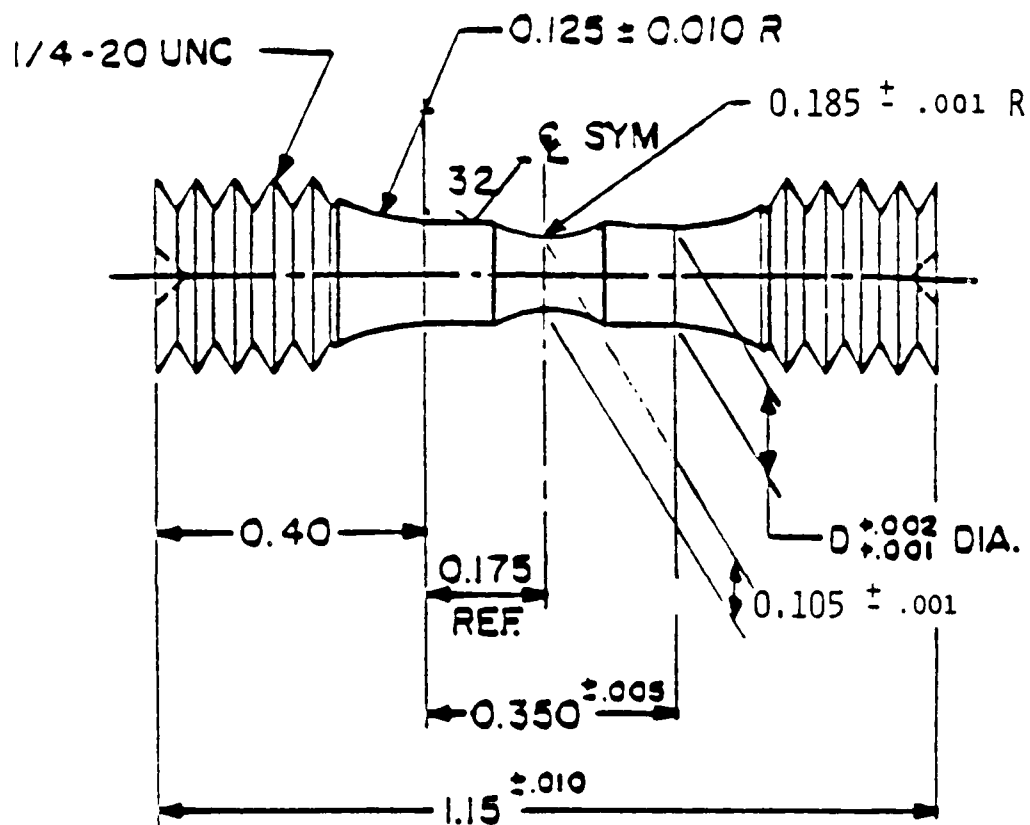


Figure 19. Shallow-notched tensile specimen geometry.

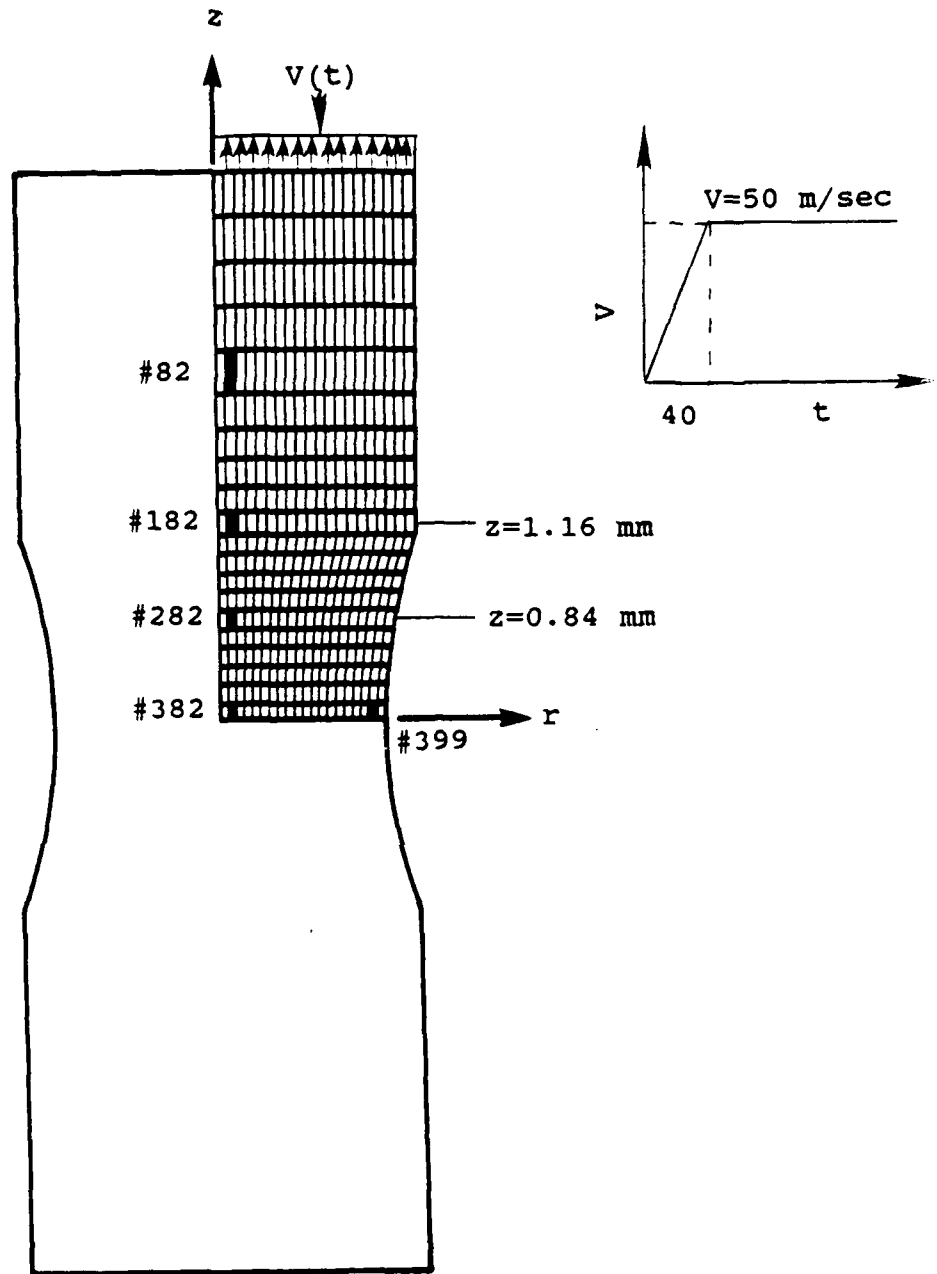


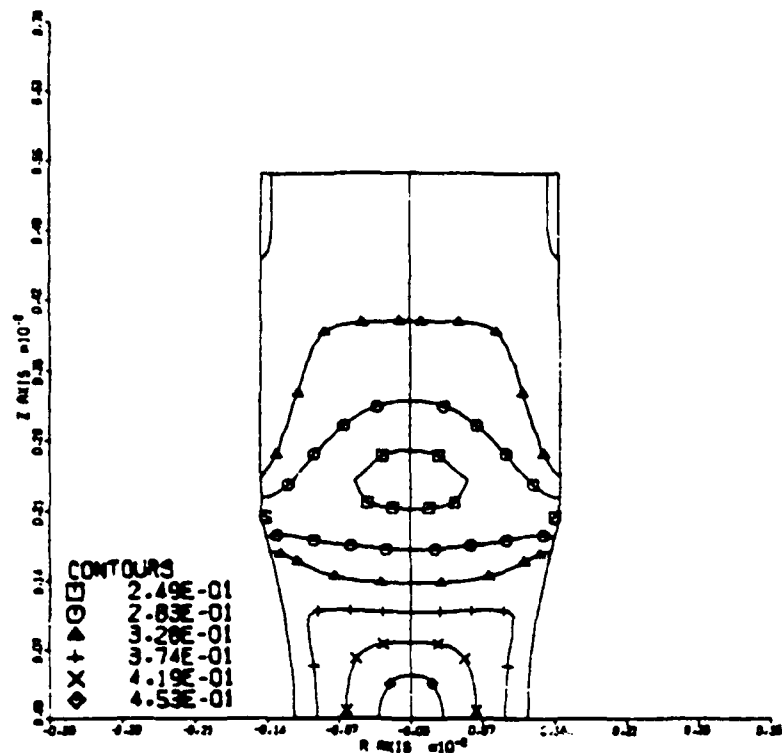
Figure 20. Finite element mesh for shallow-notched SHB specimen. The velocity loading history is shown in the inset.

progresses under significant plastic flow and a moderate triaxial stress state.

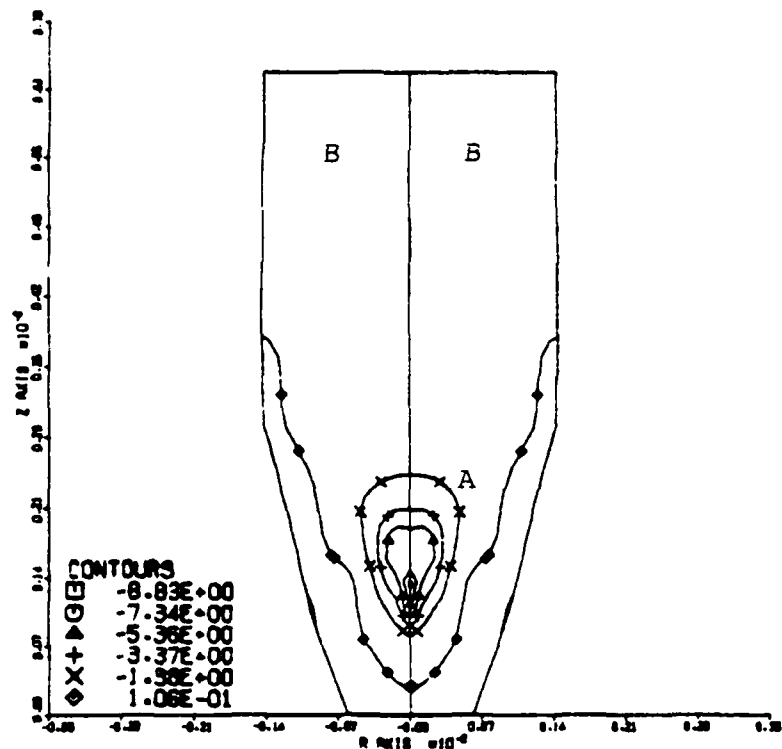
In the analysis, the time histories of effective stress, effective plastic strain, void volume fraction, and triaxiality of the stress state (ratio of pressure and effective stress) were evaluated for elements #82, #182, #282, and #382 as shown in Figure 20. Variation of pressure, stress components, strength, and other variables along a radius (snapshots) for different time intervals have also been considered in the analysis.

The stress triaxiality parameter (P/Y) contours are plotted in Figure 21. While this parameter is increasing at the specimen center, the stress state is under uniaxial stress condition (P/Y is around $1/3$) for the uniform shaded region. The triaxiality ratio becomes negative (compressive) around region A as can be seen from Figure 21b. The unloading of the uniform section (region B) and the compressive loading at A make the interpretation of the triaxiality contours complicated. In the presence of increased triaxiality, the void growth also increases as shown in Figure 22. The void volume fraction contours at $t=0$, 20, 50, and 60 microseconds are shown. Initially, a small amount of voids nucleate near the stress-free notch surface. The void distribution spreads toward the specimen center with increasing necking. By about 50 microseconds, the void content at the center region increases rapidly to 3 to 4 percent. Due to increasing triaxial tensile state, rapid void growth occurs during the next 10 microseconds; by $t=60$, the necked region is filled with voids, over 40 percent located at the center (see Figure 22d). Although the void nucleated near the surface, the failure initiation eventually occurs at the center of the specimen. Hancock and Brown [39] provided the physical evidence to support failure initiation at the center in notched tensile specimens for various notch geometries under quasi-static loading conditions.

The time history plots of effective plastic strain and void volume fraction for regions near the neck (local, element #382) and away from the neck (uniform, element #82) are given in Figure 23. Initially, the plastic strains are identical at both regions. However, the local strain at the center of the specimen starts deviating from the uniform strain slowly due to enhanced void growth. The void nucleation process occurs during the first 40 microseconds, and rapid growth initiates around $t=50$. Beyond this time, while

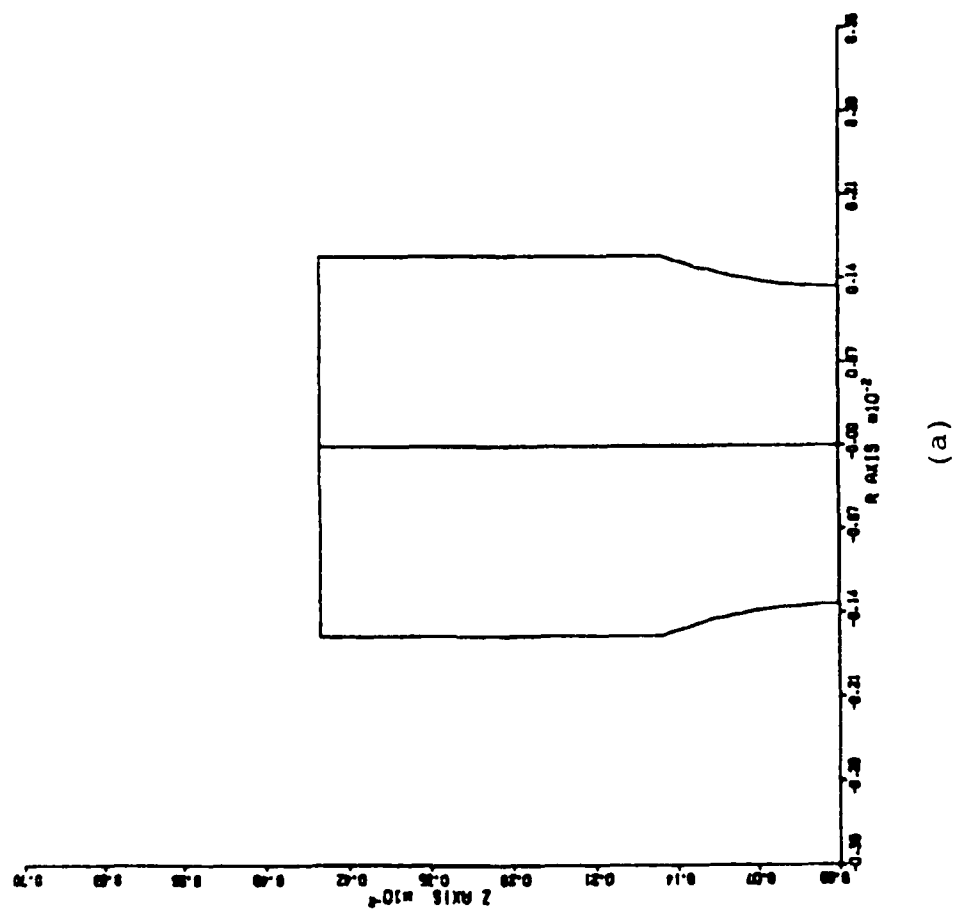


(a)

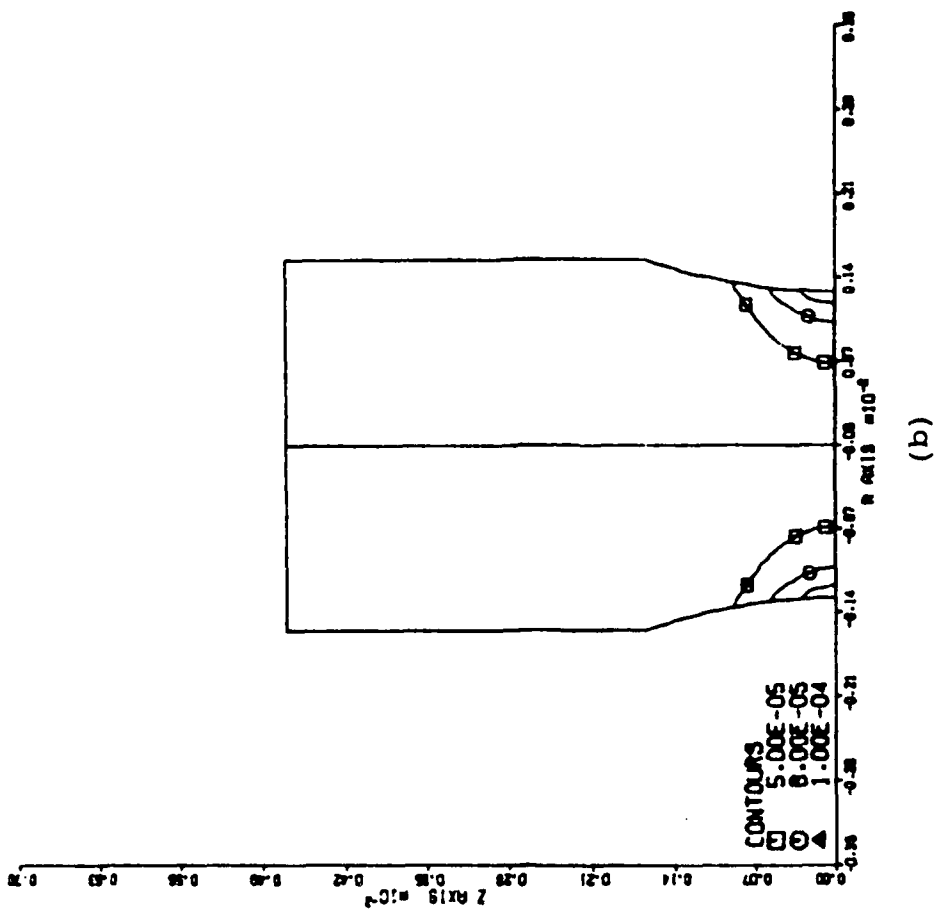


(b)

Figure 21. Stress triaxiality (P/Y) at (a) $t=40$, (b) $t=50$, and (c) $t=60$ microseconds.



(a)



(b)

Figure 22. Damage (void volume fraction) contour at (a) $t=0$, (b) $t=20$, (c) $t=50$, and (d) $t=60$ microseconds.

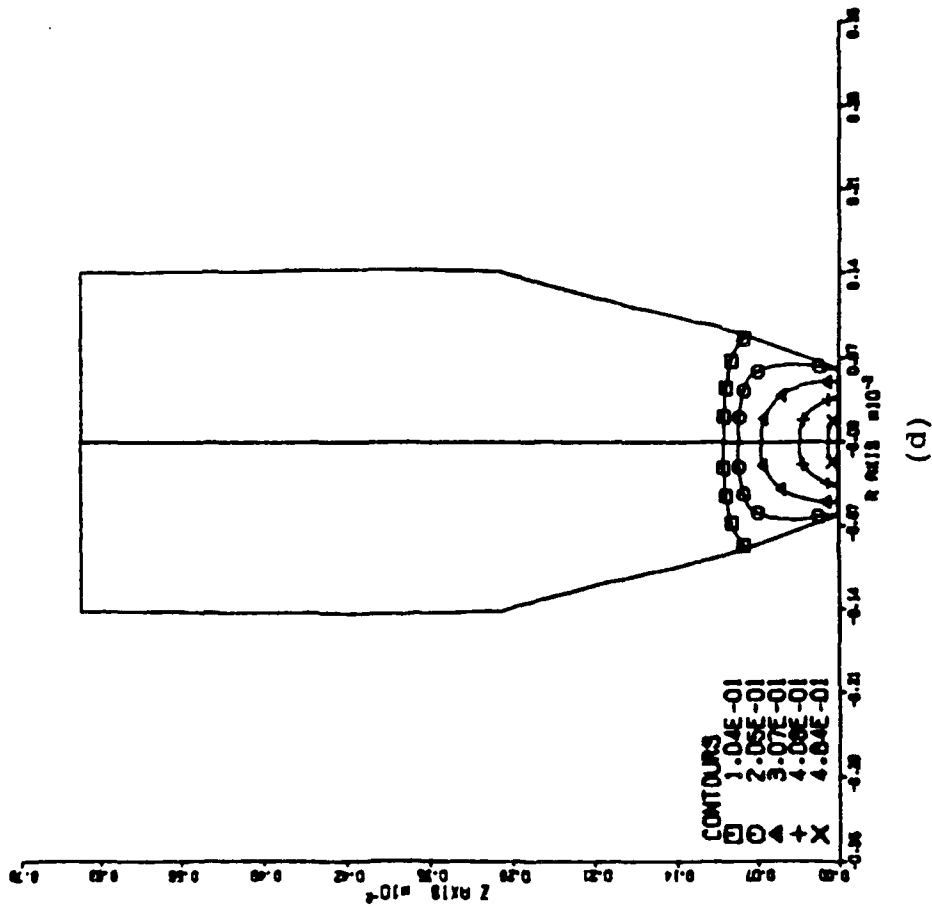
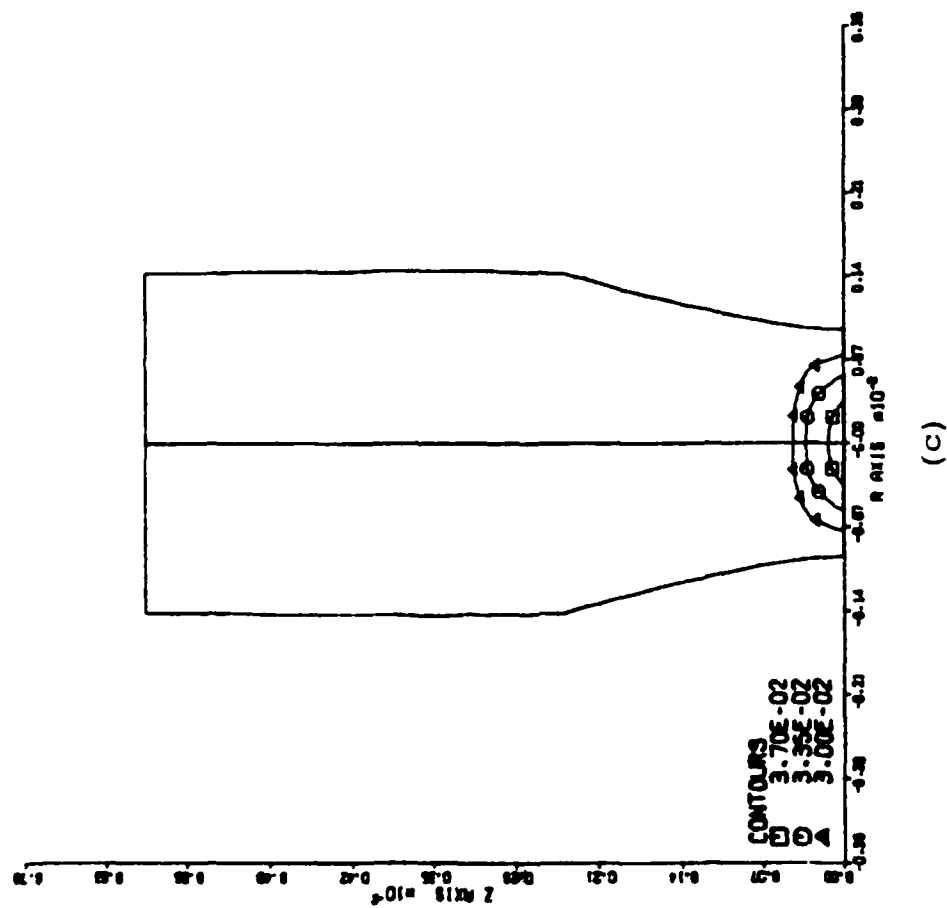


Figure 22. Damage (void volume fraction) contour at (a) $t=0$, (b) $t=20$, (c) $t=50$, and (d) $t=60$ microseconds (concluded).

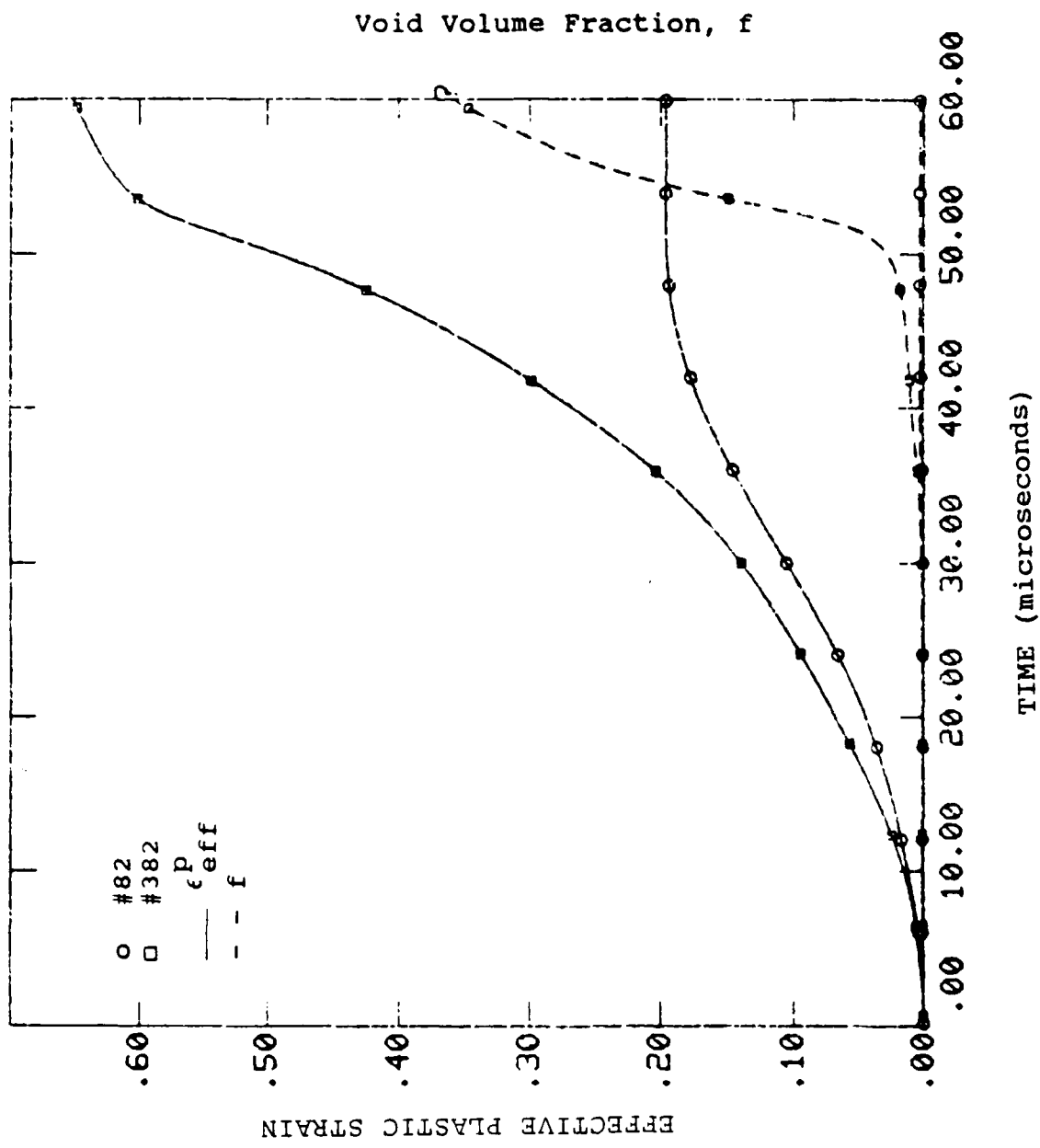


Figure 23. Time histories of effective plastic strain and void volume fraction for elements #82 (uniform section) and #382 (local section).

the local strain continues increase due to void growth, the uniform strain at element #82 (see Figure 20) reaches a maximum value of 20 percent and stopped increasing. This is obviously due to unloading of the sections away from the local necking region, shown in Figures 24-26.

The stress-time history for the local and uniform regions are shown in Figure 24. Also shown in this figure is the void volume fraction history for elements #82 and #382. Since these two elements are very close to the axis of symmetry, the hoop and radial stresses are identical (Figure 24). For the uniform element (#82), the hoop and radial stresses are zero as one would expect. However, the stress state in the local element #382 begins almost uniaxial and becomes triaxial due to necking. The hoop and radial stresses increase as the void growth occurs in the local region generating a high triaxial stress state locally. Between 40 and 50 microseconds, this stress state accelerates the necking process. As rapid void growth occurs at 50 microseconds, the axial as well as hoop and radial stresses relax (at point A') in local element #382. The word 'relax' indicates the decreasing stresses with increasing plastic strains. However, the axial stress actually unloads in uniform element #82 (at point A in Figure 24) due to rapid localization of the deformation. Since no void growth occurs in this uniform region, the decreasing stresses are only due to unloading. In regions away from the neck, the material is intact without any voids, and, therefore, the possibility of any strength degradation leading to stress relaxation does not exist. To further demonstrate these aspects, effective stress versus effective plastic strain is shown in Figure 25. The void volume fraction history has also been included. The stress (strength degradation) relaxation beyond point A can be seen in this figure. The plastic strain continually increases because of the void growth induced plastic flow. As the void volume fraction increases, the strength continues to decrease.

The mean stress (pressure) histories at various locations are plotted in Figure 26. As mentioned earlier, #82 represents the uniform region and #382 represents the local region. The elements #282 and #182 are the intermediate regions (see Figure 20). The stress triaxiality (defined as the ratio of mean stress and effective stress) due to the initial notch leads to a higher mean stress level in the local region before the occurrence of necking. When necking initiates around 40 microseconds, the regions (#82 and #182) away

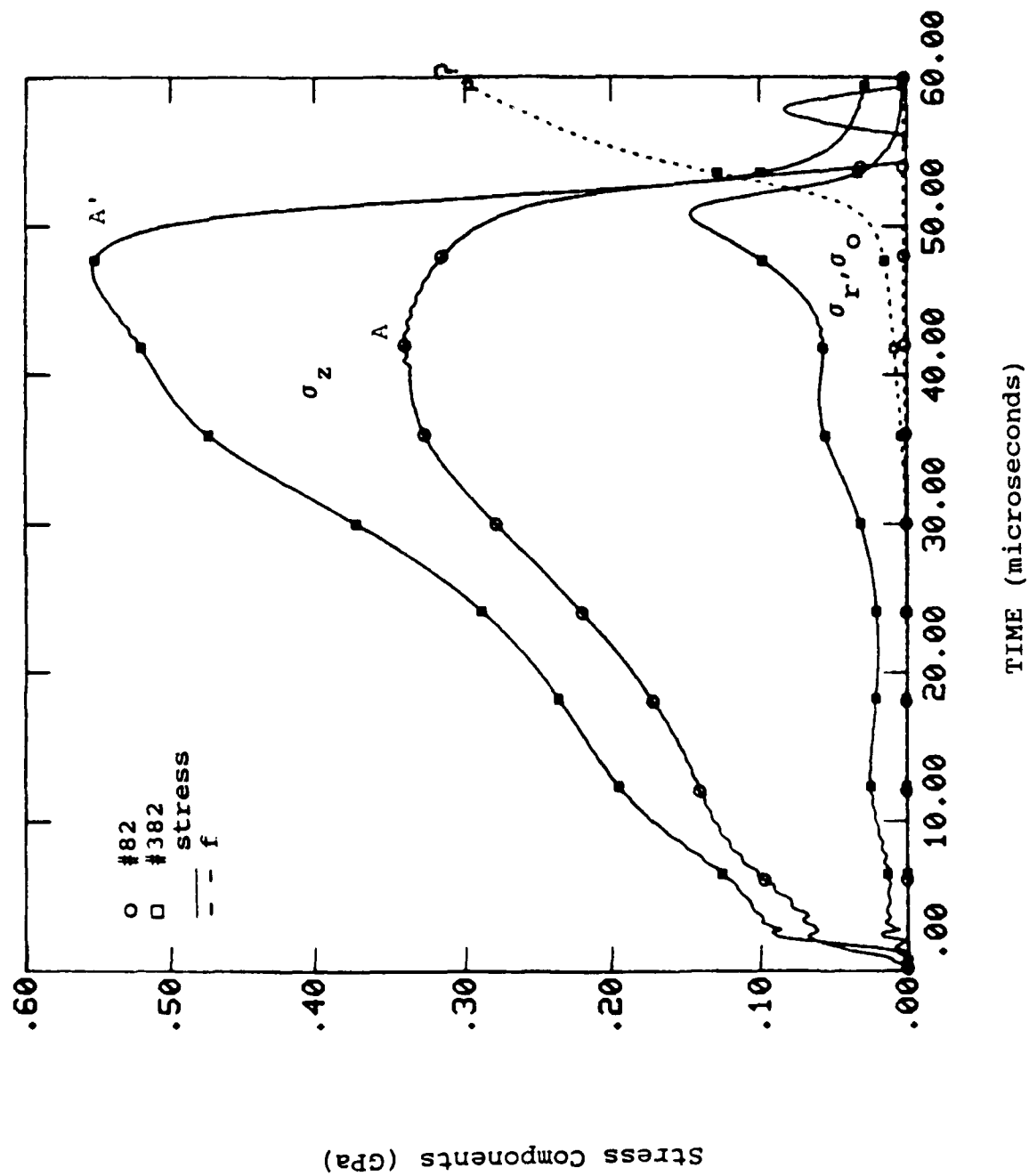


Figure 24. Time history plots for the stress components and void volume fraction.

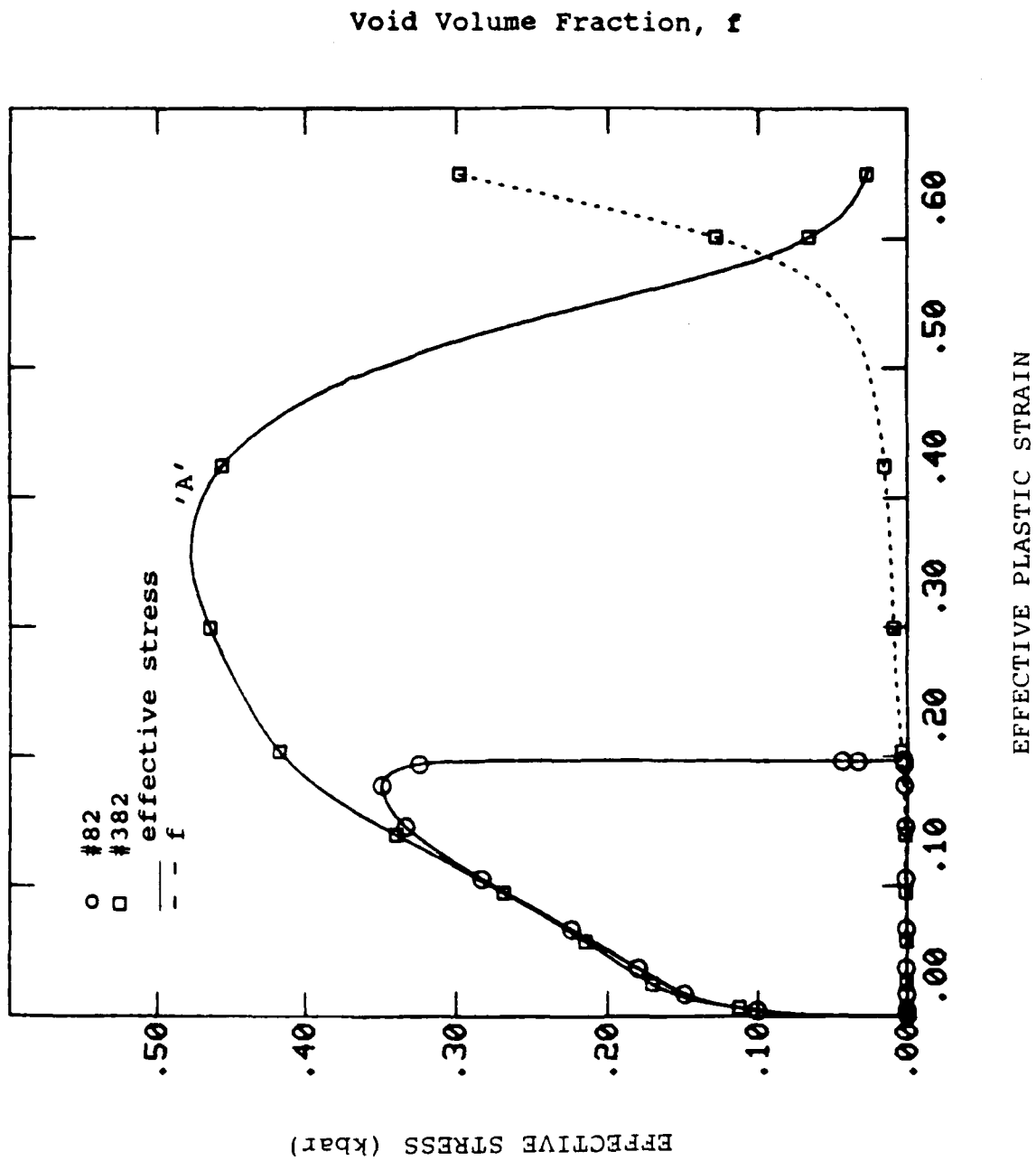


Figure 25. Stress-strain response for #82 and #382 along with the variation of f with respect to effective plastic strain. Note that $f=0$ for #82.

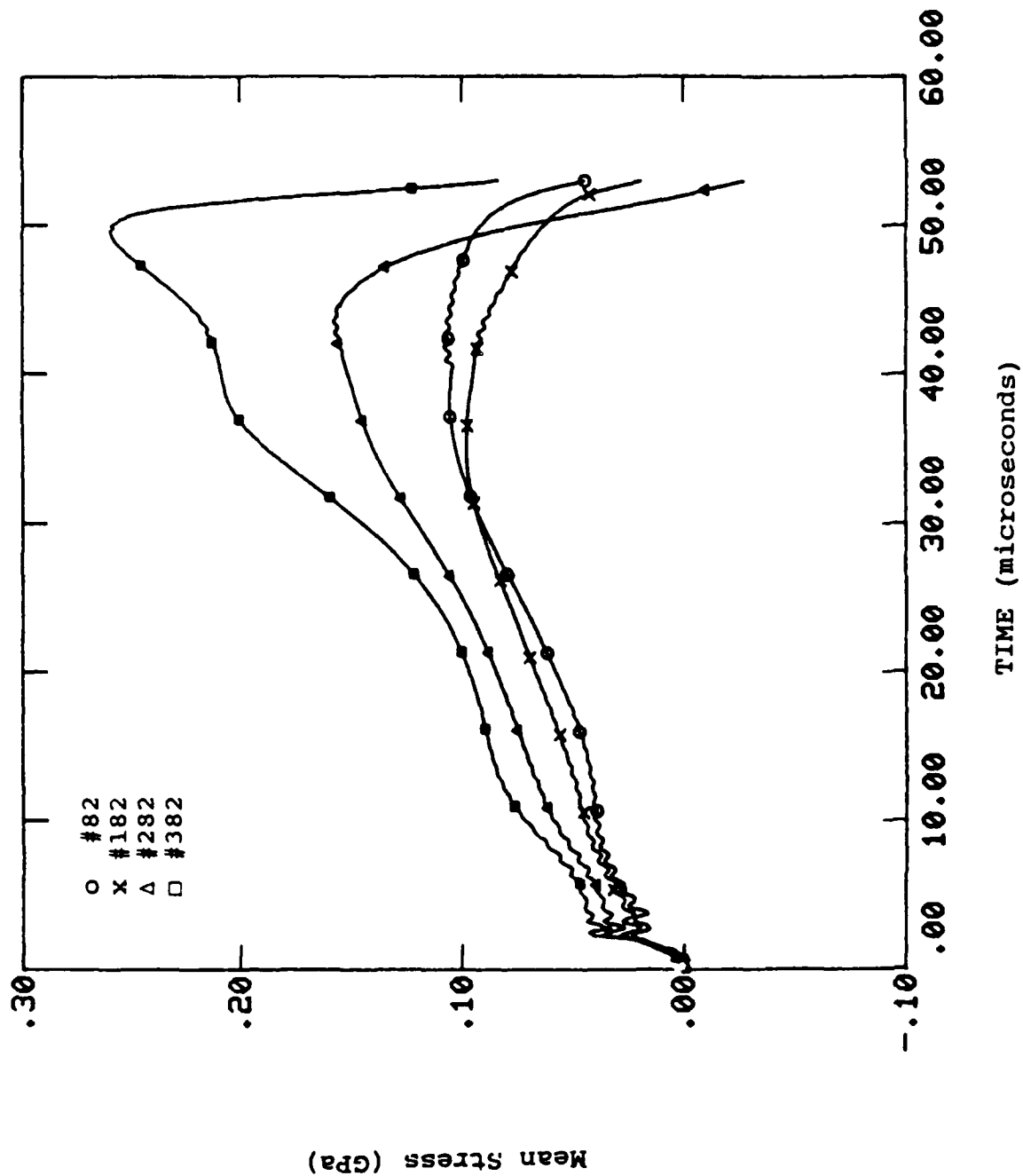


Figure 26. Time history plot of mean stress for elements #82, 182, 282, and 382.

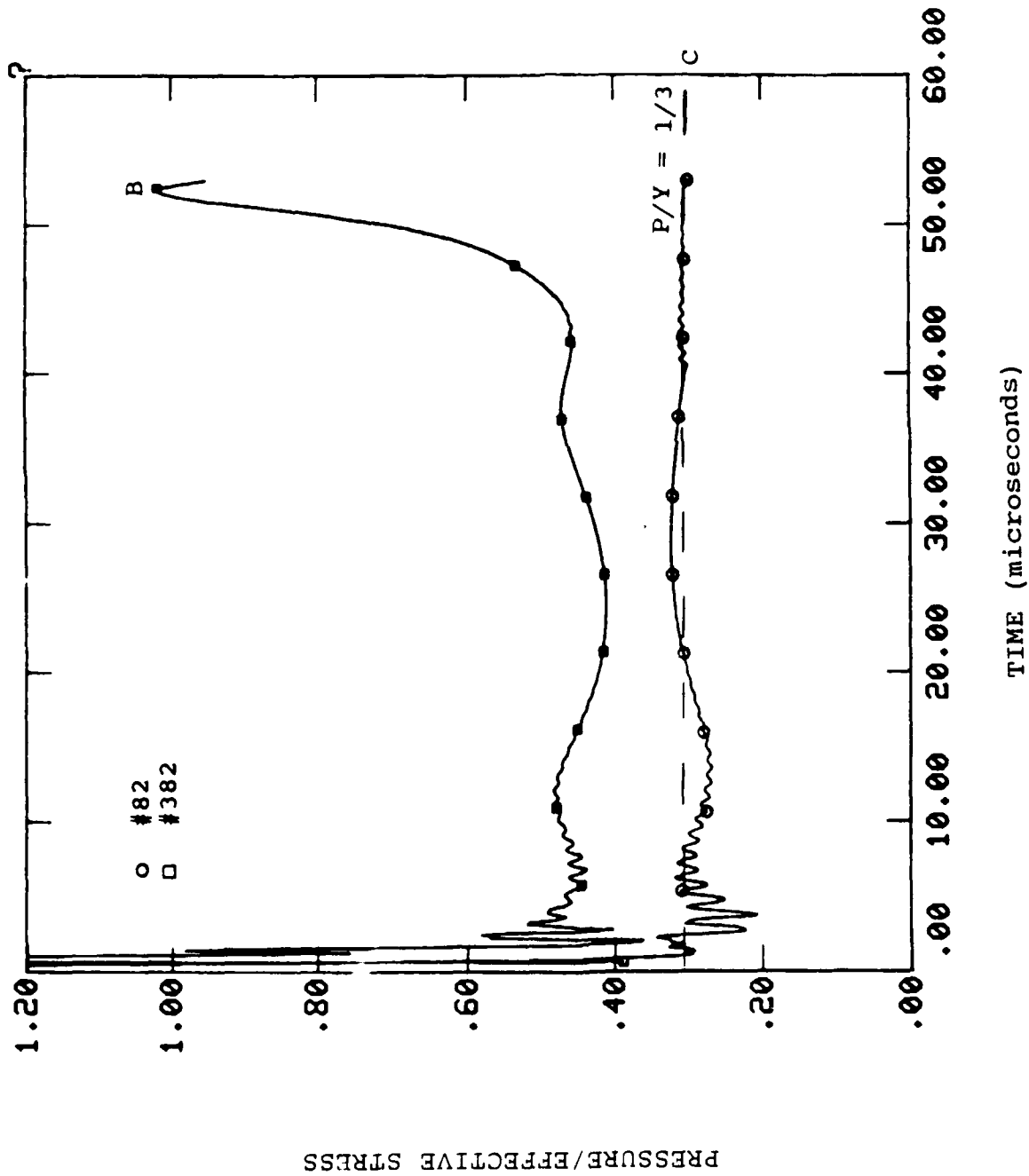


Figure 27. Measure of triaxiality with respect to time for the uniform (#82) and local (#382) sections. The dashed line represents the uniaxial stress state.

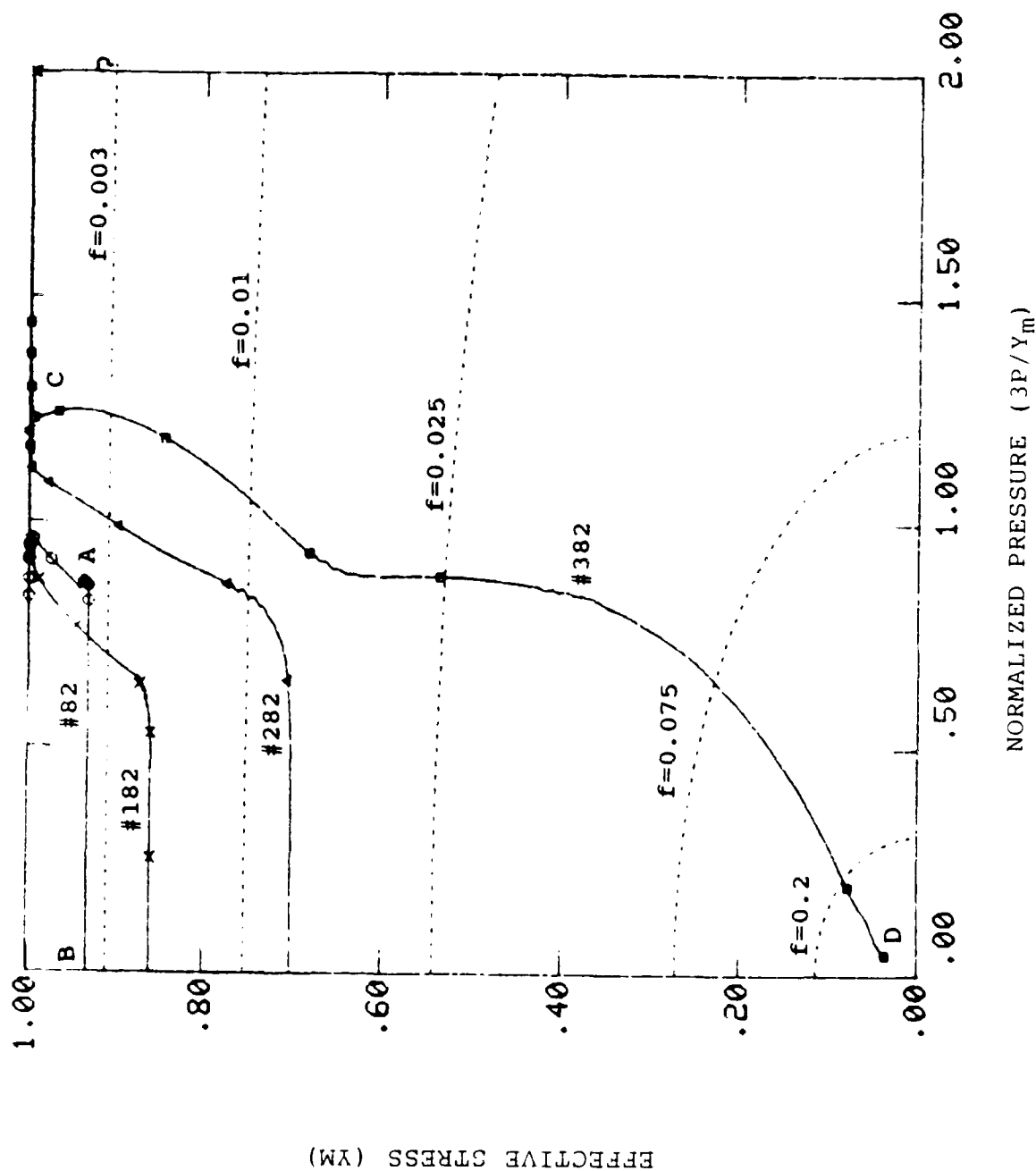


Figure 28. Loading paths with respect to pressure dependent yield surfaces in elements #82, 182, 282, and 382.

from the neck start unloading. While the pressure decreases because of unloading in these regions, the mean stress relaxes due to void growth in the local regions.

The stress triaxiality is plotted with respect to time for elements #82 and #382 in Figure 27. The uniform region remained closely under uniaxial stress state. The ratio of mean stress and effective stress was almost $1/3$, as one would expect. The slight deviation from this value before 20 microseconds is numerical, and later this ratio remains close to $1/3$. For the element in the local region, the stress triaxiality is initially greater than $1/3$ due to the notch. However, as necking occurs between 40 and 50 microseconds, the local triaxiality rapidly increases in Figure 27. Beyond point B, rapid void growth leads to strength degradation and failure initiation. For further understanding the loading conditions, the loading paths are shown at different locations with respect to the pressure dependent yield surfaces in Figure 28.

The loading paths for elements #82, #182, #282, and #382 are described by plotting the ratio of effective stresses of the aggregate and the fully dense matrix (σ_{eff}/Y_m) and the ratio of mean stress and effective stress of the matrix (P/Y_m). Since the material is initially void-free, the plastic yielding is pressure independent. Therefore, the loading path starts at $\sigma_{\text{eff}}/Y_m = 1$ as shown in Figure 28. The dotted lines represent the elliptical yield surfaces for various levels of porosity. In element #82, a small amount of void nucleates initially and grows very little. The corresponding loading path is shown between points A and B. The loading remains on the yield surface for void volume fractions less than 0.3 percent. In a similar manner the loading path for element #182, which is away from the notch zones, is confined to a yield surface corresponding to $f = 0.01$. Because of enhanced void growth in the local regions, a significant amount of void growth occurred, especially in element #382 as between points C and D in Figure 28. As the loading path proceeds along the shrinking yield surfaces, the material strength degrades to less than 80 to 90 percent of the original intact material, indicating failure of the material.

For completing the discussions of the RDG model capabilities, additional analyses in terms of snap shots and additional contour plots are

presented. The snap shots are plots that describe the distribution of a variable with respect to position (for example, radial distance from the axis-of-symmetry). In the snap shot plots, the radius is normalized with respect to the initial notch radius. In Figure 29, the snap shots of void volume fraction for the three different z positions, shown earlier in Figure 20, are plotted. The z position describes the position along the specimen length that is away from the minimum cross section (c/s) of the shallow notched tensile specimen. Therefore, $z=0$ represents the minimum cross section. Since the triaxiality is largest at the center of the specimen ($r=0$ and $z=0$), the void volume fraction is maximum at the center and decreases toward the free surface ($r/r_0=1$). The present analysis is for a dynamically stretched tensile specimen. The loading duration is of the order of microseconds. Interestingly, the numerical results are very similar to a statically deformed specimen. These analyses compared qualitatively well with the results reported by Norris et al. [40]. They analyzed quasi-static necking deformation using a dynamic finite difference computer program. However, in the present work, the problem is considered as inherently dynamic and has been treated as a shock wave propagation problem. Due to several reverberations of the shock waves, the deformation is homogeneous, and the problem is dominated by inertial loading rather than the shock wave effects.

The snap shot of normalized effective stress of the voided-aggregate is given in Figure 30. At $t=20$ microseconds, the effective stresses of the matrix and the aggregate are almost the same due to insignificant void growth; therefore, the ratio is 1. When the void growth occurs at $z=0$ c/s, the aggregate strength degrades and the ratio becomes less than one. At 40 microseconds, the c/s at $z=0.84$ mm and the minimum c/s develop significant voids. The $z=0$ c/s degrades faster than the section at 0.84 mm. Since the void volume fraction is initially evenly distributed across the c/s (not shown in the figure), the reduction in strength is almost uniform. However, later at 50 microseconds, the non-uniform void growth in the intermediate section leads to rapid strength degradation near the axis ($r/a_0=0$) as shown between A and B in Figure 30. However, because of a lack of stress triaxiality near the surface, the void growth was not significant; correspondingly, the strength did not significantly degrade. At the minimum c/s, due to the enhanced void growth and void coalescence across most of the c/s, the strength degraded more

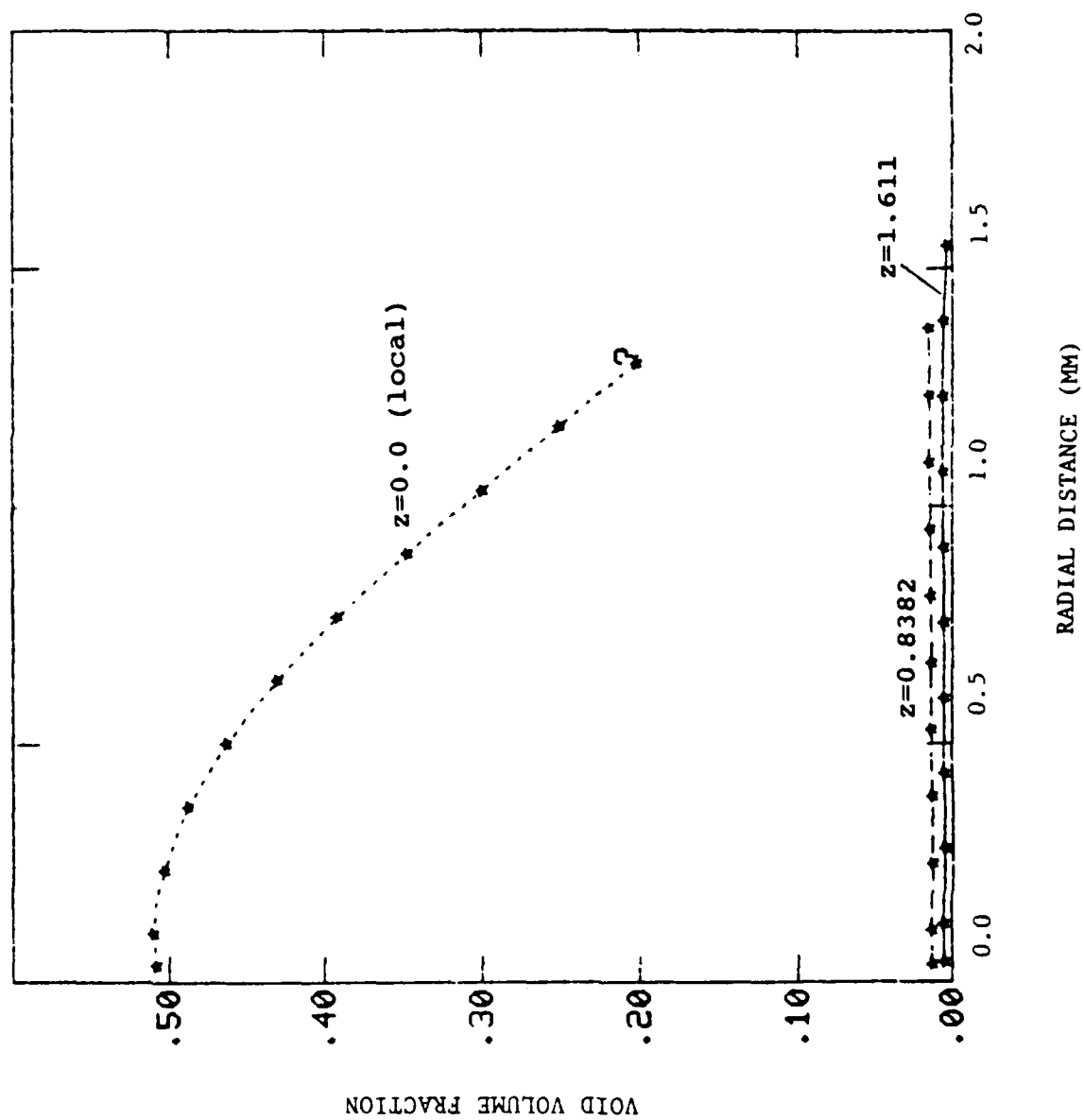


Figure 29. Radial distribution of void volume fraction at these different positions along the specimen length.

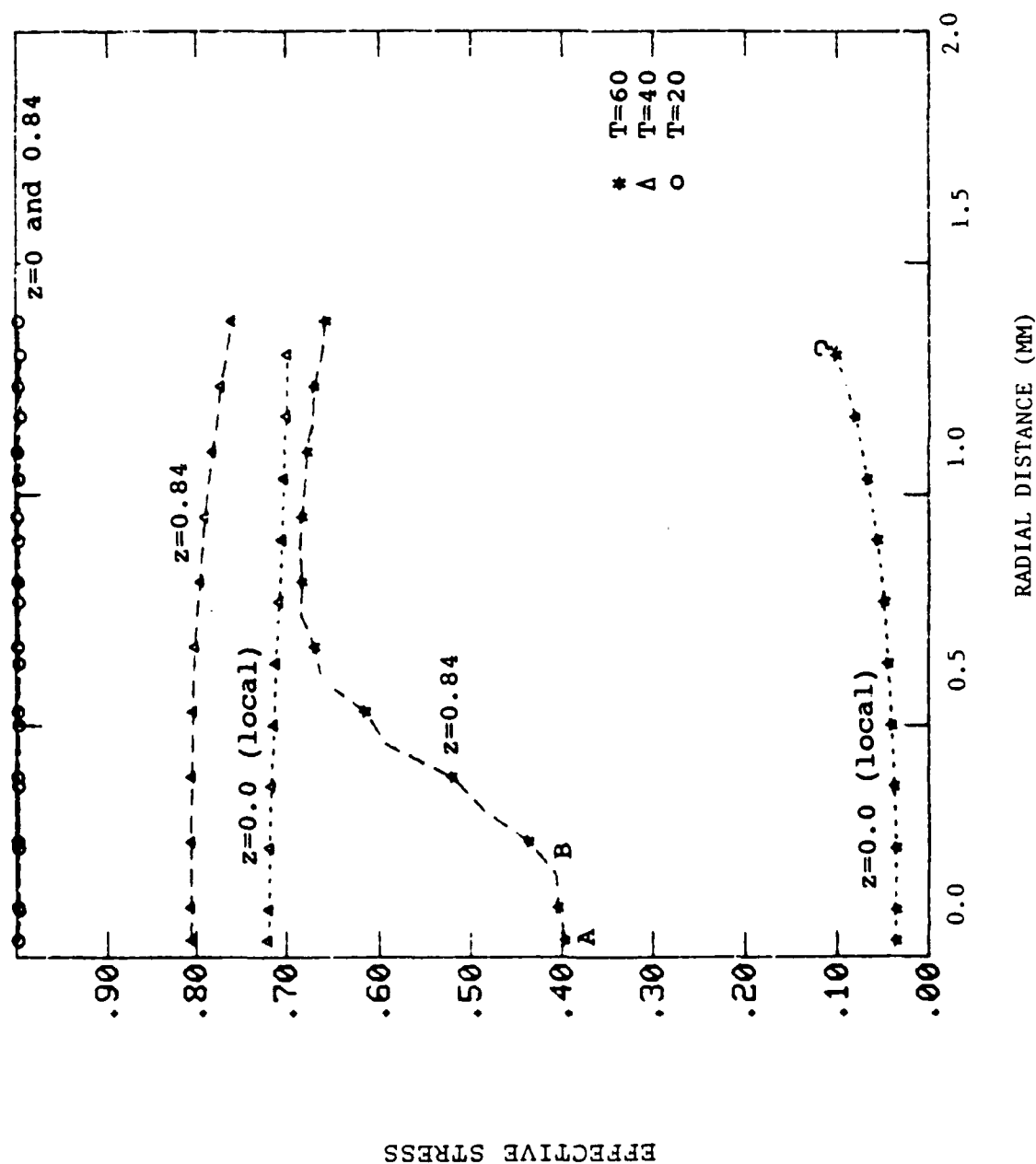


Figure 30. Normalized effective stress (σ_{eff}/y_m) distribution along the radius for different z positions and time intervals.

than 90 percent. This indicates failure initiation leading to total separation of the material.

For comparison, the necking process was also simulated without the voids. This simulation will be referred to as case 2 in the following discussions. The Bodner-Partom model described the material behavior. The solution was carried out for 60 microseconds. Since the boundary conditions for the two simulations were the same, the top section was moved (pulled) identically. Therefore, at any given instant, the specimen length was the same for both cases. Plastic strains were plotted based on: the ratio of current length and original length; uniform strain in element #82 for void-free material (case 2); and, uniform strain in element #82 for void-containing material (case 1) in Figure 31. As one would expect, the average strain based on the overall specimen length was larger than the uniform strains in element #82 for the two cases. While in case 2 the uniform section continues to deform at 60 microseconds, deformation no longer occurs in case 1 due to void growth controlled necking process. For this reason, the ductility reduced significantly in the presence of void growth.

The effective stress versus effective plastic strain in the local element for the cases with and without voids is shown in Figure 32. In the void-free case, the necking process continues beyond 60 microseconds. Since material degradation does not occur in this case, the effective stress (strength) follows the true stress-true strain curves generated by the BP model for OFHC copper (Figure 32). The drooping portion of the stress-strain curve (between points A and B) for the void-growth influenced necking case is due to strength degradation. Even though the loading (increasing plastic strain) increases beyond point A, the stress continually drops indicating void-softening in the material.

The effective plastic strain variations along a radius for the necking process with and without voids are shown in Figure 33. The variation along the minimum radius (local) indicates that the strain reached a maximum near the surface and not at the axis for both cases. These results differ from the tensile simulation results reported by Norris et al. [40] in which the plastic strain reached maximum at the axis. They considered a quasi-static necking problem in which the inertial effects were neglected. Since the present necking analysis considers the inertial effects, the difference in the effective

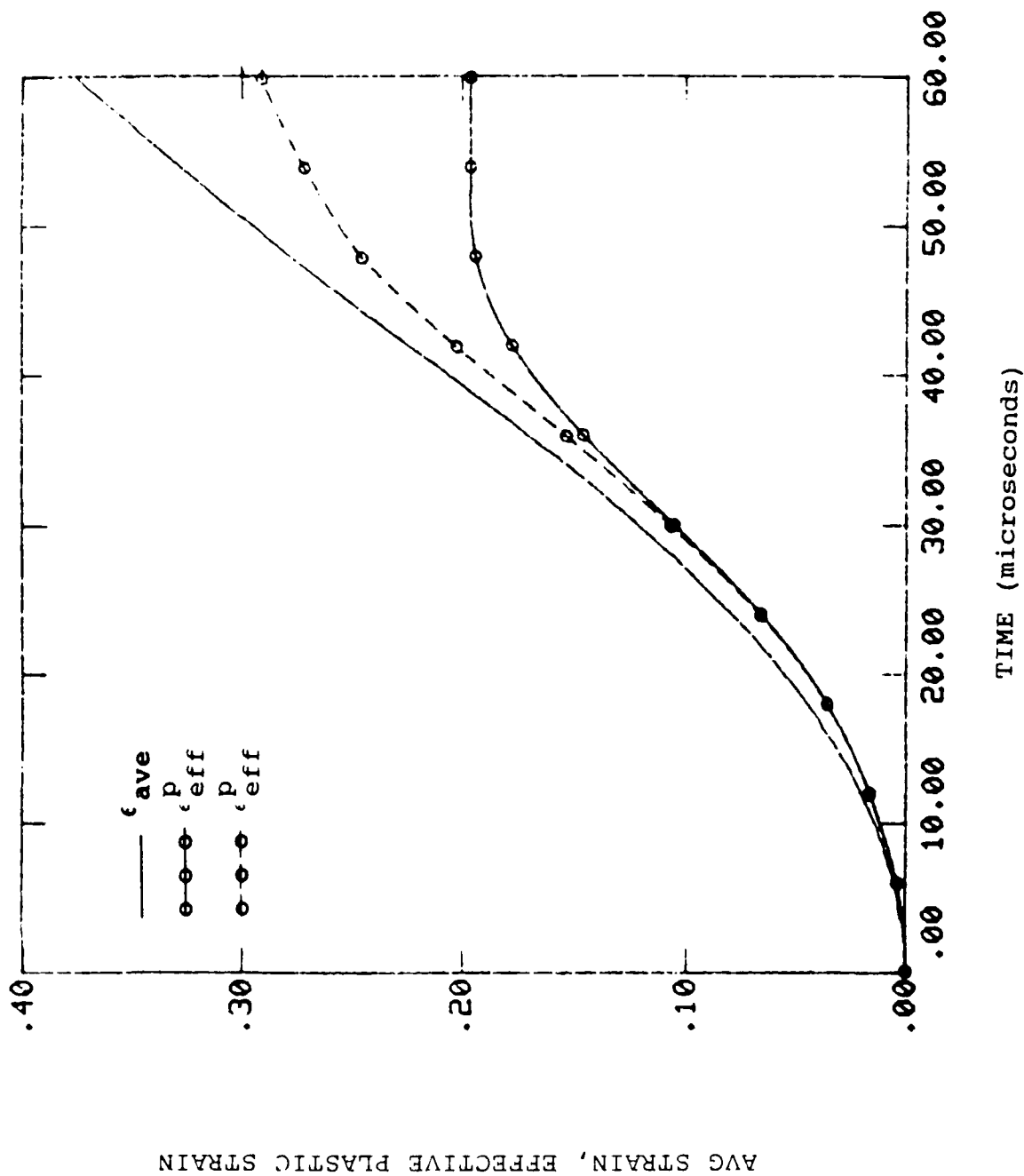
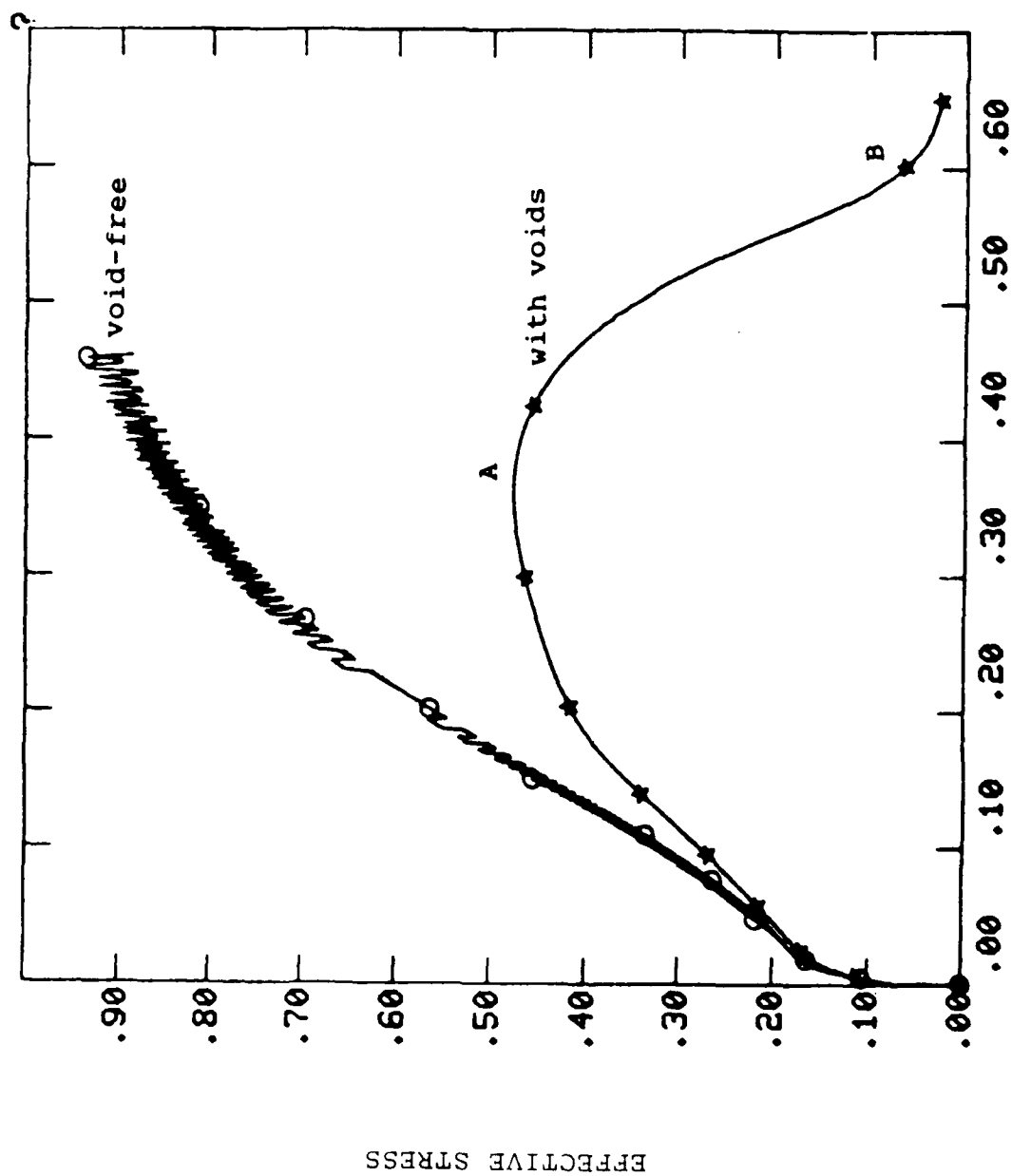


Figure 31. Comparisons of failure strain for tensile necking with and without voids. The solid line without symbols is an average measure of strain based on the pull velocity.



EFFECTIVE PLASTIC STRAIN

Figure 32. Comparison of σ_{eff} vs ϵ_{eff}^p for tensile necking with and without voids.

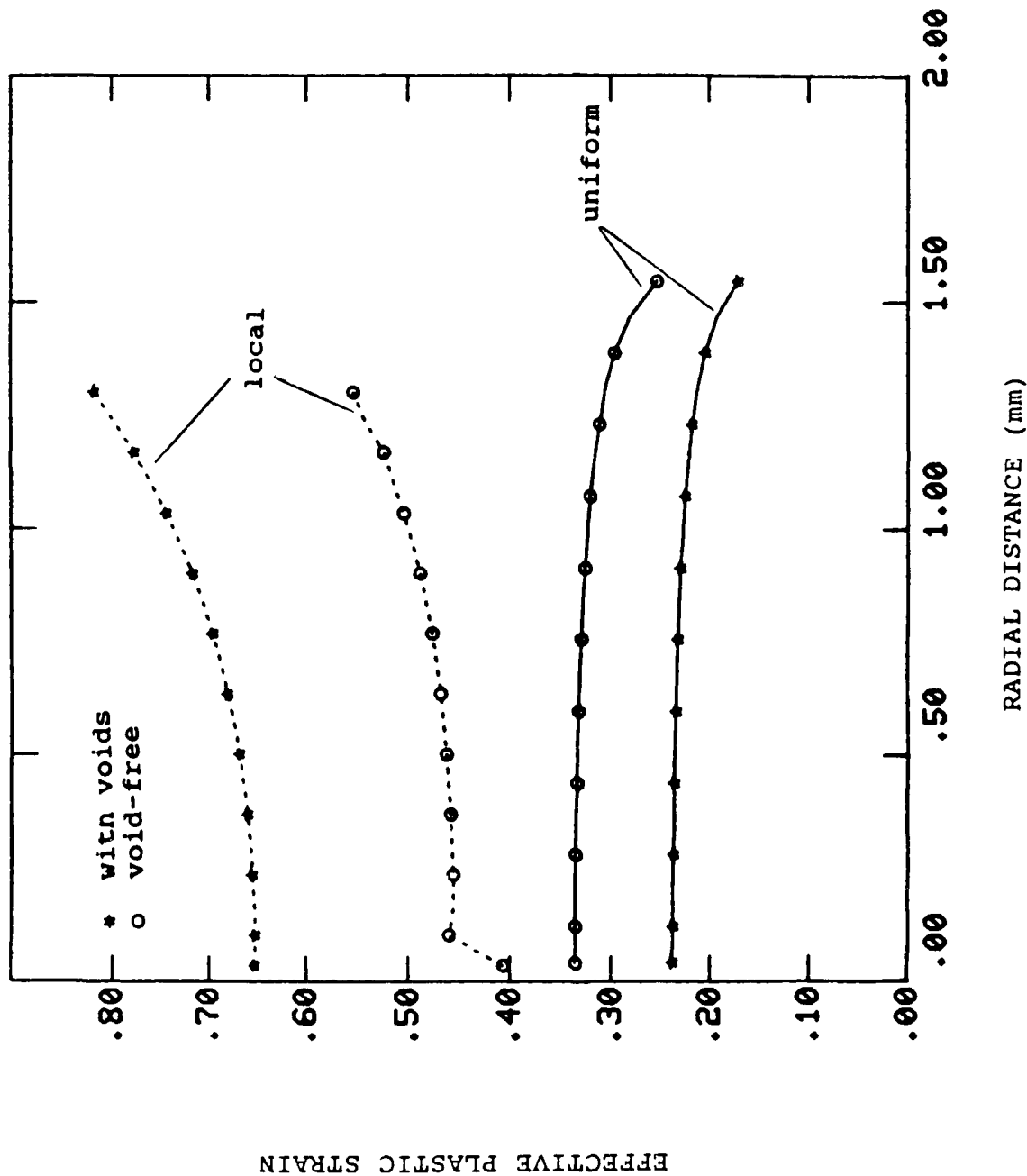


Figure 33. Radial distributions of ϵ_{eff} for cases with and without voids, plotted for elements in uniform (#182) and local (#382) sections.

plastic strain distribution is attributed to the inertial loading. Also, the stress-strain response was modeled as an isothermal process. In the simulations, the effects due to the adiabatic process are not considered.

The local plastic strain levels in the void-growth case are larger than that in the void-free case. The obvious reason is that void growth and pressure-dependent yield enhance the plastic flow. While loading continues in the local region, the uniform section unloads because of enhanced necking process due to void growth. Since the necking was not very severe in the void-free case, the loading continues in the uniform section as shown earlier in Figure 32. The effective strain along the uniform cross section continued to increase in this case.

The snapshots of stress triaxiality for the two cases were also plotted. The triaxiality was maximum at the local (minimum) section with void growth, especially near the axis ($r=0$) as can be seen from Figure 34. Other investigators [40-41] have observed similar behavior under quasi-static loading conditions with and without void growth. The triaxiality levels are relatively low near the surface, as one would expect. In the void-free case, the stress triaxiality is equal to 0.3 in the uniform section. However, for the uniform section of the void-growth case, the triaxiality near the axis is actually lower than 0.3. The reason for this can be explained from Figure 35.

Figure 35 shows the mean stress contour plots for the void-growth case. The material under compression is shown by the shaded region. The contour was plotted for the final solution time (60 microseconds). Failure initiation has occurred due to large void content near the central portion of the tensile specimen, failure initiation has occurred. This resulted in unloading of the uniform section and further loading under compression. In the void-free case (not shown in the figure), the uniform section unloaded completely but did not go into compression. If calculations were carried out beyond 60 microseconds, compressive loading might also occur in the void-free case. However, Norris et al. [40] in their numerical analysis of quasi-static tensile necking observed compressive zones away from the local region.

The deformed configurations of the shallow notched tensile specimen for the cases with and without void growth are shown in Figure 36. Only one half

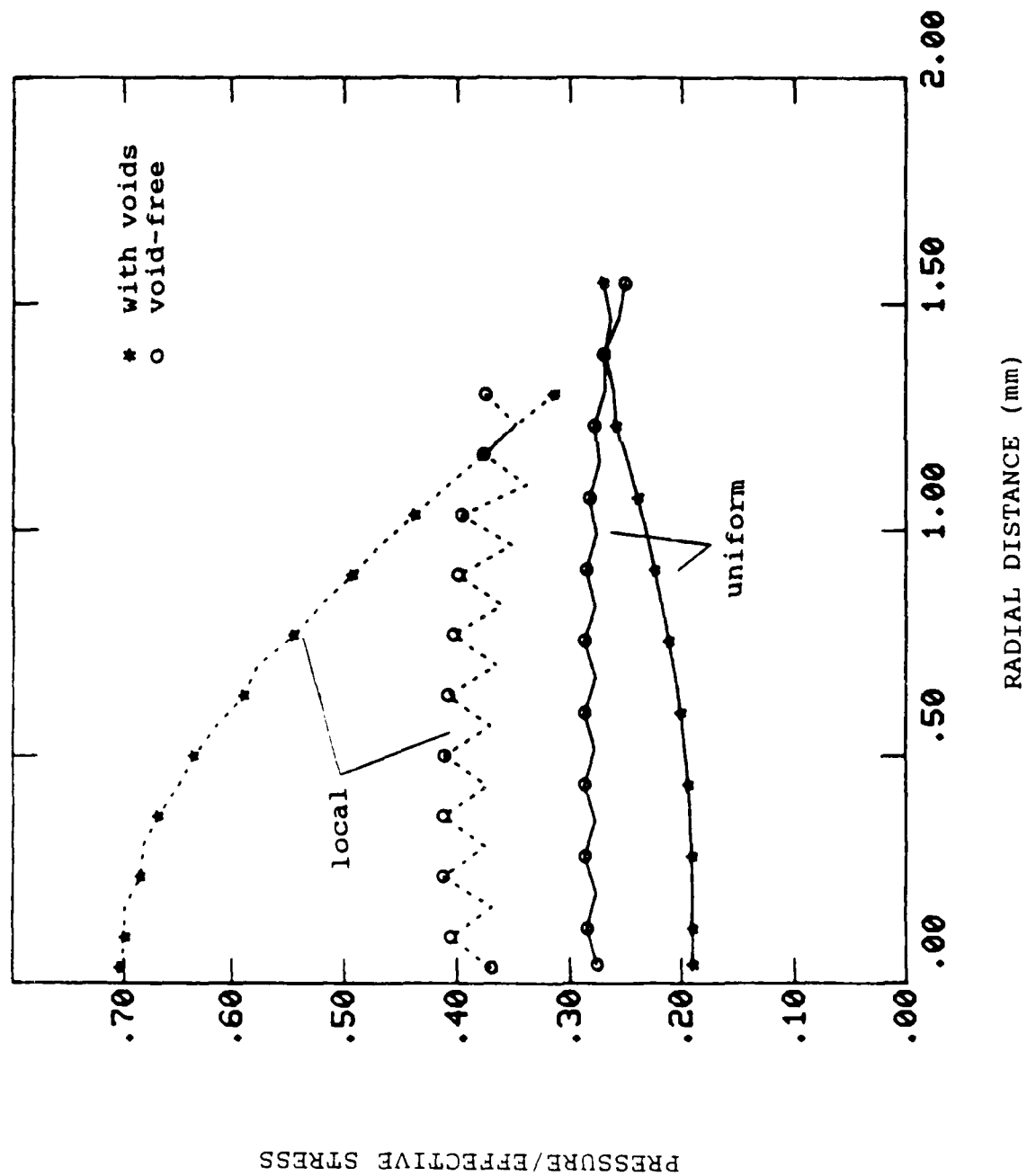


Figure 34. Measure of triaxiality ($P \sigma_{eff}$) along the radius for cases with and without voids.

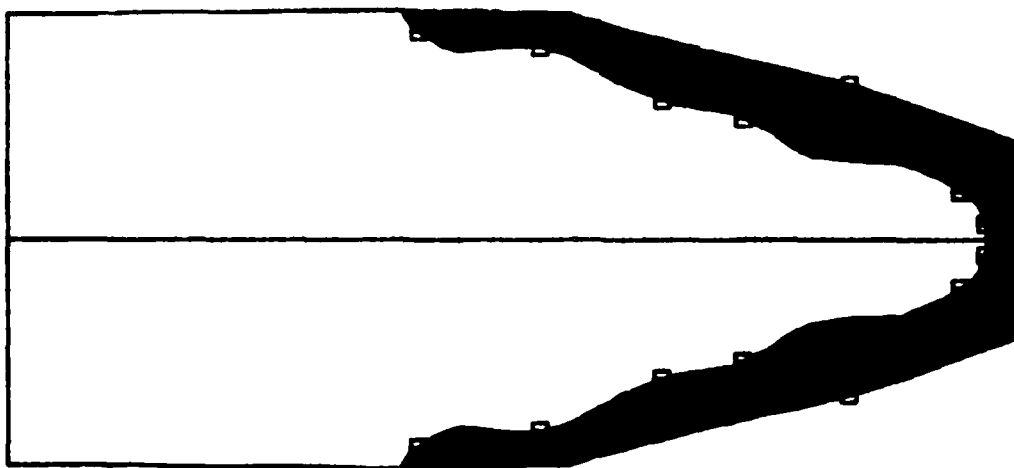


Figure 35. Pressure contour plot for void-growth influenced necking process. The shaded region is under tensile loading, and the rest of the region experiences compressive loading.

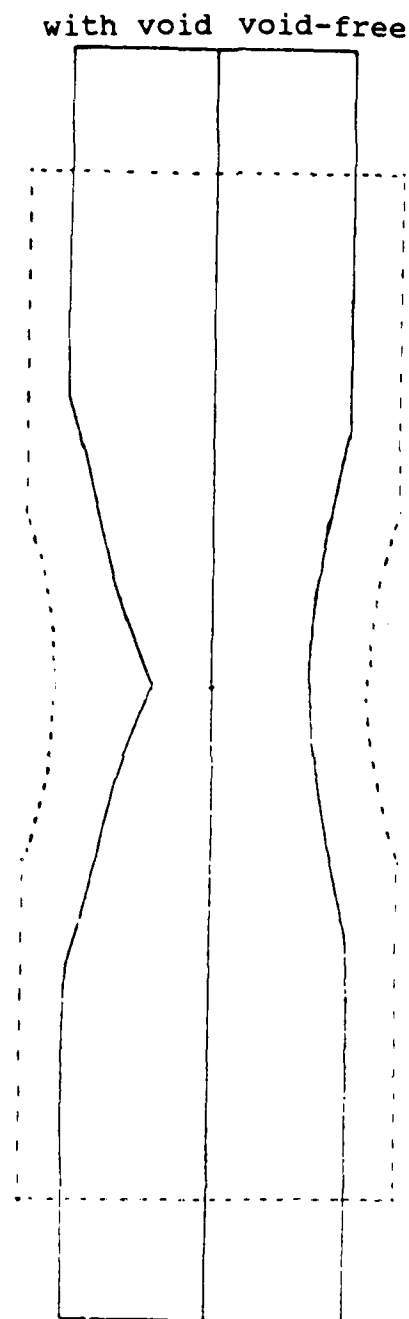


Figure 36. Initial (dotted) and final (full) shapes of the shallow notch tensile specimens.

of the specimen is shown for each case for comparison. Also included was the initial geometry, shown by the dotted line. In the void-free case, the neck profile retained the original notch shape while in the void-growth case the profile did not follow the notch shape as can be seen from Figure 36.

In the present application, the material was modeled as strain rate dependent and highly strain hardening. Additional exercises with different material behaviors such as perfectly plastic, strain rate independent, and thermal softening, with and without voids will shed additional light on the evolution of necking.

6.2 Application of RDG Model to Rod Penetration Problem

The main objective of this simulation is to show the spall evolution in the target using the RDG model. Until now, the model has been successfully used to describe the spallation phenomenon in plate impact configuration and void-growth enhanced tensile necking problems.

An EPIC-2 code simulation of a 2-inch long and 1-inch diameter solid copper rod impacting a 6-inch diameter and 1 inch thick HY100 steel at an impact velocity of 8333 ft/sec was considered. The corresponding finite element mesh is shown in Figure 37. The behavior of intact copper was modeled using the Johnson-Cook (JC) model [23] and the HY100 steel through the Bodner-Partom (BP) model [22]. The constants for both the BP and JC and the RDG models are given in Tables 1, 2, and 4 respectively.

The numerical solution was obtained for 20 microseconds. For analysis, elements near the axis of symmetry of the target and at a distance of 0.8125 inches from the impact point were examined. The time history of pressure, stress components, effective stress, and damage (void volume fraction) were stored for post-processing. Also plotted was the variation of these variables along the target radius at different depths for various time intervals. Damage contours at different time intervals were plotted to show spall zones in the target.

In Figure 38, the normalized pressure (mean stress / aggregate strength) is plotted with respect to time. The evolution of damage in terms of void volume fraction is also shown. The normalized pressure is a measure of triaxiality of the stress state. When the ratio is negative, it indicates that the material element is under compression, and void growth cannot occur.

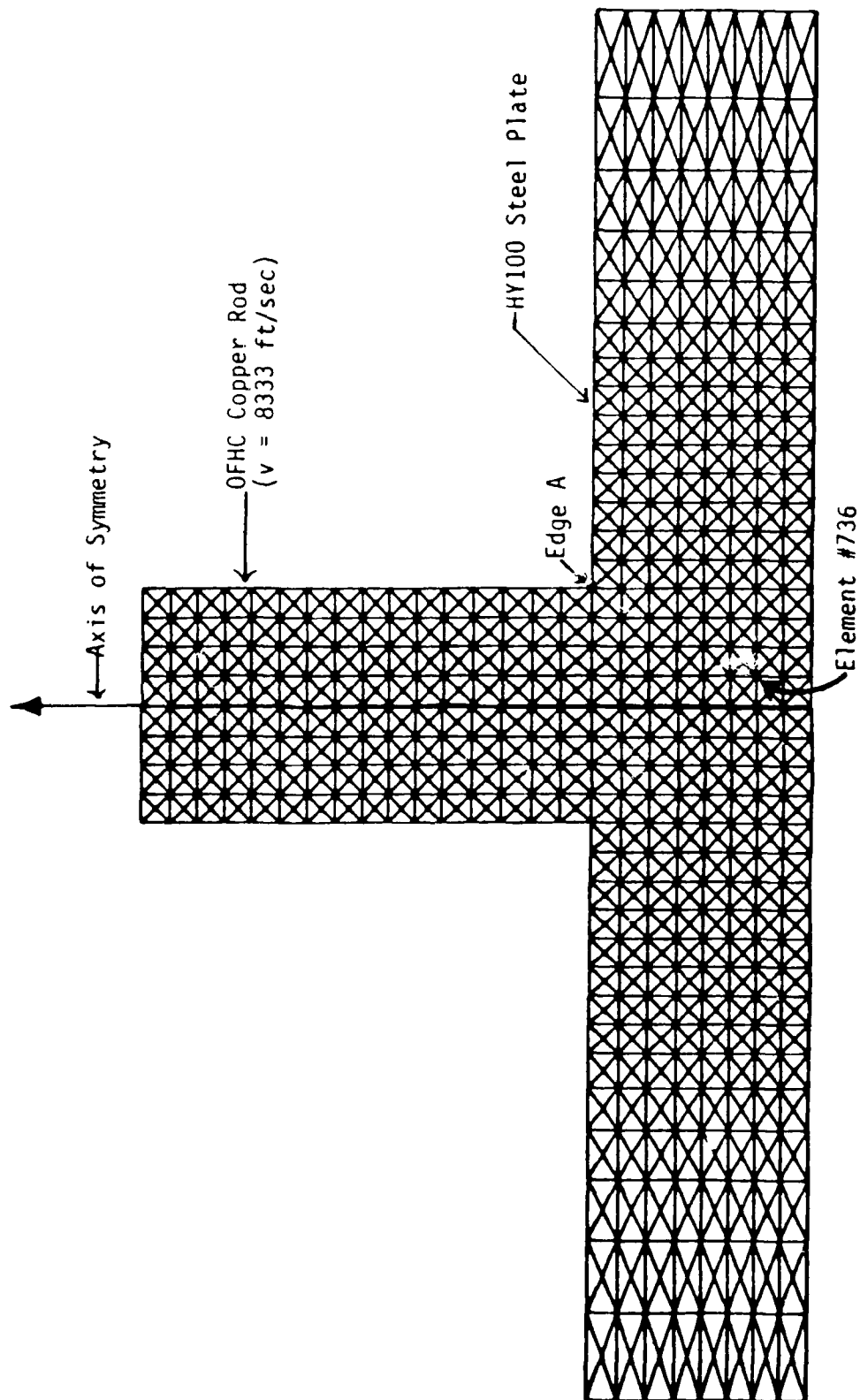


Figure 37. Finite Element Mesh for the Rod Penetration Problem.

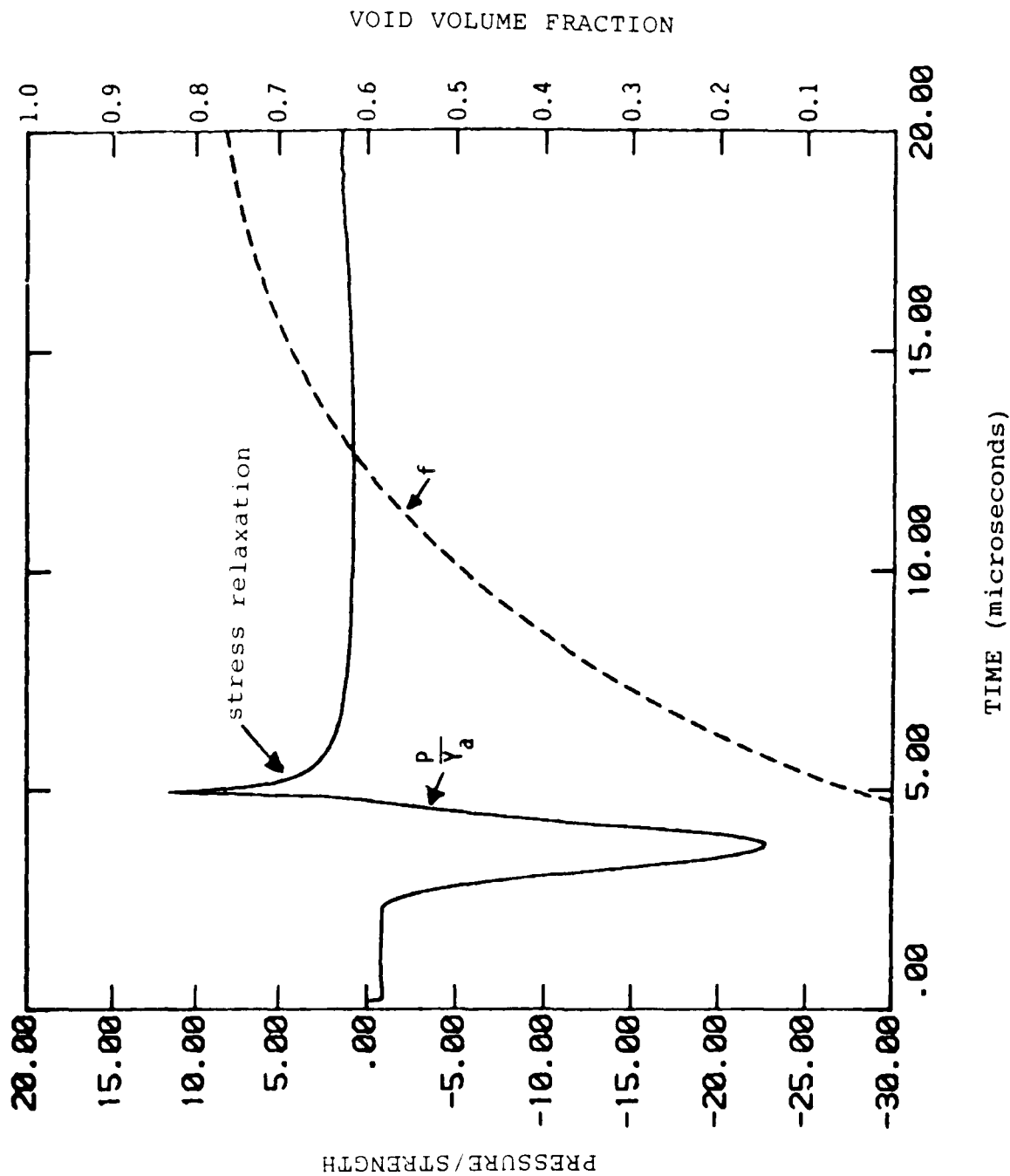


Figure 38. Measure of Traixiality, Ratio of Pressure (mean stress) and Strength (effective stress), and Void Volume Fraction with Respect to Time.

To generate voids in an intact ductile metal, high triaxial stress state under tension is required. The derivations of Rice and Tracey [7] and McClintock [6], and the quasi-static experiments of Hancock and MacKenzie [9] supported the concept that high triaxial tensile state enhances void nucleation and growth. The RDG model which is also based on this concept was able to model the void growth accordingly as can be seen from Figure 38. In a tensile test, before the occurrence of necking, the triaxiality ratio is $1/3$. However, in a penetration experiment configuration, the triaxiality could be large enough to generate spallation in the target. In this particular simulation, the tensile triaxiality reached extremely high (>10 in Figure 38).

In element #736, the release wave from the edge (point A in Figure 37) arrives at about 4 microseconds and releases the compressive pressure. Note that the distance of this element from the edge A in Figure 37 is around 0.9 inches. The wave speed in HY100 steel is 0.23 inches/microsecond.

The arrival time of the release wave from the stress free back surface of the target is about 5 microseconds. Note that the initial shock wave will reflect as a tensile wave. This tensile wave puts the element under a high triaxial stress state leading to void nucleation and growth. The void volume fraction increases while the tensile stress state prevails. As the material degrades due to voids, the pressure as well as the strength relaxes as shown in Figure 39.

The matrix material (intact HY100 steel) and porous aggregate (HY100 steel with porosity) strengths are also shown in this figure with respect to time. For further understanding and evaluation of the RDG model capabilities, the evolution of void volume fraction (damage) has also been included in the plot. Initially, the material (target element) is intact; therefore, the aggregate and matrix strengths are the same, and the curves between points A and B are identical. Void nucleation occurs around $t = 4.9$ microseconds. The void generation degrades the aggregate strength as shown by the sudden drop of the effective stress, Y_a to the point X and remained lower compared to the matrix strength (as shown by the dotted line). The matrix material strength (the strength of the undamaged HY100) obviously remained larger than the degraded material strength as one can see from Figure 39.

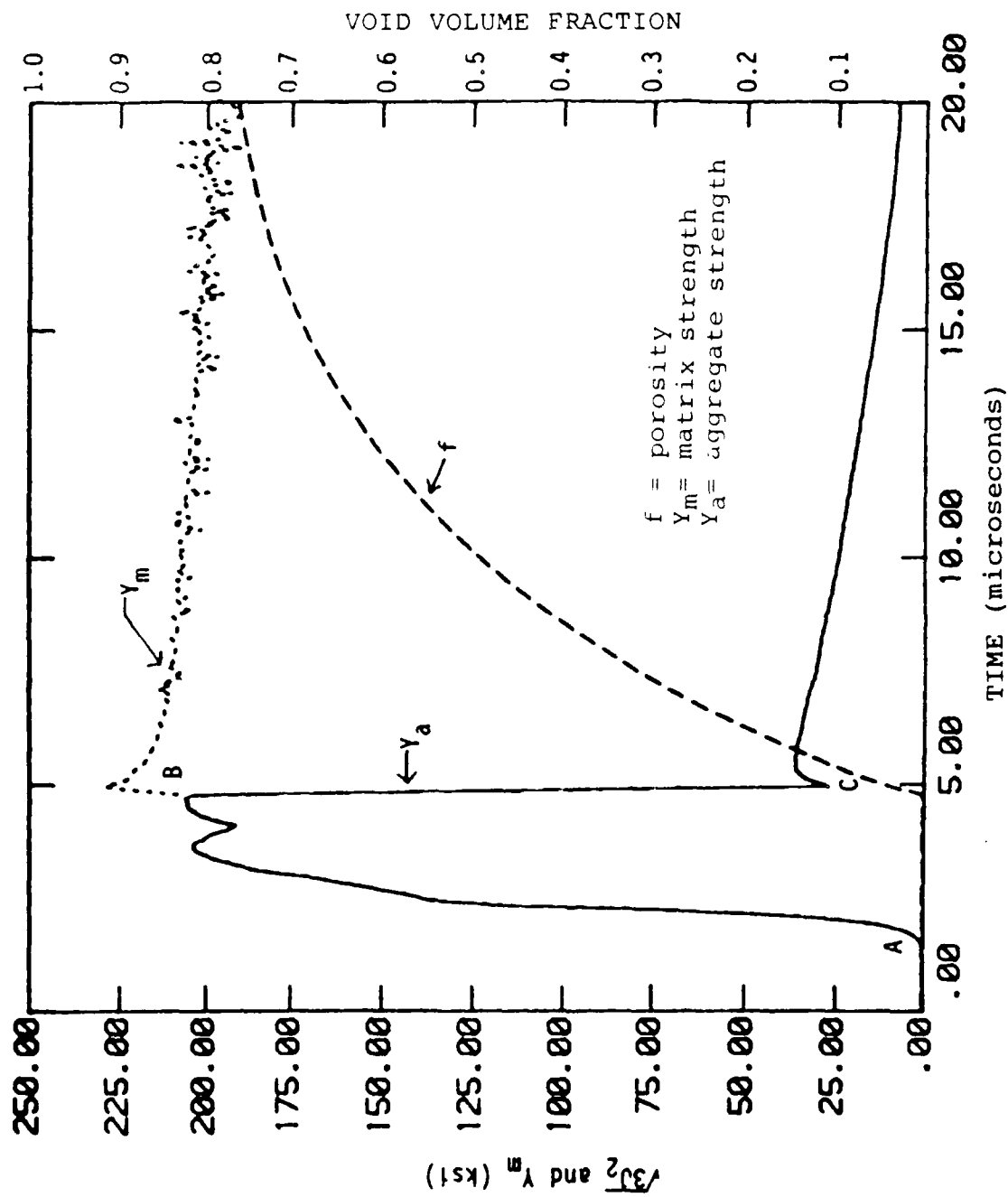


Figure 39. Effect of Void Volume Fraction, f (porosity) on the Aggregate Strength. The Matrix Strength (Y_m) is Independent of f .

In Figure 40, the loading path in element #736 was plotted with respect to the pressure dependent yield surfaces. Yield surfaces for various values of the void content are shown in this figure. These surfaces are generated from the relationship (Equation 16) between the normalized pressure and normalized effective strength. The pressure and the effective stress are normalized with respect to the matrix flow strength. Initially, the material is void free, and therefore the effective stress (strength) of the aggregate and the matrix are the same. For this reason, the loading path starts at the point A where the value of the normalized effective stress is one. When small amounts (<0.005) of voids nucleate between point A and B, the pressure dependence of the yielding makes the aggregate flow strength a function of pressure. The void-containing aggregate strength is lower than the matrix strength, and the ratio between these two strengths becomes less than one. As the loading progresses, rapid void growth occurs between the points B and D in Figure 40. The void content in element #736 increases to about 0.02 at C. The flow strength is about 60 percent of the original intact material (matrix) strength. Further void growth between points C and D degrades the flow strength to about 10 percent of its original value. Beyond point D, the material completely loses its load carrying capacity in tension, and the flow strength as well as the mean stress (pressure) relaxes to zero.

The RDG model does not include any void coalescence model; however, the void growth model has been formulated in a manner that rapid void growth occurs at a certain void volume fraction level indicating void coalescence. This can be clearly seen in Figure 40 between points D and F.

The extent of voids generated in the target due to high triaxial tensile stresses are shown in Figure 41. The void distribution along the radius at element #736 for two different time intervals (5 and 20 microseconds) are shown. A small amount of voids has nucleated and grown at the center of the specimen between A and B at $t=5$. Beyond a radial distance of 0.5 inches, the material is void-free. The strength relaxation can be seen between A' and B' due to this small amount of void generation. As the void distribution spreads to larger distances (between C and D) by 20 microseconds, the material strength diminishes, as represented by the solid line between C' and D' over a larger radius.

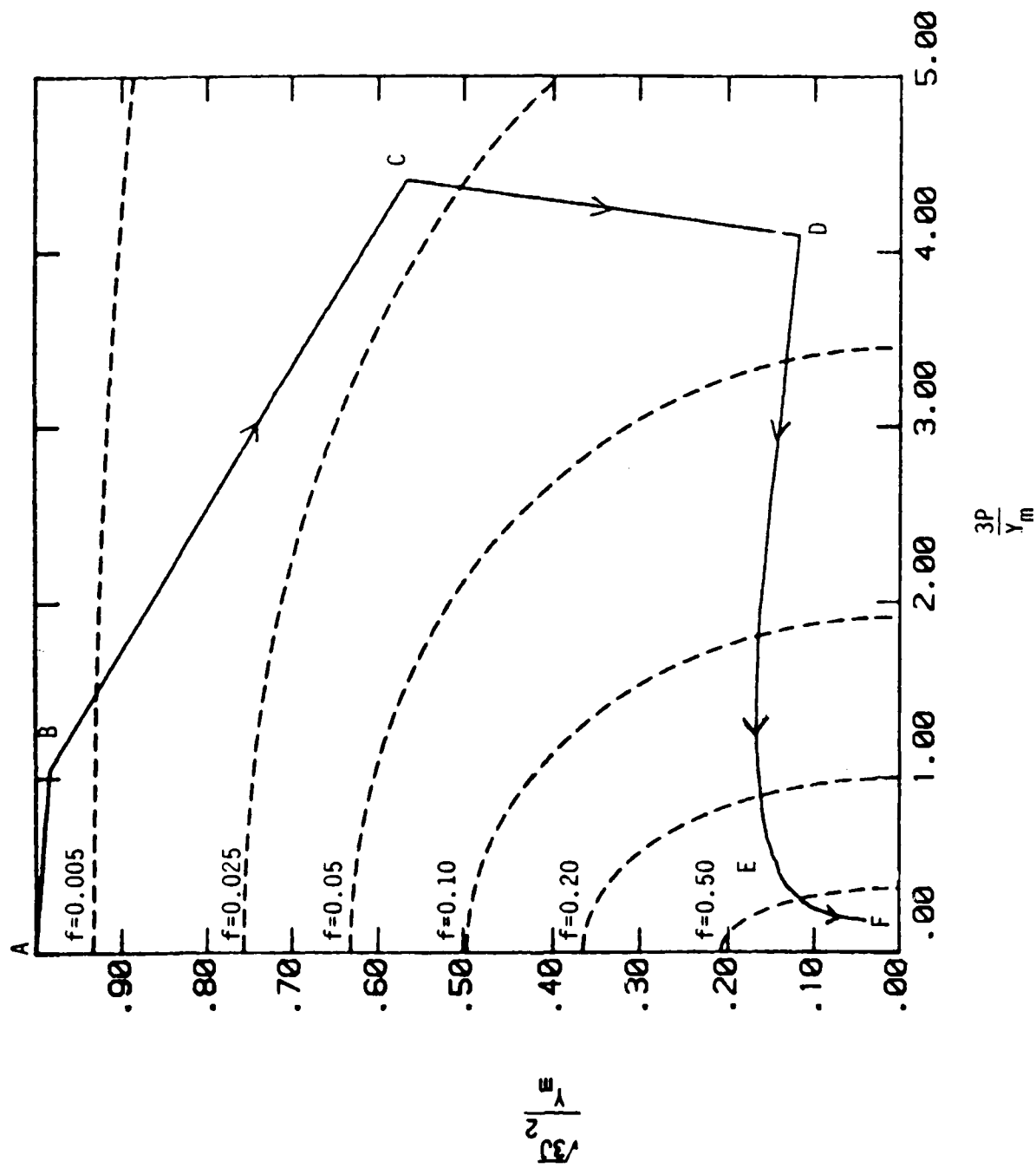


Figure 40. The Loading Path (solid line) with Respect to the Pressure Dependent Yield Surfaces.

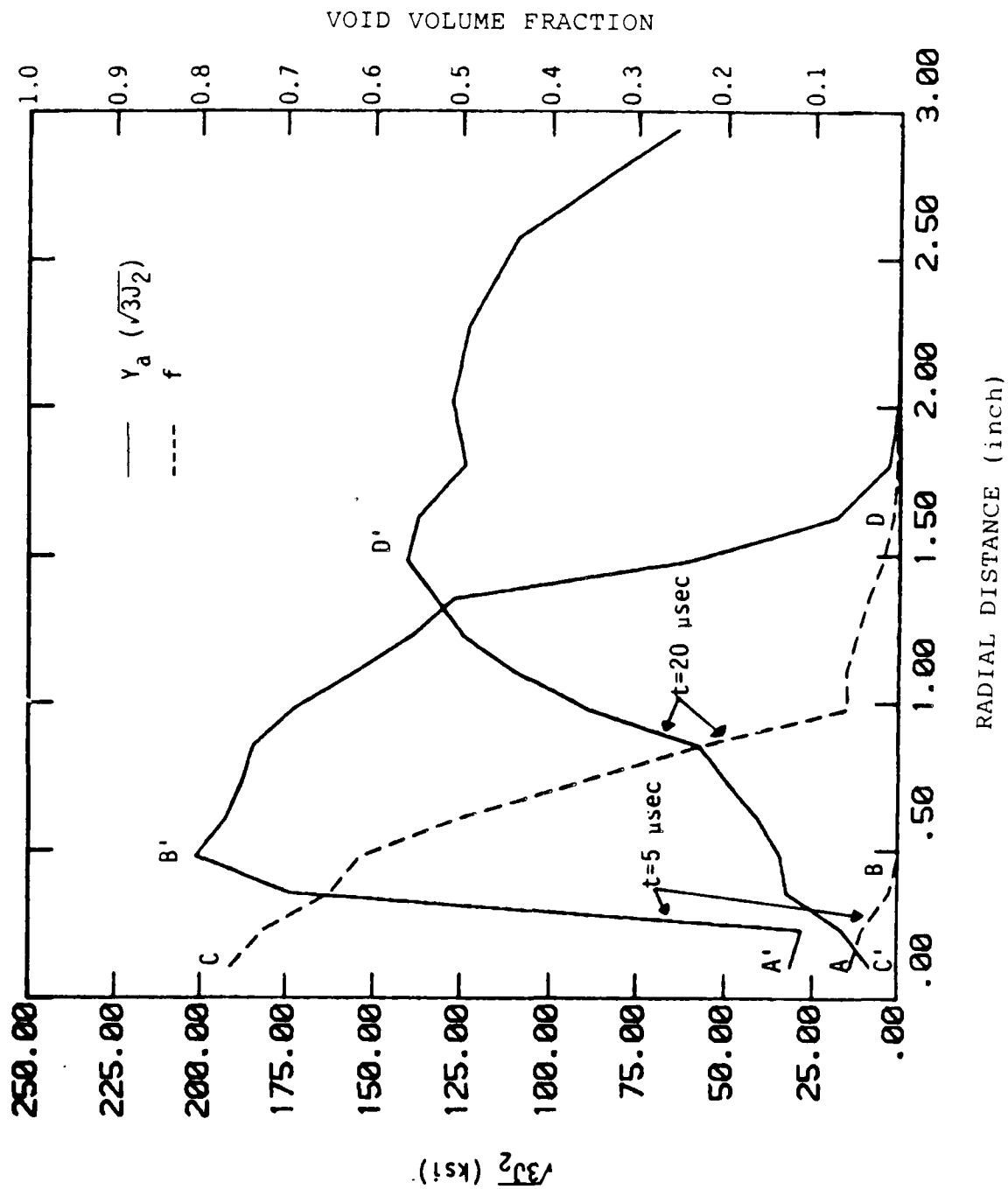


Figure 41. Distributions of Aggregate Strength (Y_a) and Void Volume Fraction (f) Along the Target Radius at Two Different Times.

The void volume fraction contours for different time intervals are plotted in Figure 42. At 5 microseconds, void nucleation and growth occurred at a distance 0.9 inches from the top of the target. Since the material around this region experiences relatively large tensile stresses, the spall initiates in this region first. The growth rate was relatively lower outside the region enclosed by the contour in Figure 42a. Between 5 and 10 microseconds, the void growth extended to a larger region as shown in Figure 42b. At 15 microseconds, the spall process is completed and intense void concentration occurred. The inner contours in Figure 42c represent this intense spall zone. The void volume fraction in this zone was well above 0.5. In a penetration experiment, the material often physically separates and forms stress free fracture surfaces in the target due to void coalescence; in some cases, spall fragments are ejected out from the back of the target.

For completion, the case of a penetration process without any material degradation was simulated. In the calculation, the void volume fraction was set to zero and also no other spall criterion was included. The material behavior was therefore described by the JC or BP viscoplastic models and without the RDG model. In Figure 43, the matrix and aggregate strength history plots from the two analyses, one with material degradation (RDG failure model) and the other without any degradation model, are presented. Again these plots are for the element #736 of the finite element mesh shown earlier in Figure 37. Since the aggregate and matrix strengths are the same in the absence of any porosity, the strength remained high as represented by the dashed line in Figure 43.

The deformed configurations of the penetrator and the target at time 20 microseconds are compared in Figure 44. The target exhibited a relatively larger bulge from enhanced plastic flow due to void softening of the material. Since the target material in front of the projectile has been damaged due to spalling, the penetration process is accelerated and this allows the projectile to penetrate easier. When there is no material degradation due to void nucleation and growth, the target material is relatively stronger, and therefore the penetration rate is slower compared to the case in which the material degrades. The differences in the deformed target shapes and the penetration rates demonstrate the importance of accurate dynamic failure model.

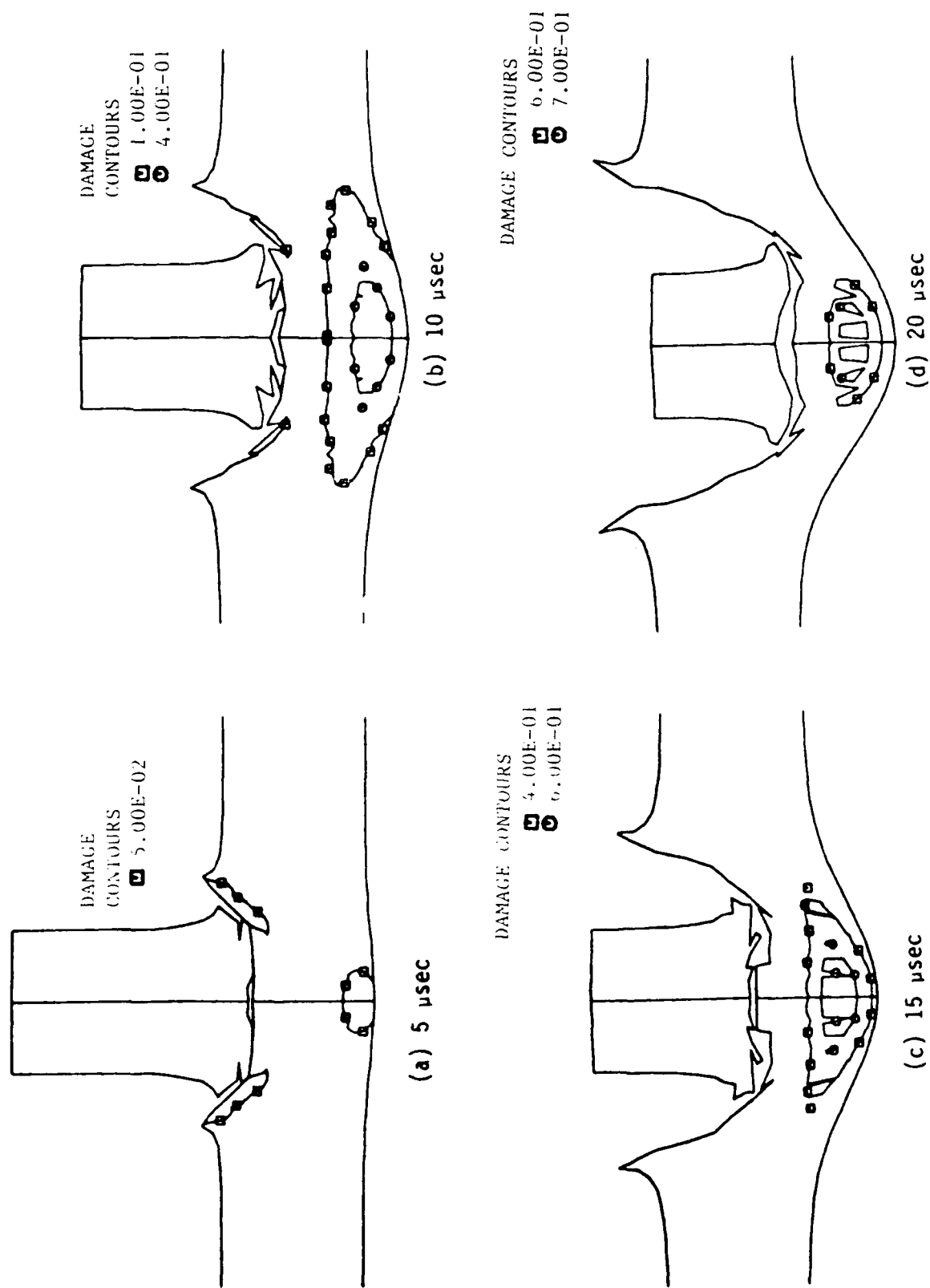


Figure 42. Damage contours at various stages in the rod penetration.

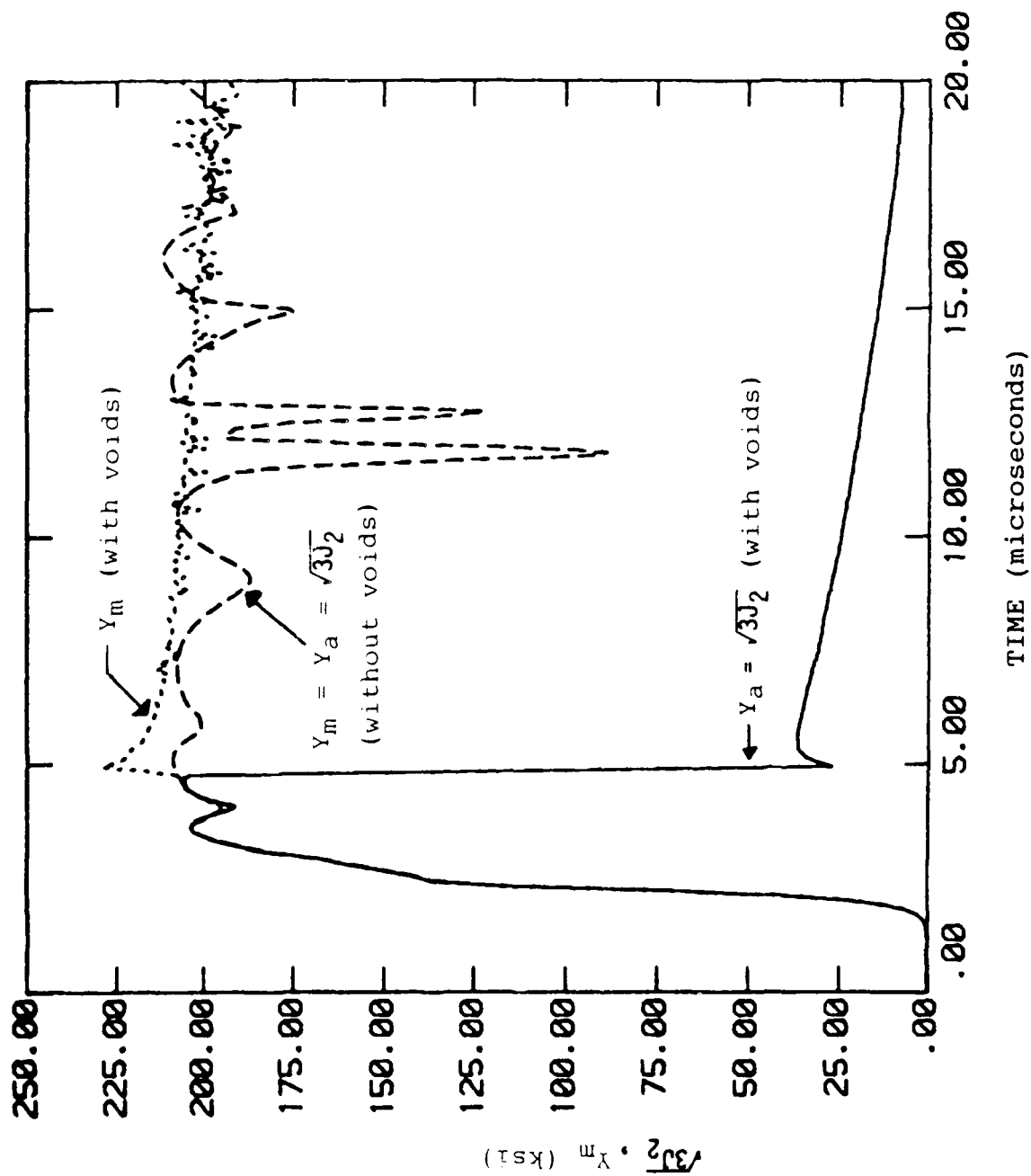


Figure 43. Comparisons of Yield Strength Aggregates (Y_a) With and Without Voids. Y_m is the Matrix Strength of Void Containing Material. Note that Y_m = Y_a when f = 0.

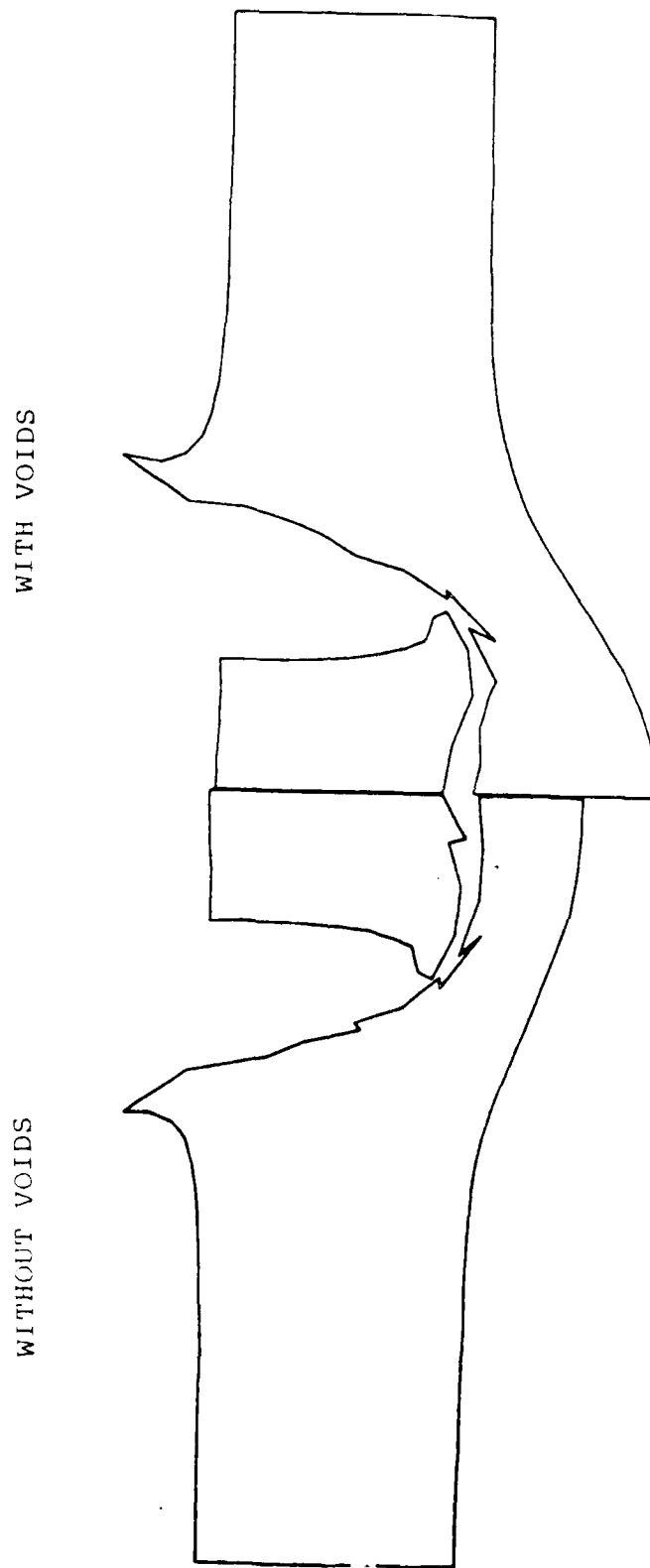


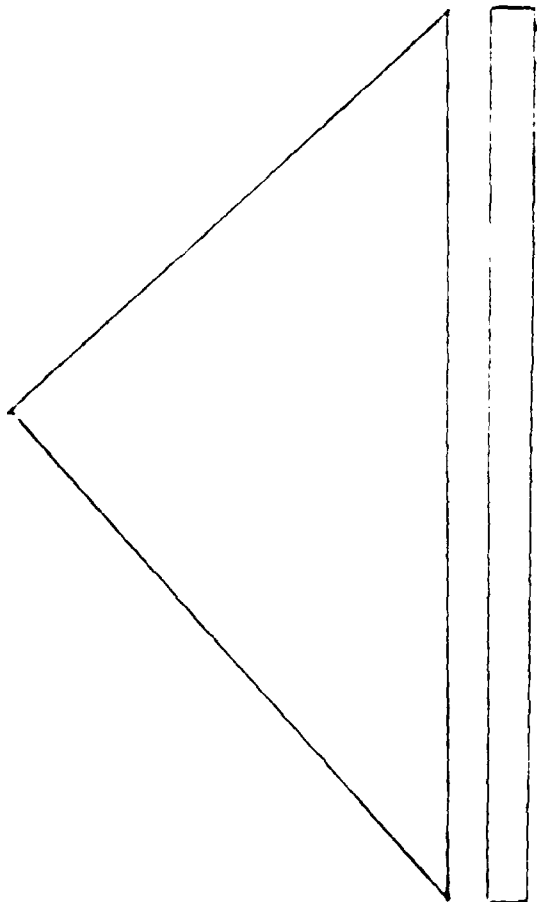
Figure 44. Deformed Configurations at 20 μ sec, With and Without Void Growth.

One could expect dependable and realistic failure predictions from physically based evolution equations of the failure model. Since the damage evolution depends on the time and loading history, use of appropriate damage evolution laws and viscoplastic description of the plastic flow are extremely important.

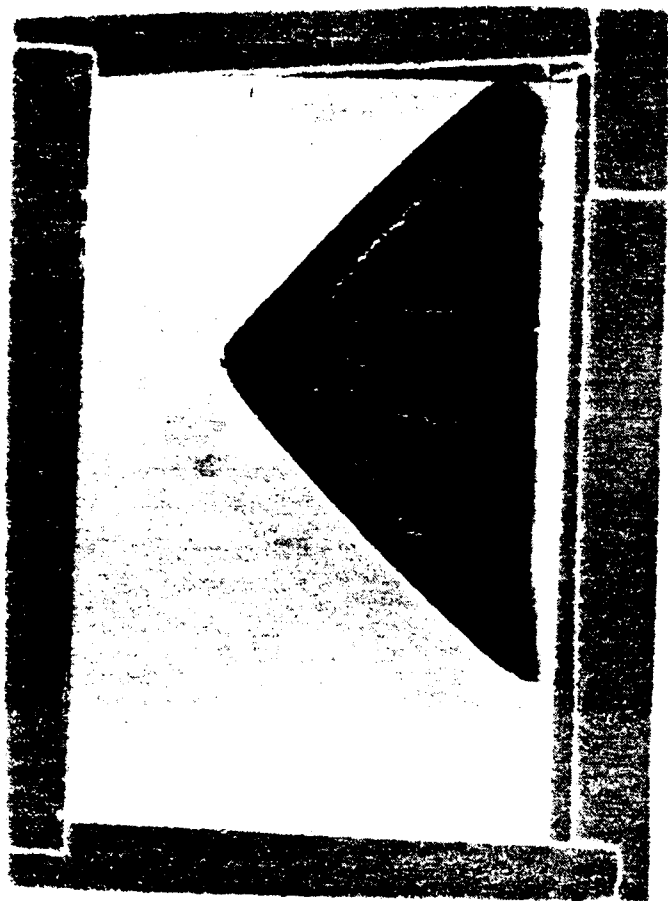
6.3 Spall in a Solid Cone Target

Bless [41] considered a plate impact configuration in which a flyer plate impacts the base of a solid right circular cone as schematically shown in Figure 45a. The target was a cone of 25 mm in height with a 90° included angle. The flyer and the target materials were 1020 steel. The flyer thickness and diameter were 2 mm and 38 mm respectively. Depending on the impact velocity, a complex spall pattern was generated in the cone. The pattern consisted of tunnel cracks parallel to the axis and longitudinal cracks parallel to the circumference of the cone, as shown in Figure 45b. This cone impact configuration is a two-dimensional axisymmetric geometry. However, the creation of spall regions leading to macrocrack formations destroy the axisymmetry, and the configuration eventually becomes three dimensional. The EPIC-2 code analysis includes only the onset of spallation and maps the various spall zones in the target. A flyer plate of diameter 50 mm was assumed in the simulation. The high strain rate behavior of 1020 steel was modeled using the Bodner-Partom model. The corresponding model constants are tabulated earlier in Table 1. The RDG model constants have been determined from plate impact experimental data and are given in Table 4. The solution was carried out for 60 microseconds. The finite element mesh for the cone configuration at $t=0$ and $t=60$ microseconds are shown in Figure 46.

EPIC analysis showed formation of incipient spall surfaces within five microseconds after the impact due to voids nucleation and growth. Figure 47 shows the void volume fraction contours for $t=5$ and $t=60$ microseconds. Comparisons between these two time intervals clearly indicated that the spall evolution is almost complete during the initial five microseconds. A qualitative comparison between the simulation and the experiment (Figure 45b) clearly shows that the RDG model could reproduce the salient features of the spall fracture evolution.

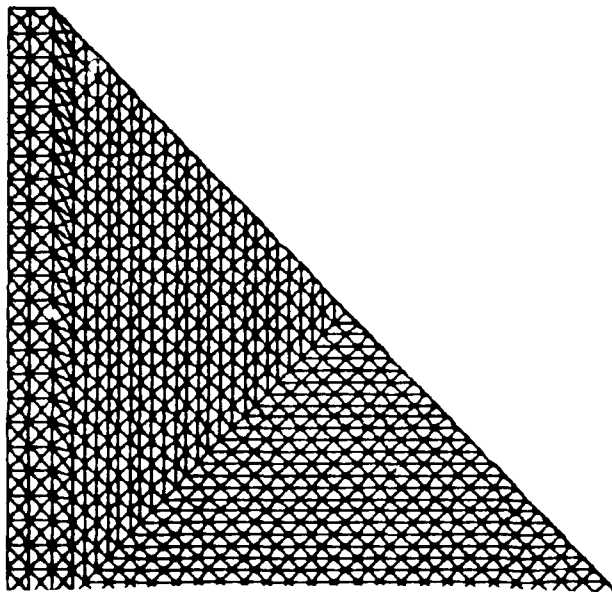


(a)

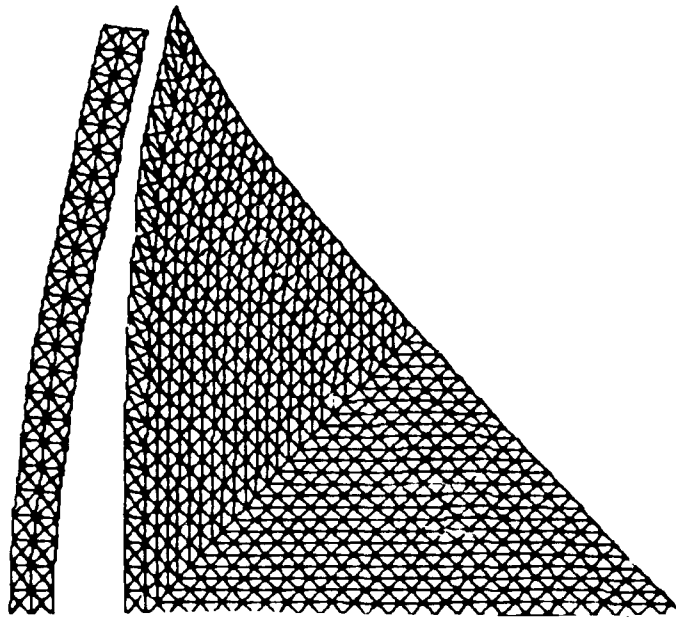


(b)

Figure 45. (a) Schematic Two Dimensional Sketch of a Flyer Plate Impact on the Base of a Right Solid Cone. (b) Recovered and Sectioned Solid Cone Revealing the Complex Spall Zones.

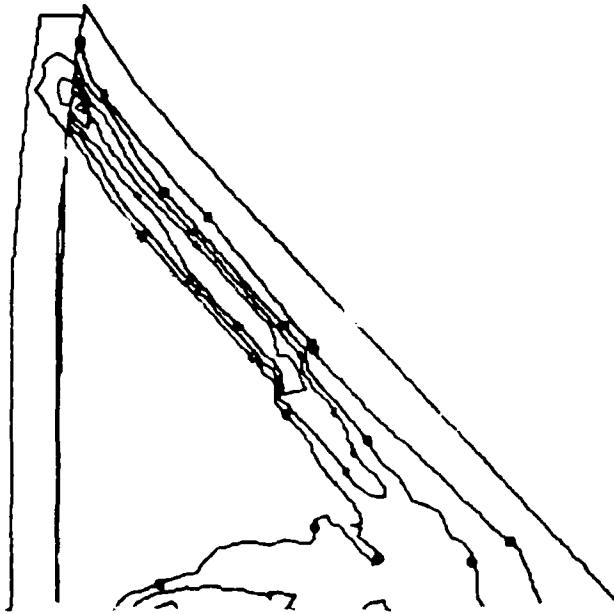


(a)

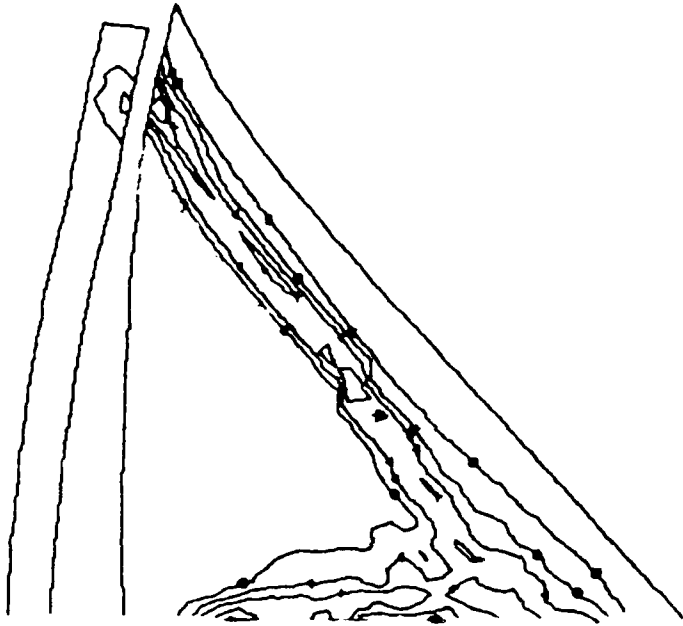


(b)

FIGURE 40. The Finite Element Mesh for the Cone Impact Geometry at (a) $t=0$ and (b) $t=0.60$ microseconds.



(a)



(b)

Figure 47. The Damage (Void Volume Fraction) Contour at (a) $t=5$ and (b) $t=60$ microseconds.

7. SUMMARY AND CONCLUSIONS

The RDG model is a continuum mechanics based ductile failure model. The model formulation is three dimensional and therefore applicable under a general stress-strain state. The RDG model describes several fundamental aspects of the failure process. When the failure process is initiated due to void nucleation in the material, the plastic flow becomes pressure dependent. Also, under high velocity impact loading, most metals exhibit strain rate dependent behavior. The RDG model includes the effects of pressure and strain rate in the constitutive (strength) model formulation. An important feature of the RDG model is its accurate modeling of the intact material using appropriate viscoplastic equations. The Bodner-Partom (BP) equations were selected for this purpose. The state variables in the RDG model formulation become the equivalent plastic strain rate in the matrix material and the BP model state variable Z , which describes the loading history effects.

A pressure dependent yield function serves as the plastic potential in the derivation of plastic strain rate for the void contained aggregate. Since the aggregate plastic strain rates are directly related to the equivalent plastic strain rate of the matrix material, the strain rate and loading history effects enter into the failure model formulation through the Bodner-Partom model. The RDG failure model does not require separate loading or unloading conditions. Both elastic and plastic rate components are taken to be always nonzero, and the same relations are intended to hold under loading and unloading conditions as in the Bodner-Partom model. When the equivalent plastic strain rates are numerically very small (<0.0001), the deformation is considered to be elastic.

Another appealing feature of the RDG failure model is the void growth law. Assuming that the void volume fraction rate is equal to the summation of the normal plastic strain rate components (dilation) removes the requirement for a new evolution law for the void growth rate. This modeling approach significantly reduces the number of model constants. While the Bodner-Partom model requires a number of constants, the determination of those constants is fairly straight forward and Rajendran et al., [24] reported a procedure to calibrate the constants using data from a limited number of standard impact tests.

In the RDG model, there are three constants for the nucleation, and two constants for the growth of voids. Model constants were determined from the numerical simulations of a plate impact experiment. The standard deviation is arbitrarily set to one third or one fourth of this stress. The initial value for the void volume fraction and the nucleation threshold stress can be adjusted to match the time arrival of the spall signal. The initial slope and amplitude of the spall signal will guide the selection of void growth constants.

The RDG model was implemented into the EPIC-2 finite element code. A numerically stable and accurate solution technique based on a diagonally implicit Runge-Kutta (DIRK) method was used to solve the complex and stiff governing differential equations. Various aspects of the numerical scheme were demonstrated in References 1 and 20. For solving only the Bodner-Partom equations, an iterative radial return scheme has been successfully implemented. The BP model constants had already been determined for these materials and reported by Rajendran and Bless [41]. The model accurately matched several of the plate impact experiments. The RDG model constants for OFHC copper, tantalum, Armco iron, and 1020, MAR 200, MAR 250, AF1410, C1008, and HY100 steels were determined and presented in the report.

The capability of the RDG model was extended to multiple impact loading conditions. The model could accurately predict the failure process in a twice-impacted target plate. Both void growth and collapse were modeled by the RDG model. To describe the pore collapse correctly, the critical value of the void volume fraction was calibrated for collapse. For complete spallation, the critical void volume fraction was arbitrarily assumed to be 1.0 for most metals.

The results from the analysis of application problems require additional in-depth analyses supported by experimental data. For example, to substantiate the tensile necking analysis, high speed photographic split Hopkinson bar tests on a shallow notch specimens should be conducted. The experimentally determined neck profiles should be compared with the RDG model predictions. For this purpose, selection of a material in which microvoids have been observed under dynamic tensile loading conditions is recommended.

It is desirable to perform instrumented penetration experiments for validating the RDG model prediction. Radiographs of the projectile and target during the penetration, and post-failure analysis on the target would identify additional model requirements. These radiographs are particularly important for verifying the spall fragmentation studies.

8. REFERENCES

1. Rajendran, A.M., Dietsberger, M.A., and Grove, D.J., "A Void Nucleation and Growth Based Failure Model for Spallation," J. Appl. Phys., 65, 1989, 1521-1527.
2. Argon, A.S., Im, J., and Safoglu, R., "Cavity Formation from Inclusion in Ductile Fracture," Metallurgical Transactions A., Vol. 6A, 1975, 825.
3. Gurland, J. and Plateau, J., "The Mechanism of Ductile Rupture of Metals Containing Inclusions," Transactions of the A.S.M., 56, 1963, 443.
4. Darlington, H., "Ductile Fracture Under Axisymmetric Stresses in Electrolytic Iron and Spheroidized Low-Carbon Steel, Ph.D. Diss., Dept. of Metallurgy and Materials Science, Lehigh University, Bethlehem, PA, 1971.
5. Beachem, C.D., "An Electron Fractographic Study of the Influence of Plastic Strain Conditions Upon Ductile Rupture Processes in Metals," Transactions of the A.S.M., 56, 1963, 318.
6. McClintock, F.A., "A Criterion for Ductile Fracture by the Growth of Holes," J. Appl. Mech., 35, 1968, 363.
7. Rice, J.R. and Tracey, D.M., "On the Ductile Enlargements of Voids in Triaxial Stress Fields," J. Mech. Phys. Solids, 17, 1969, 201.
8. Gurson, A.L., "Porous Rigid-Plastic Materials Containing Rigid Inclusions-Yield Function, Plastic Potential, and Void Nucleation," Adv. Res. Strength Fract. Matls., 2a, Tablin, D.M.R., ed., Pergamon Press, NY, 1977, 357.
9. Hancock, J.W. and MacKenzie, A.C., "On the Mechanisms of Ductile Rupture in High-Strength Steel Subjected to Multi-axial Stress States," J. Mech. Phys. Solids, 24, 1976, 147.
10. Tuler, F.R. and Butcher, B.M., "A Criterion for the Time Dependence of Dynamic Fracture," Int. J. Fract. Mech., 4, 1968, 431-437.
11. Rajendran, A.M. and Bless, S.J., "High Strain Rate Material Behavior," AFWAL-TR-85-4009, Wright-Patterson AFB, OH, April 1985.
12. Cochran, S. and Banner, D., "Spall Studies in Uranium," J. Appl. Phys. 48, July 1977.
13. Steinberg, D.J., Cochran, S.G., and Guinan, M.W., J. Appl. Phys., 51, 1982, 1498.
14. Curran, D.R., Shockey, D.A., and Seaman, L., "Dynamic Fracture Criteria for a Polycarbonate," J. Appl. Phys., 44, 1973, 4025-4038.
15. Curran, D.R., Seaman, L., and Shockey, D.A., "Linking Dynamic Fracture to Microstructural Processes," Shock Waves and High-Strain-Rate Phenomena in Metals, ed. M.A. Meyers and L.E. Murr, Plenum Press, NY, 1981, 129-167.

16. Curran, D.R., Seaman, L., and Shockey, D.A., "Dynamic Failure of Solids," Phys. Reports, 147, 1987, 253-388.
17. Davison, L., Stevens, A.L., and Kipp, M.E., "Theory of Spall Damage Accumulation in Ductile Metals," J. Mech. Phys. Solids, 25, 1977, 11-28.
18. Johnson, J.N. and Addessio, F.L., "Tensile Plasticity and Ductile Fracture," J. Appl. Phys., 64, 1989, 6699-6712.
19. Carrol, M.M. and Holt, A.C., "Static and Dynamic Pore-Collapse Relations for Ductile Porous Materials," J. Appl. Phys., 72, 1972, 1626-1636.
20. Rajendran, A.M., "A Void Growth Based Failure Model to Describe Spallation," Dynamic Constitutive/Failure Models, ed. A.M. Rajendran and T. Nicholas, AFWAL-TR-88-4229, Wright-Patterson AFB, OH, 1988.
21. Chu, C.C. and Needleman, A., "Void Nucleation Effects in Biaxially Stretched Sheets," J. Eng. Mat. Tech., 102, 1980, 249-256.
22. Bodner, S.R. and Partom, Y., "Constitutive Equations for Elastic-Viscoplastic Strain Hardening Materials," J. Appl. Mech., 42, 1975, 385-389.
23. Johnson, G.R. and Cook, W.H., "A Constitutive Model and Data for Metals Subjected to Large Strains, High Strain Rates, and High Temperatures," Seventh International Symposium on Ballistics, The Hague, Netherlands, April 1983.
24. Rajendran, A.M., Bless, S.J., and Dawicke, D.S., "Evaluation of Bodner-Partom Model Parameters at High Strain Rate," J. Eng. Mat. and Tech., 108, 1986, 75-80.
25. Johnson, G.R. and Cook, W.H., "Fracture Characteristics of Three Metals Subjected to Various Strains, Strain Rates, Temperatures, and Pressures," Eng. Fract. Mech., 21, 1985, 31-48.
26. Bodner, S.R., "Review of a Unified Elastic-Viscoplastic Theory," Unified Constitutive Equations for Creep and Plasticity, ed. A.K. Miller, Elsevier, 1987, 273-301.
27. Doraivelu, S.M., Gegel, H.L., Gunasekara, J.S., Malas, J.C., Morgan, J.T. and Thomas, J.F., "A New Yield Function for Compressible P/M Materials," Int. J. Mech. Sci., 26, 1984, 527-535.
28. Mackenzie, J.H., Proc. Phys. Soc., 63, 1950, 2.
29. Johnson, G.R. and Stryk, R.A., "User Instructions for the EPIC-2 Code," AFATL-TR-86-51, 1986, Eglin AFB, FL.
30. Johnson, G.R. and Holmquist, T.J., "Evaluation of Cylinder-Impact Test Data for Constitutive Model Constants," J. Appl. Phys., 64, 1989, 3901-3910.
31. Rajendran, A.M. and Bless, S.J., "Determination of Tensile Flow Stress Beyond Necking at Very High Strain Rates," Exp. Mech., 26, 1986, 319-323.

32. Rajendran, A.M., Grove, D.J., and Bless, S.J., Shock Waves in Condensed Matter, ed. S.C. Schmidt and N.C. Holmes, Elsevier, Amsterdam, 1987, 359.
33. Karnes, C.H., "The Plate Impact Configuration for Determining Mechanical Properties of Materials at High Strain Rates," Mechanical Behavior of Materials Under Dynamics Loads, U.S. Lindholm, ed. Springer-Verlag, NY, 1968.
34. Asay, J.R. and Lipkin, J., "A Self Consistent Technique for Estimating the Dynamic Yield Strength of a Shock Loaded Material," J. Appl. Phys., 49, 1978, p. 4242.
35. "STEALTH, Lagrange Explicit Finite-Difference Code for Solids, Structural, and Thermohydraulic Analysis," EPRI NP-2080, November 1981.
36. Yaziv, D., "Shock Fracture and Recompaction of Ceramics," Ph.D. Diss., Univ. of Dayton, Dayton, OH, 1985.
37. Yaziv, D., Bless, S.J., and Rosenberg, Z., "Study of Spall and Recompaction of Ceramics Using a Double-Impact Technique," J. Appl. Phys., 58, 1985, 3415-3418.
38. Grove, D.J., Rajendran, A.M., and Dietenberger, M.A., "Numerical Simulation of a Double Flyter Impact Experiment," 1989 Topical Conference on Shock Waves in Condensed Matter, Albuquerque, NM, 1989.
39. Hancock, J.W. and Brown, D.K., "On the Role of Strain and Stress State in Ductile Failure," J. Mech. Phys. Solids, 31, 1983, 1-24.
40. Norris, D.M., Moran, B., Scudder, J.K., and Quinones, D.F., "A Computer Simulation of the Tension Test," J. Mech. Phys. Solids, 26, 1978, 1-19.
41. Kleiber, "On Plastic Localization and Failure in Plane Strain and Round Void Containing Tensile Bars," Int. J. Plasticity, 2, 1986, 205-221.

APPENDIX A Numerical Solution of the Governing Equations in Section 3

The governing equations described in Section 3 are rearranged and numerically integrated. For stability, accuracy, and uniqueness of the solution, a second order diagonally implicit Runge-Kutta (DIRK) method was considered for integrating the system of stiff ordinary differential equations. The DIRK scheme is outlined in Appendix B. The DIRK variables are integrated using the estimated rates for the current time. Grove et al. [38] successfully implemented the RDG model in the EPIC-2 code using the DIRK scheme.

The EPIC-2 code calculates the current strain rates in each material element. Before any void nucleation occurs, the volumetric strain of the matrix and the aggregates are the same. However, once void nucleation occurs in an element, the incremental volumetric strain of the aggregate, ϵ_v , is the sum of the incremental elastic volume change, ϵ_v^e , in the aggregate (in the same sense as Mackenzie's) and the incremental volume change due to the viscoplastic growth of voids, ϵ_{ii}^p . This relationship can be related directly to the aggregate elastic compressible strain, μ_{ag} , from Equation (27) as follows. The relationship between the true volumetric strain and the compressible strain is by definition,

$$1 + \mu = (1 - f_0) \exp(-\epsilon_v) \quad (A.1)$$

where f_0 is the initial void volume fraction at the beginning of the simulation. The relationship between the true plastic dilatation and the void volume fraction is given by the direct integration of Equation (10) as,

$$1 - f = (1 - f_0) \exp(-\epsilon_{ii}^p) \quad (A.2)$$

where the plastic dilatation, ϵ_{ii}^p , is zero at $f = f_0$. Substituting equations (A.1) and (A.2) into Equation (27), we obtain the relationships,

$$\mu_{ag} = \exp(-\epsilon_v^e) - 1 \quad \text{and} \quad (A.3)$$

$$\epsilon_v^e = \epsilon_v - \epsilon_{ii}^p \quad (A.4)$$

ϵ_v^e is the true elastic dilatation strain of the aggregate. This development suggests that the plastic strain rates, $\dot{\epsilon}_{ij}^p$, as given by Equation (20) should be numerically integrated instead of integrating Equation (23). The aggregate pressure, P , is evaluated by using Equation (A.3) and the procedure outlined in Sections 3.4 and 3.5.

The true elastic deviatoric strains of the aggregate are given by the equation,

$$\epsilon_{ij}^e = \epsilon_{ij} - [\epsilon_{ij}^p - (\epsilon_{kk}^p/3)\delta_{ij}] \quad (A.5)$$

This leads to the degraded deviatoric stresses as in the equation,

$$s_{ij} = 2 \hat{G} \epsilon_{ij}^e \quad (A.6)$$

One numerical bonus of this approach is that the use of Equation (A.2) to calculate f avoids numerical integration of the stiff differential equation (10). Equations (2) and (7) lead to stiff differential equations; therefore, the DIRK scheme permits extremely small time steps to maintain solution stability and accuracy. For numerical efficiency (i.e. to avoid extremely small time steps), Equations (2) and (7) were analytically integrated to result in the following equations for the BP model loading history parameter and the void nucleation volume fraction,

$$Z = Z_1 - (Z_1 - Z_0) \exp(-\text{term}) \quad (A.7)$$

$$\text{term} = m_0 W_p + (m_1/\alpha) [1 - \exp(-\alpha W_p)] \quad (A.8)$$

$$f_n = (f_1/2) [\text{erf}((P + Y_m - \sigma_N)/(\sqrt{2} s_1)) - \text{erf}((- \sigma_N)/(\sqrt{2} s_1))] + \\ (f_2/2) [\text{erf}((D_m^p - e_N)/(\sqrt{2} s_2)) - \text{erf}((-e_N)/(\sqrt{2} s_2))] \quad (A.9)$$

One numerical bonus of having Equation (A.9) is not needing to evaluate the effective matrix stress rate, \dot{Y}_m , as was required in Equation (7). The value for the effective matrix stress is obtained from the yield function, Equation (16), as in the equation,

$$Y_m^2 = [(2+\rho^2) J_2 + \frac{1-\rho^2}{3} I_1^2] / \delta(\rho) \quad (A.10)$$

The yield function described by Equation (16) was treated as a plastic potential. Implicitly assumed was that the loading and unloading are controlled by the BP model through the matrix equivalent plastic strain.

This rearrangement of the governing equations has resulted in a fewer differential equations which are relatively less stiff. Thus, the numerical integration problem was reduced to the solution of the rate equations for D_m^P , W_p , I , and ϵ_{ij}^P .

Examination of Equation (1) shows that \dot{D}_m^P is ultimately the function of the same four integration variables (the variables input from EPIC are considered constant during the EPIC time step). That is, the Z in Equation (1) is only a function of W_p through Eqs. (A.7) and (A.8). The Y_m in Equation (1) is a function of f , P , and S_{ij} through Equation (A.10). The variables f , P , and S_{ij} are in turn functions of ϵ_{ij}^P through Eqs. (24) to (26) and Eqs. (A.2) to (A.6). Since the variables P and S_{ij} are also direct functions of f_n in the degraded modulus and that f_n is in turn a function of P and S_{ij} through Equation (A.9), an efficient convergent iterative scheme was developed to solve f_n simultaneously with P and S_{ij} . The temperature in Equation (4) and the pressure in Equation (26) are also direct functions of the specific internal energy. The rate equation for the internal energy is,

$$\dot{I} = (-P \dot{\epsilon}_v + S_{ij} \dot{\epsilon}_{ij}) / (1 + \mu) \quad (A.11)$$

Examination of these equations, Equation (18) for the plastic work rate and Equation (20) for the aggregate plastic strain rates, show that they are also ultimately functions of the same four dependent integration variables, D_m^P , W_p , I , and ϵ_{ij}^P .

The corresponding rate equations were solved using the DIRK scheme. Demonstrated in Section 3, was the solution stability, accuracy, and uniqueness with respect to different finite element mesh size and time step through one dimensional plate impact solutions. This was again demonstrated through two dimensional solutions of several application problems.

APPENDIX B
The Diagonally Implicit Runge Kutta (DIRK)
Scheme With Time Step Control

The diagonally implicit Runge-Kutta integration is given by the formula [B1],

$$K_i^{(n)} = f(t_n + c_i h, y_n + h \sum_j a_{ij} K_j^{(n)}), \quad i=1(1)q \quad (B.1)$$

$$y_{n+1} = y_n + h \sum_i b_i K_i^{(n)} \quad (B.2)$$

$$(dy/dt)_n = f(t_n, y_n) \quad (B.3)$$

h is the time step and y_n is the vector of the integrated variables at time, t_n . Note that K_i is also a function of itself, which requires an iterative corrector procedure. That is, the calculated value of K_i is re-substituted into the nonlinear equation (B.1) until convergence is achieved within an error tolerance. If convergence is not achieved after a certain number of re-substitutions of K_i , then the time step, h , is reduced. Convergence of K_i is assured if a small enough time step is chosen. In the RDG model implementation, if convergence was achieved within a very small error tolerance, the time step h was gradually increased to improve computation time. This scheme was implemented into the shock wave propagation, finite element code, EPIC-2

The EPIC-2 host code is based on the time-centered integration approach with the time step controlled by the Courant stability criterion; therefore, the time steps usually remain small. Thus, the lowest order DIRK, ($q=1$), will be adequate for stable and accurate solutions. For the values, $q=1$, $a_{11}=1/2$, $b_1=1$, and $c_1=1/2$, the DIRK method becomes second-order accurate. This special case is equivalent to Bass and Oden's [B2] recommendation of their Euler predictor-trapezoidal corrector scheme. Saliba [B3] has effectively proved this special case as stable and accurate in conjunction with the mechanical equilibrium equations for quasi-static problems.

With the DIRK method applied to the ODE of any viscoplastic formulation, a single corrector step was found sufficient for accurate calculations most of the time. However, during the stiff phase of the solutions, such as the unloading, the DIRK time steps require significant reduction even with several re-substitutions of K_i . Maximum efficiency during the stiff phases was achieved as follows. If after three re-substitutions of K_i the relative

error is not within two percent, the DIRK time step is reduced by one-tenth. The process continues until the two percent error is obtained. If, however, after three re-substitutions of K_1 the relative error is within two-tenth of a percent, the DIRK time step is increased in an arbitrary manner by 33% for the next time step. This process continues until the end of the EPIC time step is reached.

References for Appendix B

- B1. Al-Rabeh, A.H., "Embedded DIRK Methods for the Numerical Integration of Stiff Systems of ODEs," Int. J. Comp. Math., 21, 1987, 65-84.
- B2. Bass, J.M. and Oden, T.T., "Numerical Solution of the Evolution Equations of Damage and Rate-Dependent Plasticity," Int. J. Eng. Sci., 26, 1988, 713-740.
- B3. Saliba, J E., "Numerical Stability of Implicit Integration Schemes in Nonassociated Viscoplasticity," Comp. & Struct., 31, 1989, 693-698.